

**Founders:** The National Academy of Sciences of Ukraine

The E.O. Paton Electric Welding Institute of the NAS of Ukraine, International Association «Welding»

**Publisher:** International Association «Welding»

Editor-in-Chief B.E. Paton

*Editorial board:*

Yu.S.Borisov V.F.Grabin  
Yu.Ya.Gretskii A.Ya.Ishchenko  
V.F.Khorunov  
S.I.Kuchuk-Yatsenko  
Yu.N.Lankin V.K.Lebedev  
V.N.Lipodaev L.M.Lobanov  
V.I.Makhnenko A.A.Mazur  
L.P.Mojsov V.F.Moshkin  
O.K.Nazarenko V.V.Peshkov  
I.K.Pokhodnya I.A.Ryabtsev  
V.K.Sheleg Yu.A.Sterenbogen  
N.M.Voropai K.A.Yushchenko  
V.N.Zamkov A.T.Zelnichenko

*Promotion group:*

V.N.Lipodaev, V.I.Loktchev  
A.T.Zelnichenko (exec. director)

*Translators:*

S.A.Fomina, I.N.Kutianova,  
T.K.Vasilenko

*Editor*

N.A.Dmitrieva

*Electron galley:*

I.V.Petushkov, T.Yu.Snegireva

*Editorial and advertising offices:*

E.O. Paton Electric Welding Institute,  
International Association «Welding»,  
11, Bozhenko str., 03680, Kyiv, Ukraine

Tel.: (38044) 227 67 57

Fax: (38044) 268 04 86

E-mail: journal@paton.kiev.ua

http://www.nas.gov.ua/pwj

State Registration Certificate

KV 4790 of 09.01.2001

*Subscriptions:*

\$460, 12 issues per year,  
postage and packaging included.  
Back issues available

All rights reserved.

This publication and each of the articles  
contained herein are protected by copyright.  
Permission to reproduce material contained in  
this journal must be obtained in writing from  
the Publisher.

Copies of individual articles may be obtained  
from the Publisher.

## CONTENTS

### SCIENTIFIC AND TECHNICAL

- Podola N.V., Gavrish V.S. and Rudenko P.M.** Selection of input variables and structure of neural network to evaluate the quality of resistance spot welding ..... 2
- Ponomaryov V., da Costa A.V. and Scotti A.** Effect of an electrode metal droplet on arc voltage in gas-shielded welding ..... 5
- Cherepivskaya E.V. and Ryabov V.R.** Fusion welding of dispersion-strengthened aluminium-based composite materials, containing silicon carbide particles (Review) ..... 10
- Kalin N.A. and Efimenko N.G.** Peculiarities of carbon oxidation in welding with ilmenite-covered electrodes ..... 17
- Radkevich A.I.** Effect of deformation on electrochemical heterogeneity of pipeline welded joints ..... 21
- Kovalchuk V.S.** Allowance for effect of cycle asymmetry on fatigue resistance of welded joints ..... 24
- Pentegov I.V. and Petrienko O.I.** Method of calculation of voltage drop in electrode stickout length with allowance for non-linearity of thermophysical parameters ..... 27
- Lukina G.N., Bolshakov M.V. and Pidgajchuk S.Ya.** Properties of magnetron coatings on the Fe-Cr-Ni base with amorphous structure ..... 31

### INDUSTRIAL

- Bernadsky V.N., Maksimov S.Yu. and Netrebsky M.A.** Floating welded megastructures (Review) ..... 35
- Panchenko V.Ya. and Golubev V.S.** Development of laser technologies for materials treatment at the Institute for Problems of Laser and Information Technologies ..... 39
- Ryabtsev I.A., Kondratiev I.A., Vasiliev V.G. and Doroshenko L.K.** Wear resistance of deposited metal of Fe-C-Cr-Ti-Mo alloying system ..... 45

### BRIEF INFORMATION

- Tararychkin I.A. and Tkachenko A.N.** Repairing defects in thick metal using the technology of narrow-gap arc welding ..... 49
- Dragobetsky V.V.** Technology for explosion hardening of support surfaces of axle boxes ..... 51

### NEWS

- Welding in surgery — a new direction in welding technology ..... 54
- U.S. Congressman visits the E.O. Paton Electric Welding Institute of the National Academy of Sciences of Ukraine ..... 56



# SELECTION OF INPUT VARIABLES AND STRUCTURE OF NEURAL NETWORK TO EVALUATE THE QUALITY OF RESISTANCE SPOT WELDING

N.V. PODOLA, V.S. GAVRISH and P.M. RUDENKO

The E.O. Paton Electric Welding Institute, NASU, Kyiv, Ukraine

Analysis of input parameters of neural networks to control the quality of spot welding was conducted. The principal requirements to neural networks have been defined. It is shown that the proposed neural network ensures the required accuracy of predicting the weld spot nugget diameter and can be built into the microcontroller to control the spot welding process.

**Key words:** resistance spot welding, quality control, neural networks, microcontrollers

Despite the absence of reliable methods of quality control, resistance spot welding remains to be one of the main processes of joining sheet metals, for instance, in automotive industry. With the productivity of up to 200 spots per minute, it is rather difficult to evaluate the joint quality of each weld spot. Considering the stringent specifications to be followed in production, in particular, in aircraft industry, when variation of input parameters does not exceed 10 %, positive results were derived in controlling the quality of the spot, using regression models [1]. However, a considerable non-linearity of the process does not allow construction of an acceptable regression model, for instance, of the second order, for quality evaluation in a broader range of variation of the welding conditions.

Research has been going on lately that is devoted to development of mathematical models for arc and resistance welding, based on neural networks, that are constructed and then taught by the input and output variables of the process [2–4]. One of the most important problems is real-time evaluation of the joint quality.

Analysis of published work demonstrates the effectiveness of applying neural network models to evaluate the quality of the joints, made by resistance

welding. These models yield the error of forecasting the diameter of the weld spot nugget within 0.2–0.5 mm in welding two sheets 0.8 to 2.0 mm thick. On the other hand, the published articles, as a rule, do not describe the requirements to optimisation of the network structure and number of variables, and do not demonstrate the ability to incorporate the programs into the existing computer controllers to control the resistance welding machines (for instance, RVK-100). For optimisation of the structure of the neural network and number of input parameters, as well as adaptation algorithms, a controller with a small memory and low response can be used.

Thus, it is necessary to not only confirm the possibility of creating the control system, but also ensure that the above conditions are satisfied, in order to apply the neural network model in the controller.

Described below are a neural network, developed at the E.O. Paton Electric Welding Institute, with optimised structure and input variables, as well as the results of its testing in spot welding of Zn-plated steel, using RVK-100N type controller.

Welding mode parameters are mostly used as the input parameters of the neural networks, namely welding current  $I_w$ , inter-electrode voltage  $U_e$ , welding time  $t_w$ , electrode clamping force  $F_{cl}$ , as well as their derivatives (inter-electrode resistance  $R_e$ , power  $P_w$ , energy  $Q_w$ , etc.).

In addition, the neural networks are characterised by the number of buried layers, of neurons in these layers, as well as output neurons (Figure 1). The following characteristics of welding quality are used as the output parameters: diameter of weld spot nugget  $d_n$  or rupture strength  $F_r$  at mechanical testing of specimens. Other quality characteristics are also used (penetration depth of weld spot,  $h_p$ , availability of splashes, cracks or other defects).

Teaching a neural network is an iteration process, that is conducted, using an experimental sample of input and output parameters, and during which the synaptic weights  $W_{ij}$  and thresholds  $Q_k$  are determined at minimal error of forecasting the nugget diameter  $\Delta_{\min} = d_{\text{meas.n}} - d_{f.n}$  (Figure 2) or rupture force  $\min \Delta_F = F_{\text{meas.r}} - F_{f.r}$ . Further on the taught neural

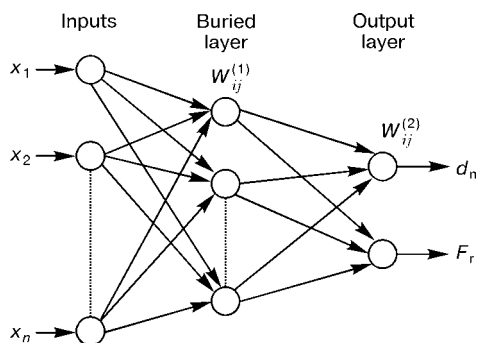


**Figure 1.** Generalised structure of a neural network for controlling the resistance welding quality ( $x_1$ ,  $x_2$  and  $x_n$  are the input parameters)

© N.V. PODOLA, V.S. GAVRISH and P.M. RUDENKO, 2002

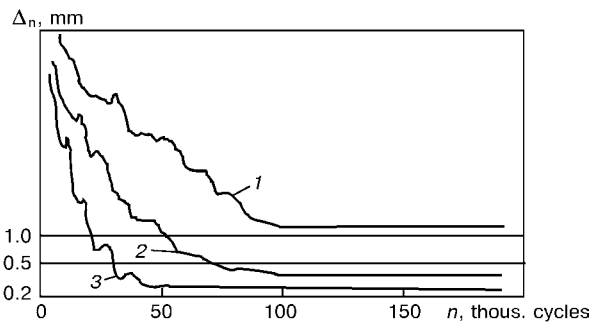


**Figure 2.** Dependence of the error of  $d_n$  forecasting on the number of teaching cycles: 1 – unsatisfactory; 2 – satisfactory; 3 – good neural network

network can be used to evaluate the quality of welding by the input parameters [2].

In neural network analysis to evaluate their effectiveness the following factors were assumed: error of  $d_n$  forecasting, number of input signals, hidden layers and output neurons, simplicity and reliability of the sensors, as well as the ability of applying the neural networks in single crystal controllers.

Let us consider some features of neural networks, given in works [5–9].

In article [5] the described neural network consists of 17 input neurons, 12 neurons of the buried layer and 2 output neurons. Signals, proportional to dynamic inter-electrode resistance in each period of the mains voltage during the entire time of welding, are applied to the neural network inputs:

$$R_i = \frac{U_{e_i}}{I_{w_i}} \quad (i = 1, 2, \dots, 17).$$

As output parameters one neural network uses the diameter of the spot nugget  $d_n$  and penetration depth  $h_p$  (Figure 3), and another – rupture strength  $F_r$ .

The error of  $d_n$  forecasting is not more than 10 %, although in some cases it rises up to 25 %. A large number of input parameters, dependent on the welding pulse duration, as well as the low forecast precision can be regarded as the shortcomings of this system.

Work [6] describes a neural network where  $I_w$ , averaged over the entire welding time  $t_w$ , is introduced in addition to input parameters  $R_{e_i}$  for each half-period. The optimal number of neurons in the intermediate layer is six. The absolute error of  $d_n$  forecasting is not more than 0.5–0.6 mm. Other disadvantages of this system also include a large number of input parameters and their dependence on  $t_w$ .

In study [7] effective values of  $I_w$ ,  $U_{e_i}$  measured in each half-period during  $t_w$ , are used as the input parameters. In addition, applied to the neural network inputs are their values, proportional to the duration of welding current half-waves in the first three half-periods. The number of neurons in the buried layer is five. Welding quality is classified by the good–bad principle. System disadvantages are similar to those of the previous systems.

Different combinations of the values of inter-electrode resistance are used for the inputs of the neural

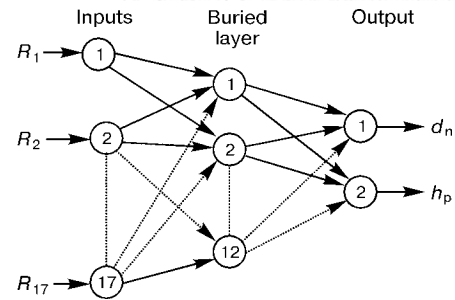


**Figure 3.** Neural network with input parameters  $R_i = U_{e_i}/I_{w_i}$

network described in [8]. In addition to  $R_{e_i}$ ,  $R_{\max}$  and  $R_{\min}$ , difference of resistances, calculated at different moments  $t_w$ , as well as power, evolved in welding, are applied to the neural network input for each half-period. At  $t_w = 12$  periods 30 parameters are applied to the neural network input (Figure 4). The forecast error is not higher than  $\pm 0.5$  mm for 80 % of the classified specimens. An extremely large number of input variables (30), making the neural network model more complicated, should be regarded as one of the system disadvantages.

The dynamic characteristics of the welding process are taken into account to a greater degree in the neural network, described in study [9]. Applied to the neural network inputs, in addition to  $I_w$  averaged over  $t_w$ , are various combinations of inter-electrode resistances, their maximal and minimal values and increments over different time intervals. Neural network has 10 inputs, with 4 neurons in the buried layer. Error of  $d_n$  forecasting is  $\pm 0.5$  mm. The system has such shortcomings as the cumbersome nature of preliminary calculations to generate the input parameters.

It should be also noted that these publications do not give any data on the ability of applying the proposed neural networks in 8-bit controllers with limited computational resources. Their common drawback is a large number of input variables and complex structure.

For a reliable forecast of  $d_n$  using a neural network, it is necessary to select its optimal structure, as well as the optimal combination of input variables, taking into account the changes in the welding process.

Detailed analysis of input parameters of a neural network allows forecasting their influence on the error of  $d_n$  forecasting. Studying  $I_w(t)$ ,  $U_e(t)$  and  $R_e(t)$  shows that the welding quality is essentially deter-

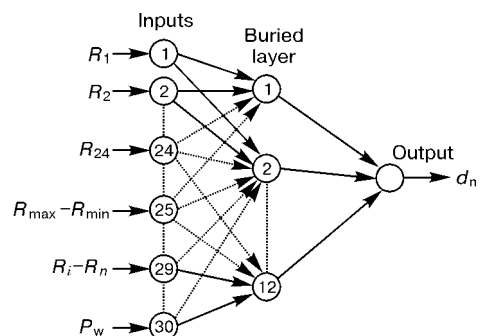


**Figure 4.** Neural network with input parameters  $R_i = U_{e_i}/I_{w_i}$ ;  $(R_{\max} - R_{\min})$ ,  $(R_i - R_n)$  and  $P_w = U_e I_w$

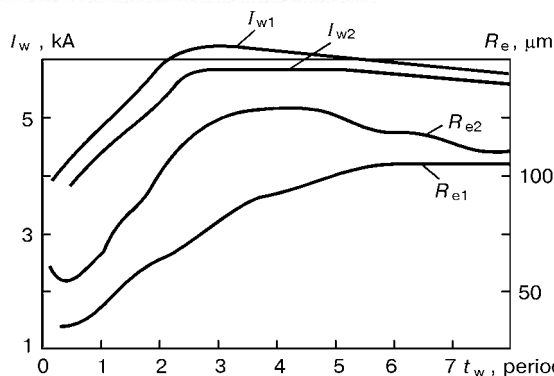


Figure 5.  $I_w(t)$ ,  $R_e(t)$  dependencies ( $I_{w1}$ ,  $R_{e1}$  — lack-of-penetration,  $I_{w2}$ ,  $R_{e2}$  — normal welding)

mined not only by the final value of these parameters or their averaged values that was usually used in the known systems of monitoring and adjustment, but also by their values at different moments  $t_w$ .

From Figure 5 it can be seen that the final values of  $I_w$  and  $R_e$  are approximately the same. However, in the first case the welding quality is satisfactory ( $d_n = 5.2$  mm), and in the second a complete lack of penetration is found (weld spot nugget is practically absent), caused by wear of the electrode working surface, i.e. its increase by 30–50 %. For this reason, values of  $I_w$  and  $U_e$  or  $R_e$ , measured at different moments  $t_w$ , were used as the input parameters of the neural network.

Welding experiments were conducted on specimens of low-carbon steel of thickness  $\delta = 0.8 + 0.8$ ,  $1.2 + 1.2$  and  $2.0 + 2.0$  mm with Zn-plated coating and without it in ARO type tongs.

Welding mode was as follows:

for  $\delta = 0.8 + 0.8$  mm:  $I_w = 7.2$  kA,  $t_w = 8$  periods,  $F_{cl} = 280$  daN,  $R_e \leq 50$  mm,  $d_n = 4.5$  mm;

for  $\delta = 1.2 + 1.2$  mm:  $I_w = 9$  kA,  $t_w = 10$  periods,  $F_{cl} = 350$  daN,  $R_e \leq 75$  mm,  $d_n = 5.5$  mm;

for  $\delta = 2.0 + 2.0$  mm:  $I_w = 12$  kA,  $t_w = 12$  periods,  $F_{cl} = 600$  daN,  $R_e \leq 100$  mm,  $d_n = 7$  mm.

Selection of welding mode parameters and the procedure of quality evaluation by the spot nugget diameter  $d_n$  was conducted, taking into account IIW recommendations. The weld spot nugget diameter was determined as the average measured value

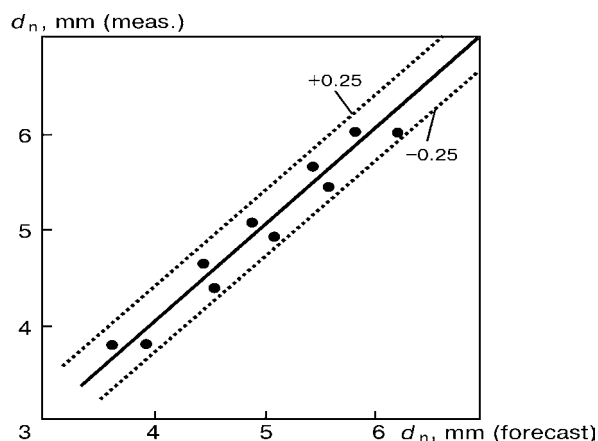


Figure 6. Evaluation of the error of  $d_n$  forecasting

$$d_n = \frac{d_{n_{\max}} - d_{n_{\min}}}{2}$$

During the experiments the welding mode parameters were varied as follows:  $U_m$  by  $+5 - 15$  %,  $I_w$  by  $+25 - 30$  %,  $d_e$  by  $+40$  %. The diameter of the weld spot nugget was reduced by 30–40 %, i.e. the welding mode was varied from lack of penetration up to a splash. Welding process parameters  $I_w$  and  $U_e$  were recorded using an automated system of data acquisition and processing, based on a personal computer of IBM PC 486 DX type. A special data file was created.

During teaching of the neural network the data of measurement of the instant values of welding current  $I_w$  and inter-electrode voltage drop  $U_e$  from this file were used. Processing of the instant values yielded derivative parameters that were introduced into the neural network:  $I_w$  is the effective value of current, averaged over  $t_w$ ;  $U_e$  is the effective value of inter-electrode voltage, averaged over  $t_w$ ;  $I_{w1}$ ,  $I_{w2}$ ,  $I_{w3}$ ,  $I_{w4}$  are the effective values of welding current, averaged over the respective intervals of time ( $t_w$  is divided into four intervals), the same goes for  $U_{e1}$ ,  $U_{e2}$ ,  $U_{e3}$ ,  $U_{e4}$  and for inter-electrode resistance  $R_{e1}$ ,  $R_{e2}$ ,  $R_{e3}$ ,  $R_{e4}$ . These parameters were introduced into the neural network in different combinations.

Teaching of the neural network was carried out at different number of neurons in the buried layer (3, 7, 10, 15) and was completed, when the maximal error of  $d_n$  forecasting was less than 5 % of the nominal value.

Teaching of the neural network was followed by its verification, using another sample of data, not included into the teaching sample.

The performed analysis showed that the best results on precision of  $d_n$  forecasting are demonstrated by neural networks with input parameters  $I_w$ ,  $U_e$  and  $I_w$ ,  $R_e$ , averaged over each of the four intervals  $t_w$ .

Neural network with input parameters  $I_w$ ,  $U_e$  is preferable for monitoring and control systems that use single crystal microcontrollers. The maximal absolute error of  $d_n$  forecasting for  $\delta = 0.8 + 0.8$  mm was  $\Delta_{\max} = 0.3$  mm (Figure 6).

Similar results on the precision of  $d_n$  forecasting were derived in welding specimens of the thickness of  $1.2 + 1.2$  and  $2.0 + 2.0$  mm.

To evaluate the quality of parts of the thickness from 0.8 up to 2.0 mm, using one neural network, one more input was added to it, to which  $t_w$  was applied. It was assumed, that specimens of different thickness were welded at different values of  $t_w$ . The conducted experiments showed that in this case forecasting of  $d_n$  is also possible, forecasting error, however, rising up to 12–13 %.

Thus, investigation of neural networks with different combinations of output parameters,  $I_w$ ,  $U_e$ ,  $R_e$  values and some others revealed, that quite good results of forecasting the quality during welding of the joints can be derived when using  $I_w$ ,  $U_e$  and  $t_w$  parameters. The calculation program can be executed



not only in a personal computer, but in a single crystal controller with limited computational resources, used to control the process of welding and the welded joint quality.

1. Podola, N.V., Rudenko, P.M. (1988) *Microcomputer-based automated systems for monitoring and control of resistance and arc welding on the base of a microcomputer*. Moscow: Mashinostroenie.
2. Paton, B.E., Podola, N.V., Gavrish, V.S. et al. (1998) Evaluation of the quality of resistance spot welding, using neural networks. *Avtomatich. Svarka*, **12**, 3–10.
3. Irving, B. (1997) Neural networks are raying off on the production line. *Welding J.*, **10**, 59–64.
4. Monari, G., Dieraert, O., Oberle, H. (1982) Predication of spot welding diameter using neural networks. *IIW Doc. III-1108–98*.
5. Zhawg, Z., Li, Y., He, X. et al. (1997) Artificial neural networks applied to spot welding process modeling. *China Welding*, **1**, 41–48.
6. Matsuyama, K. (1982) Nugget size sensing of spot weld based on neural network learning. *IIW Doc. III-1081–97*.
7. Diltthey, V., Dickersbach, J. (1982) Quality assurance of resistance spot welding by employment of neural networks. *IIW Doc. III-1093–97*.
8. Brown, J., Jobling, C., Williams, N. (1982) Optimization of signal inputs to a neural network for modeling spot welding of zinc coated steels. *IIW Doc. III-117–98*.
9. Satoh, T., Abe, H., Suzuyama, S. (1982) A trial of quality assurance in resistance spot welding by aid of neural network and fuzzy reasoning. *IIW Doc. III-1083–97*.

## EFFECT OF AN ELECTRODE METAL DROPLET ON ARC VOLTAGE IN GAS-SHIELDED WELDING

V. PONOMARYOV, A.V. da COSTA and A. SCOTTI

Federal University, Uberlandia, Brazil

Voltage drop at an electrode metal droplet and its effect on the arc voltage value have been determined. Geometrical parameters of the droplet and length of the arc have been estimated using a machine consisting of laser and high-speed digital video camera, by synchronously registering the arc voltage and welding current curves. It has been established that the voltage drop per unit length of the droplet may exceed the voltage drop gradient in the arc column, and the arc voltage may increase with growth of the droplet and reduction of the arc voltage.

**Key words:** MIG/MAG welding, metal transfer, droplet parameters, arc length, voltage drop at metal droplet, arc voltage

It is a well-known fact that there is a direct proportional relationship between the arc length and the arc voltage drop in MIG/MAG welding. However, an experimental investigation of this relationship is a difficult problem, as, on the one hand, an experimental evaluation of the arc length involves difficulties and, on the other hand, methods for direct measurement of the actual arc voltage as a sum of voltage drops in the near-electrode regions and at the arc column are based on the use of probes and are difficult to employ [1]. With the traditional approach to measurement of the arc voltage, in particular the voltage between a torch and a workpiece (below referred to as the measured arc voltage  $U_a$ ), voltage drops at the transition contact «torch–wire», at the electrode extension and electrode metal droplet are added to the actual arc voltage. Distinguishing the voltage drop at the arc column from the sum of voltage drops is a very complicated problem, as its variations are accompanied, as a rule, by variations in voltage at the electrode extension, droplet and near-electrode regions. Therefore, a challenge is to determine these additional components of the voltage drop between the torch and workpiece.

This article gives results of evaluation of the voltage drop at the electrode metal droplet,  $U_d$ , during

the process of its formation at the electrode wire tip.  $U_d$  is most difficult to measure, compared with two other voltage drops outside the arc (at the torch–wire contact and at the electrode extension). Moreover, if voltage drops at the torch–wire contact and electrode extension remain more or less constant during arc burning,  $U_d$  varies depending upon the geometrical size of the droplet.  $U_d$  also varies because of displacement of the anode spot over the droplet surface.

**Experimental procedure.** A series of experiments were conducted to evaluate the above phenomenon, using electrodes of low-carbon steel, stainless steel and aluminium, i.e. materials greatly differing in specific electrical resistance.

A power source with a pin-shaped external volt-ampere characteristic, ensuring the constant value of the welding current, was used to reduce the effect of factors which determine the value of the measured arc voltage. Since there is no self-adjustment of the arc under these conditions, the assigned arc length was maintained by regulating the electrode wire feed speed  $v_f$ . Owing to the constant welding current, the curve of the measured arc voltage corresponded in shape to the curve of the electrical resistance in this region of the welding circuit.

Geometrical parameters of a droplet, its shape and position at the electrode tip, as well as the arc length, were determined using an image registering unit consisting of a laser and high-speed digital video camera [2]. Synchronously with video camera filming, values

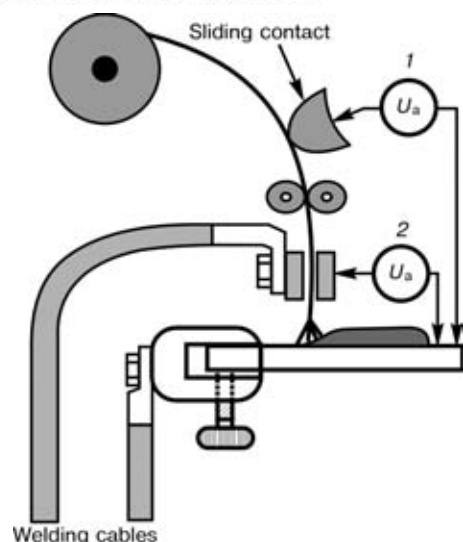


**Figure 1.** Variants of connection diagrams in measurement of the arc voltage under MIG/MAG welding conditions

of the arc voltage and welding current were measured using a PC-based measurement system.

To avoid inclusion of the voltage drop at the torch-wire transition contact into the measured arc voltage, the latter was determined according to diagram 1 shown in Figure 1, using a sliding carbon contact.

**Results and discussion.** Figure 2 shows an oscillogram of the measured arc voltage, as well as stages of formation and detachment of the electrode metal

droplet for the case of using low-carbon steel wire. The established value of the welding current (182 A) corresponds to conditions of a globular electrode metal transfer.

It can be well seen from the Figure that the arc voltage varies in a cyclic manner, i.e. it increases by 1.5–2.0 V with growth of a droplet, during which period the arc gap is reduced, and after detachment of the droplet it drops by the same value.

On the face of it, this result seems to contradict direct proportional dependence between the arc voltage and length. However, the observed variations in the measured arc voltage can be easily substantiated, if we assume that molten metal of the droplet has specific resistance which is higher than that of the arc column. In this case the measured arc voltage will grow with growth of the droplet and its replacement of the arc column, as growth of the voltage drop at the droplet is larger than decrease in the voltage drop at the arc column. It is assumed in this case that the voltage drop at the electrode extension, as well as the sum of the anode and cathode voltage drops remain unchanged.

Data of Figure 3 prove the assumption that specific voltage drop at the droplet may be very high, as specific electrical resistance of low-carbon steel in a molten state is 5–6 times as high as that at a tem-

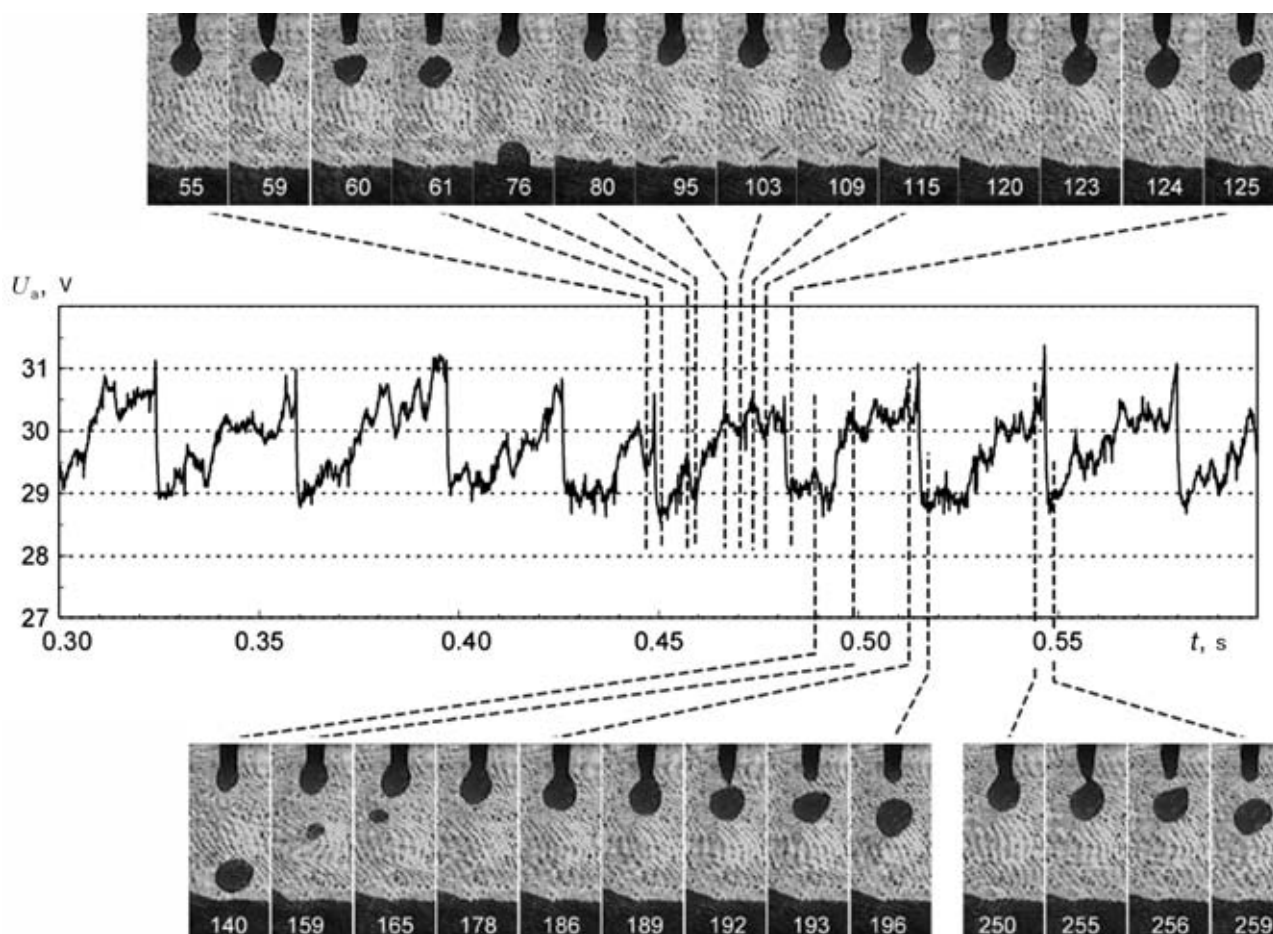


**Figure 2.** Variations in the arc voltage with formation and detachment of droplet in MIG welding using AWS ER70S6 low-carbon wire 1 mm in diameter (globular electrode metal transfer): shielding atmosphere — Ar + 2 % O<sub>2</sub>;  $I_w = 182$  A;  $v_f = 6.7$  m/min

perature of 200–300 °C (average temperature at the electrode extension [3]).

Variations in the arc voltage with the spray electrode metal transfer (Figure 4) are similar to those with the globular metal transfer. However, as the droplet has a small size and it is absorbed by the arc to a substantial degree (to be more exact, it is enclosed by the anode spot), the measured arc voltage with growth of the droplet increases to a lesser degree than in the case of the globular metal transfer.

To prove validity of the assumption that molten metal of the droplet in the case of using low-carbon steel wire has higher specific electrical resistance than the arc column, similar experiments were also conducted using electrode wires of stainless steel and aluminium.

The character and range of variations in the measured arc voltage in the case of using stainless electrode wire are close to those determined for low-carbon electrode wire (Figure 5). Despite the fact that at normal temperature the specific electrical resistance of stainless steel is almost 3 times as high as that of low-carbon steel, at high temperatures this parameter has close values for both steels (see Figure 3).

As opposed to low-carbon and stainless steel welding wires, in the case of using aluminium wire the measured arc voltage has an opposite character of variations (Figure 6), i.e. it gradually decreases with growth of the electrode metal droplet, and the arc gap is adequately reduced with its sudden increase after detachment of the droplet. The same character of variations in the arc voltage is indicative of the fact that in this case the droplet molten metal has a lower specific electrical resistance than the arc column.

**Determination of value of the voltage drop per unit length of the electrode metal droplet.** The suggested determination of value of the voltage drop per unit length of the electrode metal droplet,  $\Delta U_d$ , is based on analysis of variations of the measured arc voltage, arc length and length of the droplet at its

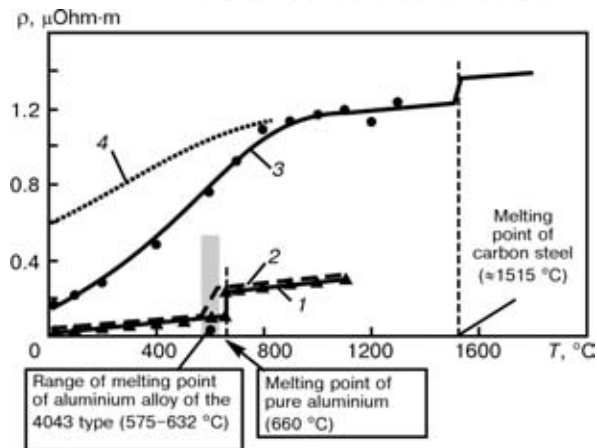


**Figure 3.** Temperature dependence of specific electrical resistance for pure aluminium (1), aluminium alloy of the 4043 type (2), carbon steel of the 1020 type (3) and stainless steel of the 430 type (4) [4–7]

detachment (see Figure 2). The procedure described is applicable to conditions of the globular electrode metal transfer, when the anode spot is comparatively small and does not enclose (does not shunt) the droplet. This analysis requires selection of such video frames where the droplet is in a co-axial position with respect to the electrode. This allows an assumption that the anode spot is at a lower part of the droplet, i.e. the droplet and the arc can be regarded as two resistances connected in series. Based on this analysis, we find that (Figure 7)

$$U_{a1} = U_{el} + U_{c+a} + U_{a1,c} + U_d, \quad (1)$$

$$U_{a2} = U_{el} + U_{c+a} + U_{a2,c}, \quad (2)$$

where  $U_{a1}$  and  $U_{a2}$  are the measured arc voltages before and after detachment of the droplet;  $U_{el}$  is the voltage drop at the electrode extension; and  $U_{a1,c}$  and  $U_{a2,c}$  are the voltage drops at the arc column before and after detachment of the droplet.

Voltage drop at the electrode extension,  $U_{el}$ , before and after detachment of the droplet does not vary, as length of the electrode extension remains

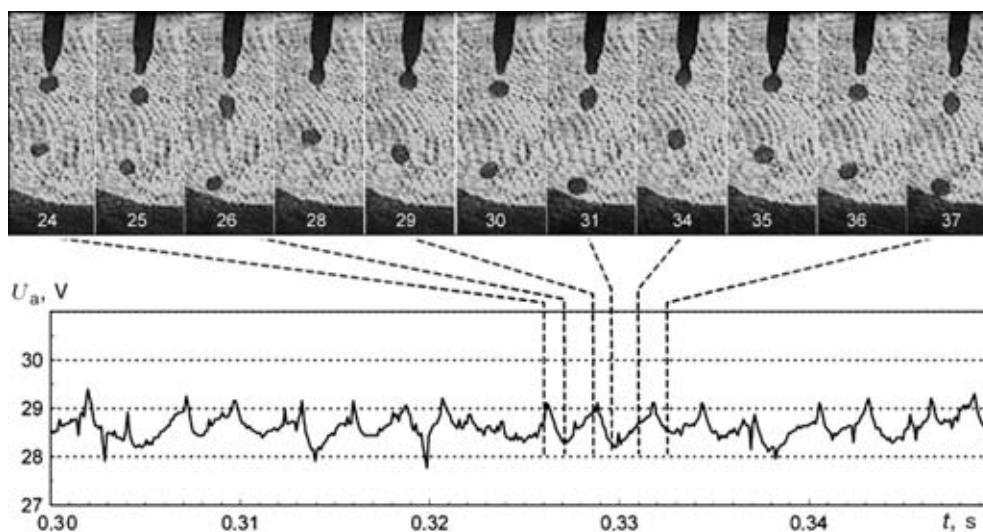


**Figure 4.** Variations in the arc voltage with formation and detachment of droplet in MIG welding using AWS ER70S6 low-carbon wire 1 mm in diameter (spray electrode metal transfer): shielding atmosphere — Ar + 2 %  $\text{O}_2$ ;  $I_w = 210$  A;  $v_f = 8.7$  m/min

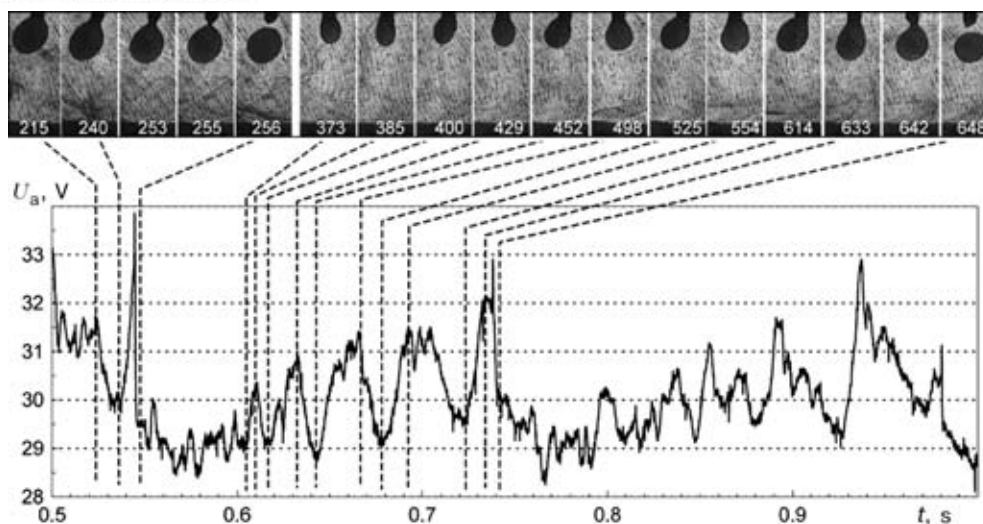


**Figure 5.** Variations in the arc voltage with formation and detachment of droplet in MIG welding using AWS ER308LSi stainless steel wire 1.2 mm in diameter (globular electrode metal transfer): shielding atmosphere — Ar + 2 % O<sub>2</sub>;  $I_w = 134$  A;  $v_f = 3.0$  m/min

constant (see Figure 2) (allowing for the residual droplet of molten electrode metal).

It is also assumed that at the moments before and after detachment of the droplet the sum of the cathode and anode voltage drops,  $U_{c+a}$ , and the voltage drop per unit length of the arc column,  $\Delta U_{a.c}$ , do not vary to a substantial degree. Allowing for the last assumption, we find the following expression for the voltage drop at the arc column:

$$U_{a.c} = \Delta U_{a.c} L_a, \quad (3)$$

where  $L_a$  is the arc length.

Substitution of terms  $U_{a1.c}$  and  $U_{a2.c}$  into equations (1) and (2), allowing for equation (3) and subtracting equation (2) from (1), yields expression for the voltage drop at the electrode metal droplet:

$$U_d = (U_{a1} - U_{a2}) + \Delta U_{a.c}(L_{a2} - L_{a1}). \quad (4)$$

Increment in the arc length after detachment of the droplet is equal to the length of the droplet. Therefore, expression (4) can be written as follows:

$$U_d = (U_{a1} - U_{a2}) + \Delta U_{a.c} L_d. \quad (5)$$

Difference in the measured voltage drop before and after detachment of the droplet is determined from the  $U_a$  oscillogram (see Figure 2), and for the case under consideration it is 1.2 V on the average.

Preliminary experiments showed that the voltage drop per unit length of the arc column,  $\Delta U_{a.c}$ , for the given welding conditions was approximately equal to 0.7 V/mm, which is in good agreement with the data of [1].

While measuring the length of the droplet, it is necessary to bear in mind that the line of conjugation of the arc with the droplet passes a bit higher than the lower part of a visible contour of the droplet. Therefore, the length of the droplet should be measured with a certain shift to the centre of the droplet. It is postulated for the globular metal transfer that this shift is 0.25 of the electrode wire diameter. The length of the droplet at the moment of its detachment,  $L_d$ , is determined from the video frames, and in the case under consideration it is 1.8 mm on the average.

Therefore, for the given welding conditions the average values of the total voltage drop at the droplet and voltage drop per its unit length are, respectively, as follows:

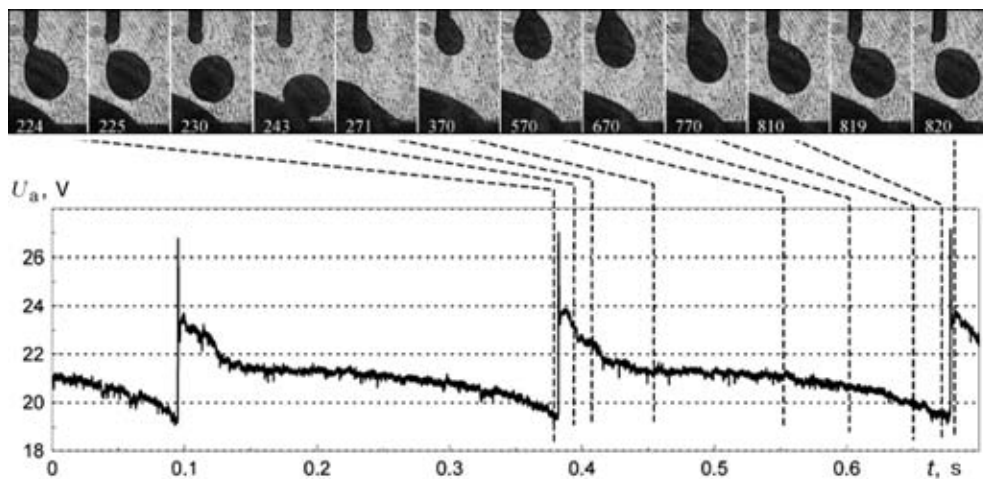


**Figure 6.** Variations in the arc voltage with formation and detachment of droplet in MIG welding using AWS A5.10-88 aluminium wire 1.2 mm in diameter (globular electrode metal transfer):  $I_w = 95$  A;  $v_f = 4.8$  m/min



$$U_d = 1.2(\text{V}) + 0.7(\text{V}/\text{mm}) \cdot 1.8(\text{mm}) = 2.46(\text{V}), \quad (6)$$

$$\Delta U_d = 2.46(\text{V}) / 1.8(\text{mm}) = 1.37(\text{V}/\text{mm}). \quad (7)$$

As shown by the results obtained, the voltage drop per unit length of the droplet may substantially exceed the voltage drop per unit length of the arc column. This leads to the fact that the principle of self-adjustment of the arc length may not be met in each separate cycle of formation and detachment of the droplet. However, it is natural that with variations in the mean arc length (where the mean arc length has grown or, on the contrary, decreased for any reason whatsoever) the principle of self-adjustment of the arc length does take place because of variations in the total resistance of the «droplet + arc» system.

The results obtained also suggest that the efficiency of self-adjustment of the arc length is higher for materials with lower specific electrical resistance, e.g. in the case of using aluminium electrode wire, as the principle of self-adjustment of the arc in this case will take place both in general and in each separate cycle of formation and detachment of the droplet. In addition, it is necessary to take into account that welding conditions with the globular metal transfer are usually not applied in practice; hence, the negative effect of the voltage drop at the droplet in MIG/MAG welding is relatively low.

## CONCLUSIONS

1. Voltage drop at the molten electrode metal droplet in MIG/MAG welding has a significant effect on a value of the measured arc voltage between the nozzle and workpiece.

2. Voltage drop at the droplet depends upon the welding current, specific electrical resistance of the electrode material (in liquid state), shape and size of the droplet and position of the anode spot on the droplet surface.

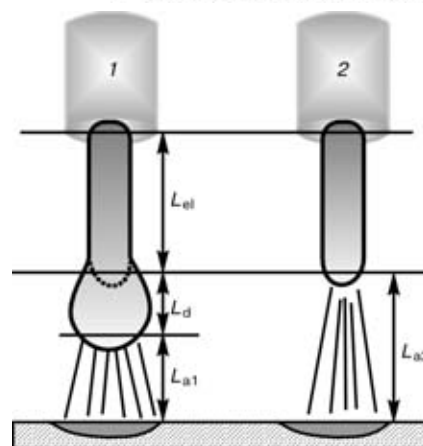


**Figure 7.** Schematic of two successive steps of electrode metal droplet transfer: 1 — droplet at the electrode tip prior to detachment; 2 — moment after detachment of the droplet

3. High voltage drop at the droplet may lead to decrease in the efficiency of self-adjustment of the arc length.

The authors express gratitude to the Division of Post-Graduate Studies at the Mechanical-Engineering Department of the Federal University of Uberlandia, Brazil, as well as organisations CNPq and FAPEMIG for their financial support in performance of this work.

1. Lenivkin, V.A., Dyurgerov, N.G., Sagirov, Kh.N. (1989) *Technological properties of welding arc in shielding gases*. Moscow: Mashinostroenie.
2. Balsamo, P.S.S., Vilarinho, L.O., Vilela, M. et al. (2000) Development of an experimental technique for studying metal transfer in welding: Synchronized Shadowgraphy. *ASM Int. J. Joining of Materials*, 4, 48–59.
3. Huismann, G., Hoffmeister, H. (1988) Reactions of current and metal transfer on unsteady wire transport in MIG welding with respect to hyperbaric conditions. In: *Proc. of 5th Int. Conf. on Trends in Welding Research*, Pine Mountain, Georgia, USA, June.
4. (1978) *ASM Metals Handbook*. Vol. 1. Physical properties of carbon and low-alloy steel. ASM.
5. (1999) *ASM Guide to engineered materials. Adv. Materials & Processes*, 12.
6. Hatch, J.E. (1984) *Properties and physical metallurgy*. Ohio: ASM.
7. Smithells, J.S., Brandes, E.A., Brook, G.B. (1998) *Smithells reference book*. Butterworth-Heinemann.



# FUSION WELDING OF DISPERSION-STRENGTHENED ALUMINIUM-BASED COMPOSITE MATERIALS, CONTAINING SILICON CARBIDE PARTICLES (REVIEW)

E.V. CHEREPIVSKAYA and V.R. RYABOV

The E.O. Paton Electric Welding Institute, NASU, Kyiv, Ukraine

A review of the current methods of fusion welding of Al-based dispersion-strengthened composite materials (DSCM), reinforced with silicon carbide particles is presented. Processes, proceeding in arc welding of Al-based DSCM are considered in detail. Mechanical characteristics of welded joints on composite materials are given, and problems, arising in their fusion welding, are considered.

**Key words:** *composite material, fusion welding, aluminium matrix, reinforcer, particle, silicon and aluminium carbides, decomposition, structure, composition*

Among the currently available DSCM the most widely accepted are composites, reinforced with SiC particles, where the volume fraction may change from 10 up to 50 %. This, naturally, results in the change of composition, structure and mechanical properties of the above materials that determine selection of the welding process. This paper provides analysis of published data on the quality and properties of joints of composite materials (CM) under the conditions of fusion welding.

**Arc welding.** In welding of Al-based DSCM, reinforced with SiC particles, high-temperature heating leads to several problems [1–7]: these particles decomposition due to high-temperature heating in welding, thus resulting in the loss of the initial CM properties; high toughness of the weld pool metal; difficulty of producing sound welds as a result of poor wetting of SiC particle surface with aluminium; porosity and embrittlement of welds. Another one arises in CM welding, using filler wire — base metal dilution with the wire metal and, as a result, transition of reinforcing particles from the base into the weld metal. In the latter the particles are non-uniformly distributed over the volume due to different densities of aluminium alloys ( $\sim 2698 \text{ kg/m}^3$ ) and silicon carbide ( $\sim 3210 \text{ kg/m}^3$ ): their clusters are found in the weld root, while in the upper part of the weld these particles are practically absent. However, even in the weld root metal their number is smaller than in the base metal. The low content of reinforcing particles in the weld zone metal and absence of mixing of the base metal and the filler result in a lower strength of the welds in relation to the composite material strength.

Earlier attempts to join CM of SiC–Al system by fusion welding led to items with an inadmissible high level of porosity, delaminations near the base–weld

metal interface and low strength. High toughness of weld metal made it difficult to achieve its good spreading.

In arc welding of CM, where the volume fraction of SiC was 12–14 %, with an aluminium matrix of AMg5 (1550) or AD33 (1330) the influence of the reinforcing particles on the arc discharge behaviour and weld appearance was noted. An unstable nature of the arc discharge is observed during welding: arc erring and a characteristic noise are noted. A dark precipitate forms on the weld face that is easily removed later on. In the case of application of filler materials of aluminium alloys, the arc distortion becomes noticeably smaller, and the weld acquires a light-gray colour. Arc welding of such CM may lead to formation of plate-like  $\text{Al}_4\text{C}_3$  phases by the following reaction:  $4\text{Al} + 3\text{SiC} \rightarrow \text{Al}_4\text{C}_3 + 3\text{Si}$ .

$\text{Al}_4\text{C}_3$  phase may also form during interaction of aluminium with free carbon, present in SiC particles [8]. In addition,  $\text{Al}_4\text{SiC}_4$  and  $\text{Al}_8\text{SiC}_7$  compounds may form in this system at temperatures above  $1400^\circ\text{C}$  [9]. In [10, 11] it was shown that silicon addition to the matrix alloy allows an essential slowing down or even complete elimination of the occurrence of the above reaction under certain conditions. It was found [7] that the quantity of SiC particles and  $\text{Al}_4\text{C}_3$  phase formed in the fusion zone, is the function of specific energy density (Figure 1).

Intensive heating in welding destroys SiC particles and promotes formation of a large number of rather coarse  $\text{Al}_4\text{C}_3$  plates in the melting zone (carbon solubility in aluminium at the temperature of  $1100^\circ\text{C}$  is practically zero, at  $1300$ – $1500^\circ\text{C}$  it is equal to 0.2–0.4 % and later it increases with temperature). Presence of coarse particles of  $\text{Al}_4\text{C}_3$  is undesirable for CM, as it leads to degradation of the mechanical properties of the material. In addition, appearance of a large amount of  $\text{Al}_4\text{C}_3$  phase promotes its reacting with water and moisture. Investigations also showed that in the weld metal structure, in addition to  $\text{Al}_4\text{C}_3$ , a considerable amount of  $\text{Al}_4\text{Si}_2\text{C}_5$  phase is observed that has the form of plates. The acicular form of  $\text{Al}_4\text{C}_3$

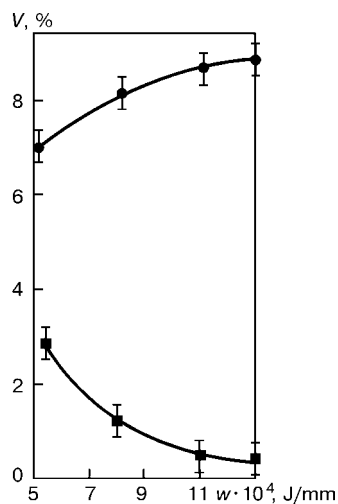


**Figure 1.** Dependence of volume fraction  $V$  of  $\text{Al}_4\text{C}_3$  (●) and  $\text{SiC}$  (■) particles on specific energy density  $w$  in welding of CM of Al-6.2Mg alloy [7]

phase may induce stress concentration at application of load to a part, made of a composite material. In order to slow down the above reaction, it is recommended [12] to apply a Si-rich filler of aluminium, for instance, ER4043 with the weight fraction of Si of 4.5–6.0 % (AK-5 type) or ER4047 (10–13 % Si).

TIG welding of a composite material based on 6061 with 20 vol.% SiC turned out to be quite successful with application of ER4043 filler wire [12]. In this case alloy 6061, produced by the method of powder sintering, was initially degassed under vacuum. Typical modes of argon-arc welding of composites, based on alloys 2080 and 7475 with 20 vol.% SiC and mechanical properties of their welded joints are given in Table 1. As can be seen from the Table, joints made without a filler have a higher strength than those made with ER4047 filler. Post-weld heat treatment of a weld made with a filler, enhances the welded joint strength.

Work [3] gives the results of experiments on CM welding (a mixture of thin fibres or whiskers and SiC particles with an aluminium matrix) with about 20–50 % volume fraction of the reinforcer, depending on

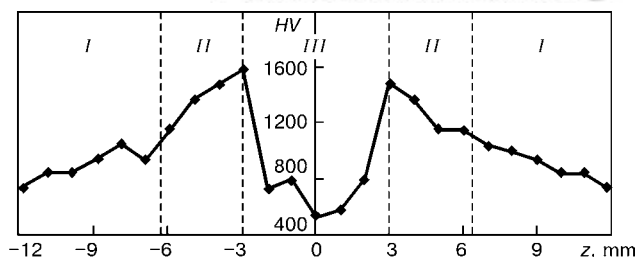


**Figure 2.** Hardness distribution across the joint of CM based on alloy 6061 with 18.4 vol.% SiC, produced by TIG welding with ER4043 filler [3]: I–III — zones of base metal, HAZ and weld, respectively

the grade of the material used. SiC whiskers are of 0.2–1.0  $\mu\text{m}$  diameter and up to 50  $\mu\text{m}$  length, and also have quite good mechanical properties ( $\sigma_t \approx 13 \text{ GPa}$ ,  $E \approx 700 \text{ GPa}$ ). CM of 6061 alloy with 18.4 vol.% SiC made by the powder metallurgy methods was selected to study the weldability. A feature of such a CM is the ability to form the billets into the required shapes (rods, pipes, sheets, etc.), using the traditional processing methods. TIG and MIG welding were used to produce joints of the selected CM, the modes are given in Table 2.

Attempts at CM welding without degassing led to joints with inadmissible high pore density. It was found that vacuum degassing prior to welding may reduce the number of pores. Metallographic and X-ray structure analysis of the metal used for welding after degassing and heat treatment showed that a certain amount of SiC in it decomposed, forming Al–SiC and  $\text{Al}_4\text{C}_3$  eutectics. Apparently, formation of pores in the weld metal is unrelated to eutectic formation [3]. A butt joint with a gap was used to provide a complete penetration of CM. In this case no discontinuities between the base and weld metal, or delaminations were found.

Figure 2 shows a typical curve of hardness distribution across a welded joint of a CM, based on 6061 alloy with 18.4 vol.% SiC (without heat treatment). Base metal hardness after its degassing in vacuum is HV 800–900; in the HAZ metal it gradually increases

**Table 1.** Results of rupture testing of flat samples of DSCM joints in AC welding [12]

Welding current, A	Voltage, V	Heat input, kJ/mm	Kind of post-weld heat treatment	Filler material	$\sigma_v$ , MPa	Fracture site
<i>Alloy 2080 + 20 vol.% SiC</i>						
154	12.0	1.09	Quenching + ageing	ER4047	218	In the filler
145	11.5	1.54	Same	Same	196	Same
149	12.0	1.29	»	»	153	»
147	11.5	1.15	»	»	175	»
147	12.8	0.90	After welding	»	145	»
90	10.6	0.39	Same	Without filler	306	In weld center
90	10.6	0.39	Quenching	Same	296	Same
<i>Alloy 7475 + 20 vol.% SiC</i>						
64	10.4	0.19	After welding	»	307	In base metal
64	10.4	0.19	Quenching + ageing	»	396	Same

**Table 2.** Parameters of the mode of welding CM based on 6061 alloy with 18.4 vol.% SiC [3]

<i>Argon-arc welding</i>	<i>Welding speed, m/h</i>	<i>Heat input, kJ/mm</i>	<i>Welding current, A</i>	<i>Voltage, V</i>	<i>Argon flow rate, l/s</i>	<i>Kind of filler material</i>
Consumable electrode	300–375	1.9–2.2	100–110	19–20	16.5–19.0	Al-3Mg
Non-consumable electrode	150–200	1.7–2.2	145–160	12–14	5.7–7.1	4043

*Note.* CM sample thickness is 3.2 mm; gap width in the weld butt root is 1.5 mm.

up to *HV* 1500–1600, and then drops to *HV* 600 in the weld metal. Increased hardness of the HAZ metal, not characteristic for the majority of not heat-hardenable monolithic aluminium alloys, shows that fracture of such a joint in tension may occur across the weld. The causes for hardness increase in the HAZ have not been studied — it is, probably, due to formation of small precipitations during aluminium reaction with SiC that act as a dislocation barrier.

Heat treatment of welded joints by T6 mode (773 K, 8 h, argon) leads to increased hardness of base metal up to the hardness level of as-manufactured material (*HV* 1200–1400). Welds, made with non-consumable electrode on a material after degassing, had the strength  $\sigma_t \approx 179$  MPa that in its magnitude is close to that of the strength of wrought aluminium alloys. All the welded joints failed in the weld. As regards welds made with the consumable electrode the results were diverse. Values of  $\sigma_t$  at tension were  $\approx 255$  MPa in them, because of application of ER5356 wire (Al–Mg type). In terms of metal strength, the obtained welds are equivalent to wrought alloys, welded using ER4043.

A feature of CM welding is lower fluidity of weld pool metal at simultaneous increase of the content of reinforcing particles. To guarantee metal penetration in the weld root, the filler wire should be lowered into the weld pool, and the sample edge preparation angle should not less than 90°. Aluminium wettability with SiC particles being poor, it is necessary to use welding wires, providing a high fluidity of the metal. Used with this purpose are welding wires with about 5 wt.% Si (AK-5 type). They allow weld metal composition to be improved and high weld quality to be achieved, respectively. As a rule, standard rigging, applied for arc welding of aluminium and its alloys, is used in welding CM without any changes [13].

Work [13] is devoted to studying the weldability of a CM based on 2124 alloy of Al–Mg–Cu system with 20 vol.% SiC. This alloy is usually regarded as unweldable, because of hot cracking [14] and low content of silicon, thus causing disintegration of SiC particles and formation of  $Al_4C_3$  phase in the welding zone. Earlier attempts at solving the problem of insufficient fluidity were reduced to increasing the heat input into the welding zone, the probability of SiC decomposition being, however, increased. Samples of 3 mm thickness with a V-shaped edge preparation (45°) were used for TIG welding. Samples were welded, using melting mushroom-shaped inserts, the «mushroom» cap forming the back reinforcement of

the weld. The best results — complete melting and absence of  $Al_4C_3$  formation were derived at the heat input of 1.25 kJ/mm. Below this value, no penetration of the weld root was recorded, and  $Al_4C_3$  formation was observed above this value. It was shown that a small amount of  $Al_4C_3$  forms in the upper part of the deposited metal at the heat input into the welding zone on the level of 1.0–1.3 kJ/mm. This layer may be removed by machining. Thus, use of melting inserts turned out to be successful. Authors of [13] also conducted experiments on welding tubes of 25.4 mm diameter and wall thickness of 1.05 mm. Regular rigging was used, that is applied for welding thin-walled tubes. Welding was performed in the following modes:  $I_w = 92$ –100 A,  $v_w = 177$ –320 mm/min (2.05–5.30 mm/s),  $U_a = 9.5$ –13.0 V, this corresponding to heat input levels of 0.169–0.305 J/mm. Considering the small thickness of the tube wall, such heat input values guarantee the complete penetration and formation of the joint. It was, however, impossible to completely avoid the formation of aluminium carbide in this series of experiments: similar to welding of plates, a small amount of it formed in the upper part of the weld metal.

In work [15] experiments were conducted on welding cast samples of DSCM, based on a cast alloy AL2 with about 10 vol.% SiC, produced by the method of mechanical mixing into the melt. Welding was conducted in argon with 4 mm tungsten electrode at AC in the modes, given in Table 3. The selected DSCM welding modes provide a satisfactory formation of welds: they are smooth without undercuts with slag films visible on weld surface along the weld line (mode 1) or in the periphery at weld edge (mode 3). Weld microstructure examination revealed the presence of reinforcing particles in the weld metal. However, zones without these particles form near the fusion line, as well as in the weld center near its surface. Now, in those areas where SiC particles are present in the weld metal, a tendency to formation of their clusters (agglomeration) is found. The most homogeneous microstructure of the welded joint metal could be produced in the mode with the lowest heat input (mode 2). In this case, a practically complete absence of zones, free of reinforcing particles, is observed. Thus, the result of fusion welding of DSCM based on cast aluminium alloys reinforced with SiC particles depends on selection of welding modes.

The [16] describes the process of fusion welding of metal-matrix CM, where the matrix can be not only of aluminium, but also magnesium, titanium and iron



alloys. The method consists in feeding the reinforcing material into the welding zone through a consumable electrode, containing particles of a reinforcer, or in the form of powder through a tube. The impact of the arc results in formation of a liquid metal pool, where the dimensions depend on welding speed. It is preferable to feed the reinforcing material into that part of the pool that has a lower temperature prior to the start of solidification. The powder feed rate depends on pool dimensions, as well as the ratio of the content of the reinforcer and the matrix metal, that must be achieved in the weld metal. This ratio should be adjusted considering that the presence of a large number of SiC particles in the molten metal of the pool may increase its toughness, thus impairing the metal fluidity and weld characteristics. As the high temperatures and arc pressure promote decomposition of particles, the volume fraction of particles fed into the pool, should be predetermined to compensate for these drawbacks. The range of volume concentration of reinforcing particles for each specific system may vary, but, as stated by the authors of [16], it is limited to 12–20 %.

The nature of weld solidification and redistribution of reinforcing particles in the composite in welding depends on the temperature and time conditions of the process, related to the basic welding parameters (heat source intensity, welding speed, conditions of heat removal from the melting zone), as well as thermo-physical properties of the metal being welded. In work [17] a special rigging in the form of heat-removing sectioned clamps was used to study the influence on the nature of weld solidification and redistribution of reinforcing particles in the composite. They, on the one hand, allow a fast heat removal from the weld, and, on the other, promote reduction of deformations during welding and after it. Irrespective of the kind of filler wire, however, the metal reinforcing phase is non-uniformly distributed. A tendency is found to formation of clusters of the reinforcing particles and zones, free of them. Such a non-uniformity of the reinforcing filler distribution in the weld metal is, possibly, connected to convective flows in welding.

**Laser and electron beam welding.** Most of the work devoted to laser welding pertains to DSCM of Al–SiC system. Continuous wave and pulsed CO<sub>2</sub> lasers were tried out for welding CM based on aluminium alloy A-356. In order to prevent the formation of Al<sub>4</sub>C<sub>3</sub> phase, a high welding speed and a sharply-focused beam of 0.4 mm diameter are recommended [13].

Studied [18] is the possibility of laser and arc welding of CM with an aluminium matrix with about 15 vol.% SiC. CO<sub>2</sub> laser of 3 kW power was used. Welding was performed at various speeds in argon and without it. TIG welding was performed by continuous and tack welds. Acicular inclusions of Al<sub>4</sub>C<sub>3</sub> were found in the structure of metal of a laser weld. Higher welding heat input leads to coarsening of the above inclusions, sensitive to moisture. The hardness

**Table 3.** Modes of welding samples of CM based on AL2 alloy with 10 vol.% SiC [15]

Mode No.	Welding current, A	Voltage, V	Welding speed, m/h	Weld size, mm	
				<i>b</i>	<i>h</i>
1	330	16	12	14–15	4.5–5
2	365	14	30	10–11	4–4.5
3	16	50	0.38	2.5–3	–

of weld metal is higher than that of base material, and in mechanical strength testing fracture runs through the weld metal without any signs of plastic deformation. Fractographic studies showed that this fracture proceeds along the interphase. Tungsten-electrode arc welding in helium is also accompanied by formation of Al<sub>4</sub>C<sub>3</sub> inclusions, the quantity and size of which are much greater than in laser welding.

In work [19] studied was the influence of low heat input and short time of the welding thermal cycle on the microstructure of a weld produced in laser welding of a CM with 15 vol.% SiC. Continuous wave CO<sub>2</sub> laser and pulsed Nd:YAG laser were used at different input power and welding speed. Laser welding with a low heat input and short thermal cycle allows prevention of Al<sub>4</sub>C<sub>3</sub> phase formation in the fusion zone metal. A qualitative model of transformations was constructed for understanding the sequence of its microstructure variation, depending on the effective maximal temperature, as well as soaking at this temperature (depending on the distance from the weld central line). This model showed that in the centre of the fusion zone, SiC particles dissolve in liquid aluminium with formation of a homological liquid at the temperature of welding. Cooling leads to the following phases precipitation from the liquid: initially Al<sub>4</sub>C<sub>3</sub>, then primary Si and, finally, Al–Si eutectic. According to the model, partial dissolution of SiC particles takes place in the intermediate area of the fusion zone. An Al<sub>4</sub>C<sub>3</sub> phase forms in cooling that initiates and grows on these partially dissolved particles. Al–Si eutectic forms of the remaining liquid. In the outer areas of the fusion zone, the soaking temperature and time of the thermal cycle are insufficient for SiC particles to be dissolved. However, the aluminium matrix solidifies as Al–Si eutectic as a result of exceeding the liquidus temperature of the hypoeutectic alloy. Weld microstructure produced in welding with the pulsed laser is similar in its phase composition to that found in the metal of welds produced with CO<sub>2</sub> laser, but is usually finer in size.

Work [20] is a study of weldability of samples of a CM based on matrix alloy A-359 with 20 vol.% SiC, of 80 mm length and 6×30 mm cross-section. Mechanical properties of this alloy and CM on its base are given in Table 4. A pulsed Nd:YAG laser was used. The high radiation power (5 kW) and speed of 30 m/h lead to formation of a large amount of Al<sub>4</sub>C<sub>3</sub> phase and primary Si with a decrease of SiC content. In welding in the mode with 3.5 kW and 90 m/h,

**Table 4.** Mechanical properties of matrix alloy A-359 and CM on its base [20]

Material	$E$ , GPa	$\sigma_t$ , MPa	$\delta$ , %	$\rho$ , g/cm <sup>3</sup>
A-359	72	330	6.0	2.68
A-359 + 20 vol.% SiC	114	375	1.0	2.75

*Note.* Composition of alloy A-359, wt.%: Si — 9.0; Mg — 0.6; Al — balance.

the welded joint microstructure is similar to that of the base metal, no aluminium carbide is formed, and a good penetration of the material with the laser beam to the depth of 4.5 mm is achieved. Use of nitrogen, helium and argon as shielding gases (flow rate of 5 dm<sup>3</sup>/min) does not affect the welded joint structure.

Such a defect as boiling is observed in laser welding. Such a phenomenon has never been observed in any of the materials, welded with a high energy density source [21, 22]. The cause for that was the feature of the material structure and its behaviour under specific conditions, arising in the penetration channel in welding with a powerful laser. Analysis of the physical mechanism of the process demonstrated that boiling may be eliminated only by its suppression. Applying longitudinal-transverse beam oscillations at the frequency of 50 Hz and amplitude of 2 to 3 mm may be used as a technique, ensuring such suppression.

Work [23] is a study of the features of EBW of CM based on aluminium alloy A-356 with 15 vol.% SiC. Welding was performed at the speed of 30.5 m/h with the heat input of 0.18–0.36 kJ/mm, using a defocused electron beam. The metal of the melting zone in the welded joint is characterized by a good structure and uniform distribution of SiC particles. Inclusions of Al<sub>4</sub>C<sub>3</sub> particles in the weld zone are very few, being of an acicular shape, not less than 20  $\mu$ m long and located at the welded joint top. With greater defocusing of the beam the size of Al<sub>4</sub>C<sub>3</sub> needles increases. No reaction was observed on the particle–matrix interface in scanning electron microscopy examination. The work confirms the advantage of EBW over laser welding, because of the difference in the mechanism of energy absorption in these two processes, as well as reports a successful application of welding processes with a short thermal cycle.

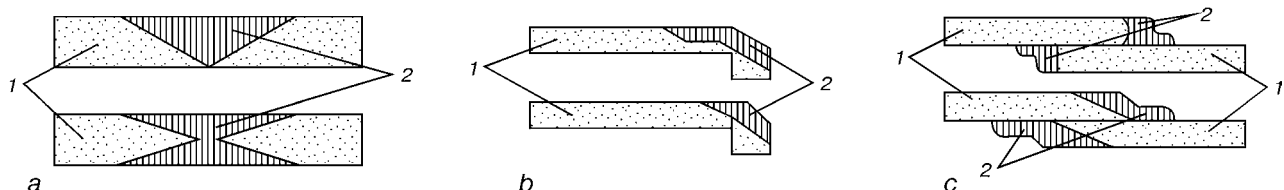
An interesting technique used in EBW [17] is application of an embedded element of a material identical to the matrix material. In welding dilution of the embedded element metal with the base metal melt and reinforcing particle transition into the weld metal

are found. The number of particles in the latter is much smaller than in the base metal.

The PWI developed a process of electron beam melt dispersion that consists in creating a directed flow of melt drops by centrifugal sputtering from the side surface of a cylindrical billet rotating in vacuum, and subsequent transfer with a uniform distribution of the drops on a heated form-shaping surface and their directed solidification [24]. This process can be used with the appropriate edge preparation (Figure 3) for fusion welding of low-ductility alloys and CM without partial melting of the base material (ceramics, dissimilar, difficult-to-weld and unweldable materials) [25].

Experiments were conducted in U-212M unit with a vertical location of the electron beam gun, which was powered from U-250A source with the accelerating voltage of 30 kV. The consumable sample was made of aluminium alloy AL25 of 100 mm diameter. Rotation was imparted to the consumable billet by D-90A motor with a smooth adjustment of the rotation speed. The latter was varied in the range of 1800–3100 rpm. The beam was controlled using a discrete scanning instrument with a set of scan patterns that allowed adjustment of beam power density within the heated spot. Conditions can be set up for distribution of the beam power density in the heated zone, allowing successful control of both the instant volume of molten metal and dimensions of the liquid melt pool, and direction of sputtering of the metal of the billet rotating at a high speed, and, therefore, also the dimensions (volume) of the liquid drops, transferred by the centrifugal force to the target. The role of CM preheating temperature and method of surface preparation were determined to evaluate the degree of adhesion bonding of the melt with the material of the substrate onto which the sprayed material was deposited. Mechanical testing and metallographic examination of the joints produced by the above technology showed that the optimal temperature range of edges preheating is from 0.50 to 0.65 of substrate melting temperature. Comparison of  $\sigma_t$  values of the deposited dispersed melt and commercial silumins shows that by the rupture strength values the coatings produced by deposition of liquid metal drops correspond to silumins.

Considering the results of optimising the dispersion parameters, samples of aluminium composites with 18 vol.% SiC were prepared for welding with alloy AL25 used as filler. Good wetting and spreading of the filler material along the base metal edges being welded are observed at the transition boundary. Such a joint does not have any defects. Unlike welding

**Figure 3.** Welded joints made using melt dispersion [25]: *a* — butt; *b* — fillet; *c* — overlap; 1 — base metal; 2 — filler metal

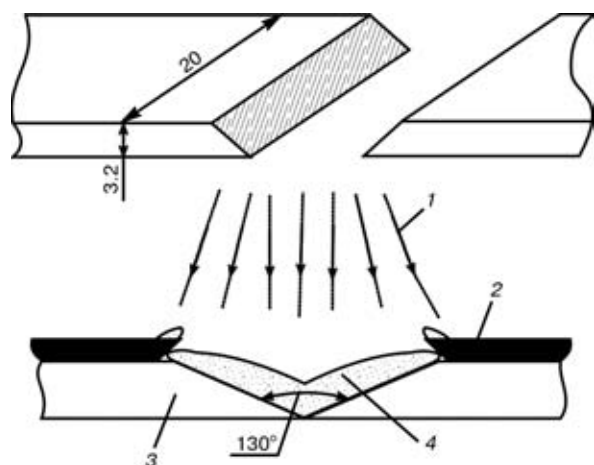


**Figure 4.** Schematic of the spraying process [26]: 1 — sprayed particles; 2 — protective mask; 3 — material deposited by spraying; 4 — base material

with surface melting of the edges in the matrix material directly at the transition boundary, the particles of SiC reinforcer did not undergo any noticeable changes (for instance, decomposition), nor was their bond with the matrix material disturbed. The filler metal is dense, without visible defects, while the dispersion of its structural and phase components is by an order of magnitude lower than that of the base metal. Thus, analysis of the results of the conducted mechanical testing and metallographic examination leads to the conclusion that sound joints of CM without surface melting of the base material edges can be produced in vacuum, using electron beam melting and dispersion of the filler.

**Joining by the plasma spraying process.** Plasma spraying is one of the possible methods of joining CM parts. The features of joining CM based on 6061 alloy with different volume fractions of reinforcing SiC particles (10 and 20 %) were studied in [26, 27]. Samples were 20 mm wide, 3.2 mm thick with the bevel angle of 130°. The face surface of the joint zone was treated with sand paper to produce greater roughness, which was followed by samples welding without a gap in the weld root. A composite powder based on alloy 2014 with 15 vol.% SiC was used for spraying, where the diameter of the granules was 45 to 150  $\mu\text{m}$ .

Schematic of plasma spraying is shown in Figure 4. The nozzle for spraying makes reciprocal motions with the speed of 0.21 m/s normal to the sample. Spraying is conducted until the weld thickness in the centre of the joint zone has reached the sample thickness. It is experimentally established that the optimal distance between the nozzle and the joint is 95 mm, and pre-heating temperature is 473 K.

Hot isostatic pressing (773 K, 1 h, 103.4 MPa), as well as heat treatment of the joints by T6 mode were performed to improve the wettability of the base metal with the deposited metal, increase the joint strength and reduce the microporosity of the joint zone after spraying. Quenching with subsequent water cooling was followed by ageing of welded samples at the temperature of 433 K for 18 h.

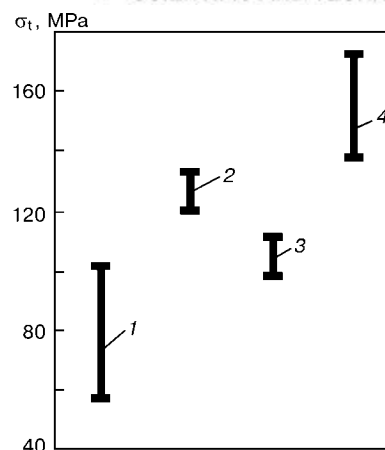


**Figure 5.** Change of ultimate tensile strength  $\sigma_t$  at tension of joints (alloy 2014 with 15 vol.% SiC), made by plasma spraying without heat treatment and after its diverse types and combinations [27]: 1 — right after spraying; 2 — after ageing heat treatment (T6); 3 — after HIP; 4 — same after subsequent ageing

Investigation of the structure of welded joints after hot isostatic pressing yielded the following results. While prior to the composite powder spraying the volume fraction of SiC in it was 12–15 %, in the deposited metal it was only 8.5 %. The main cause for the reduced content of SiC is its thermal decomposition in the plasma flow. In this connection, the dispersity of SiC particles in the base material is higher than that in the deposited material. Initial supposition about a reaction proceeding between the aluminium of the matrix and carbon during spraying was not confirmed, as subsequent metallographic examination demonstrated a complete absence of  $\text{Al}_4\text{C}_3$  phase in the deposited metal. However, a great quantity of dissolved silicon is identified in the deposited metal as a result of thermal decomposition of  $\text{Al}_4\text{C}_3$ .

Subsequent mechanical testing of joints without heat treatment, and with T6 and combined (T6 + HIP) heat treatment yielded the following results. Three types of fracture were observed, namely along the interface between the base and the deposited metal, in the deposited layer and a combination of both types, the fracture type being independent of the kind of heat treatment. It was established, however, that T6 heat treatment greatly improves the joint strength, which after a combined treatment became 2 times higher than directly after spraying. So, if right after spraying it was equal to 60 to 100 MPa, after T6 heat treatment it was equal to 124–140, and after combined treatment to 140–180 MPa (Figure 5).

## CONCLUSION

As can be seen from the above review, in the field of DSCM fusion welding the main efforts are focused on elimination of the problems of SiC decomposition in the welding zone, porosity and sound formation of welds, using diverse techniques.

While at arc welding the joint strength close to that of wrought aluminium alloys can be achieved, and a slight formation of SiC is observed only in the weld upper part, in laser welding the main efforts are



aimed at suppression of the reaction of SiC decomposition by reducing the heat input into the welding zone, while the strength issues have practically not been given any attention.

Further studies should be aimed at providing equivalent strength of welded joints. Addition of reinforcing particles into the joint zone using inserts, foils, special fluxes and pastes can be used as a possible technique. It is also necessary to determine the influence of heat treatment on the strength of CM welded joints where heat-hardenable aluminium alloys are used as matrix.

Improvement of the technology of composite fabrication is just as important. For instance, such a defect as CM microporosity strongly influences the structure and properties of joints produced by arc welding. As a rule, porosity in such welds has inadmissible high values. Therefore, the possible defects of the initial materials such as pores, slag inclusions, particles agglomeration, etc. should be minimized.

- Vishnyakov, L.R., Oniskova, N.P., Romashko, I.M. et al. (1996) Technological development of composite materials of Al-SiC system. *Tekhnologiya Lyogk. Splavov*, **3**, 64-69.
- Chernyshova, T.A., Kobeleva, L.I., Shebo, P. et al. (1993) *Interaction of metal melts with reinforcing fillers*. Moscow: Nauka.
- Ahearn, J.S., Cooke, C., Fishman, S.G. (1982) Fusion welding of SiC-reinforced Al composites. *Metal Construction*, **40**, 192-197.
- Stauffer, H., Nowak, M. (1998) GTA and GMA welding of particle reinforced aluminium. In: *Proc. of 7th INALCO Int. Conf. on Joints in Aluminium at TWI*, Abington, Cambridge, Apr. 15-17, 1998.
- Klehn, R., Eagar, T.W. (1993) Joining of 6061 aluminium matrix-ceramic particle reinforced composites. *Weld. Res. Council, Bull.*, **385**, 26.
- (1989) Fusion welding of SiC reinforced aluminum. *Weld. Res. Council, Progr. Rep.*, **5/6**, 34.
- Dahotre, N.B., McCay, T.D., McCay, M.H. (1989) Laser processing of a SiC/Al alloy metal matrix composite. *J. Appl. Phys.*, **12**, 5072-5077.
- Chernyshova, T.A., Kobeleva, L.I., Panfilov, A.V. et al. (1997) Interphase structure and mechanical behavior of composite material based on aluminium reinforced with silicon carbide particles. *Perspektivn. Materialy*, **1**, 27-33.
- Aksyonov, A.A., Churmukov, E.A., Romanova, V.S. (1994) Influence of silicon on interaction processes on interfaces of Al-SiC composites. *Izv. Vuzov, Tsvetn. Metallurgiya*, **4**, 145-150.
- Lloyd, D.J. (1989) The solidification microstructure of particulate reinforced aluminium/silicon carbide composites. *Compos. Sci. Technol.*, **35**, 159.
- Lloyd, D.J., Lagace, H., McLeod, A. (1989) Microstructural aspects of aluminium-silicon carbide particulate composites produced by a casting method. *Mater. Sci. and Eng.*, **107**, 73.
- Ellis, M.V. (1996) Joining of Al-based metal matrix composites. *Mater. and Manufact. Proc.*, **1**, 45-66.
- Hill, J.F., Wilkinson, S.W., Fenn, R. (1997) Fusion welding of an aluminium matrix/SiC reinforced MMC. *Int. J. Joining of Materials*, **2**, 61-65.
- (1991) *Welding and welded materials*. Refer. Book. Ed. by E.L. Makarov. Moscow: Metallurgiya.
- Chernyshova, T.A., Bolotova, L.K., Kobeleva, L.I. et al. (1999) Arc welding of discretely reinforced composite material of Al-SiC system. *Fizika i Khimiya Obrab. Materialov*, **4**, 57-62.
- Das, K.B. *Method of welding metal matrix composites*. Pat. 743175 USA, Int. Cl. B 23 K 9/23, 219/137. Publ. 21.06.88.
- Ryabov, V.R., Muraveinik, A.N., Bondarev, A.A. (1999) Study of the structure of welded joints of a dispersion-strengthened aluminium alloy. *Tekhnologiya Lyogk. Splavov*, **1/2**, 139-144.
- Cola, M.J., Lienert, T.J., Gould, J.E. et al. (1990) Laser welding of a SiC particulate reinforced aluminium metal matrix composite. In: *Proc. of Mater. Weldab. Symp.*, Detroit. Ohio: Materials Park.
- Lienert, T.J., Fraser, H.L., Hooper, F.M. (1995) Laser and electron beam welding of SiC-reinforced 8009 aluminum. In: *Abstr. of pap. of 76th AWS Ann. Meeting*, Miami. Miami: AWS.
- Calliari, I., Dabala, M., Penasa, M. (2000) Pulsed Nd:YAG laser welding of MMC. *Adv. Eng. Mater.*, **2**, 653-656.
- Shiganov, I.N. (1998) Laser welding of non-ferrous and composite materials. *Tekhnologiya Metallov*, **3**, 18-22.
- Shiganov, I.N. (1997) Fusion welding of composite materials based on immiscible components. *Svarochn. Proizvodstvo*, **10**, 5-9.
- Lienert, T.J., Lippold, J.C., Brandon, E.D. (1993) Electron beam welding of SiC-reinforced aluminum A-356 metal matrix composite. In: *Abstr. of pap. of 1993 AWS Convent.* Houston: AWS.
- Ryabov, V.R., Ishchenko, A.Ya., Pap, P.A. et al. (1994) Manufacturing of Al-based composites reinforced with steel fibers by vacuum spraying. *Avtomatich. Svarka*, **9/10**, 40-44.
- Bondarev, A.A., Nazarenko, S.V., Bondarev, Andr.A. (1996) Investigation of the process and development of the technology of welding aluminium matrix composites reinforced with Al<sub>2</sub>O<sub>3</sub> and SiC particles. In: *Proc. of Int. Conf. on Improvement of Efficiency of Welding Manufacturing*, Lipetsk, 17-18 Oct., 1996. Lipetsk.
- Itsukaichi, T., Eagar, T.W., Umemoto, M. et al. (1996) Plasma spray joining of Al-matrix particulate reinforced composites. *Welding J.*, **9**, 285-296.
- Itsukaichi, T., Eagar, T.W., Umemoto, M. et al. (1992) Plasma spray joining of aluminium matrix composites using O-spray composite powder. *Quart. J. JWS*, **2**, 101-105.



# PECULIARITIES OF CARBON OXIDATION IN WELDING WITH ILMENITE-COVERED ELECTRODES

N.A. KALIN and N.G. EFIMENKO

Ukrainian Engineering-Pedagogical Academy, Kharkov, Ukraine

It was established that the process of decarburization of Fe-C alloy, for example, in the form of cast iron, in electrode coatings occurs mainly in the slag phase under the lower part of a growing droplet. Oxygen dissolved in metal and coming from the slag serves as oxidizer of carbon in the melt. It was found that losses of carbon for oxidation in the Fe-C alloy are 1.5 times higher than those of graphite, and the rate of decarburization at the droplet stage is twice as high.

**Key words:** carbon, Fe-C alloy, electrode coating, stage of droplet, decarburization, oxidation, carbon losses, microstructure, cast iron powder

The feasibility of use of Fe-C alloys, cast iron in particular, as a deoxidizer of the weld pool, partially replacing ferromanganese, was firstly described in work of N.G. Slayvanov [1]. However, this idea has not found its further development.

Some works [2-6] were devoted to the study of possibility of carbon use as a deoxidizer in welding electrodes during its adding into the coating in a free state or in to the composition of the electrode wire. It was established that carbon is oxidized in the droplet almost completely, and its content in the pool is not practically changed [3]. Results of the thermodynamic analysis of the redox processes with a carbon participation, proceeding in welding, show that carbon is more preferable as a deoxidizer in a bound state, for example, in the form of cast iron powder or high-carbon ferroalloys [7]. Nevertheless, the works of carbon application in the composition of Fe-C alloy as a deoxidizer in fusion welding were not found by us.

The present article is devoted to the study of peculiarities of oxidation of carbon used in the composition of Fe-C alloy as a deoxidizer in the electrode coatings of the ilmenite-type.

It is assumed that the process of decarburization of Fe-C alloy at the droplet stage is proceeding by the following scheme (Figure 1): during the process of electrode core 1 melting and electrode coating 2 heating up to temperature above 1450 °C, the small particles of cast iron 3 are melted in it. The carbon melt passing through the layer of molten slag 6 is accumulated in the form of a layer of carbon melt 5 under a growing droplet 4. This layer is an effective reducing agent. As a result the carbon content in the droplet will be determined by proceeding redox reactions between the arc gas phase 7 and liquid phases at the electrode end, i.e slag 6, carbon melt 5 and droplet metal 4. Carbon oxidizer in melt is oxygen dissolved in metal and coming from slag [8]:



To realize reaction (1) the oxygen should enter melt 5 from slag 6. Process of carbon oxidation in melt at the stage of the droplet is complex and multistage. It consists of a number of successive, simultaneous, parallel and mating stages. In the case considered the following stages are observed: diffusion of molecular oxygen to the surface of molten slag from the arc gas phase; adsorption-chemical interaction of oxygen with ions of bivalent iron of carbon melt and adjacent layer of slag  $0.5O_2 + 2Fe^{2+} + 3O^{2-} = 2FeO_2$ ; transfer of oxygen ions  $O^{2-}$  through the slag layer; mutual diffusion of ions  $Fe^{3+}$  and  $Fe^{2+}$  in slag; discharge of oxygen ions at the surface of liquid melt and dissolution of atomic oxygen ( $O^{2-} = [O] + 2e$ ;

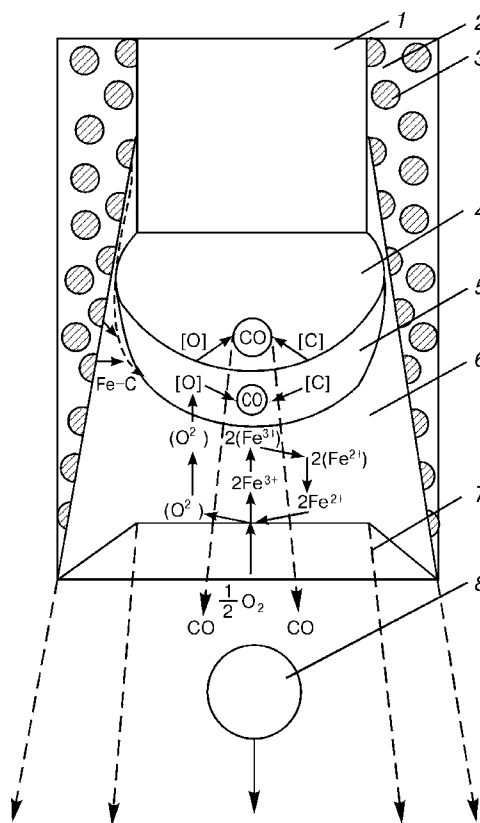


Figure 1. Scheme of process of decarburization of Fe-C alloy at the stage of droplet (for designations see the text)



Object for analysis	Mass fraction of carbon, %, in experiments							
	Initial	1st	2nd	3rd	4th	5th	6th	7th
Droplets of electrode metal	0.07	$\frac{0.08}{0.09}$	$\frac{0.08}{0.10}$	$\frac{0.08}{0.11}$	$\frac{0.08}{0.14}$	$\frac{0.09}{0.18}$	$\frac{0.14}{0.22}$	$\frac{0.18}{0.25}$
Deposited metal	0.06	$\frac{0.07}{0.08}$	$\frac{0.07}{0.09}$	$\frac{0.07}{0.10}$	$\frac{0.07}{0.13}$	$\frac{0.08}{0.17}$	$\frac{0.13}{0.21}$	$\frac{0.17}{0.24}$

Note. In numerator — carbon in Fe-C alloy; in denominator — carbon in the form of graphite.

recovery of ions of trivalent iron ( $\text{Fe}^{3+} + e = \text{Fe}^{2+}$ ); diffusion of oxygen and carbon in metal of carbon layer to the place of reaction; chemical reaction (1) in a carbon layer; formation and removal of CO bubbles.

Escaping CO bubbles passing through the carbon layer-droplet interface enter the metal of the latter. Moreover, in the process of bubbling the gas bubbles bring with themselves small volumes of carbon melt to the droplet, due to which it is saturated with a great number of CO bubbles and Fe-C alloy inclusions moving upward. In the bottom, more heated part of a growing droplet the reaction of additional oxidizing of carbon with CO precipitation into the arc zone, being not completed in carbon melt, is proceeding. Here, the residual content of carbon in the formed droplet 8 passing through the arc column 7 is tended to equilibrium content with a dissolved oxygen.

For investigations the electrodes of 4 mm diameter with ilmenite-type coating on wire Sv-08A (C — 0.1; Si — 0.03; Mn — 0.35–0.65 wt.%; Fe — balance) of two types were manufactured using a method of extrusion: with a cast iron powder and graphite in coating, and also initial electrodes — without C-containing components. Coatings with cast powder and graphite were manufactured for 7 variants of electrodes with equivalent content of carbon to mass of electrode core: 0.12; 0.16; 0.20; 0.24; 0.28; 0.32 and 0.36 %. The carbon content in cast iron was 3.5 %, coefficient of coating mass was 0.45–0.47. Welding was performed at DCRP ( $I_w = 160\text{--}180\text{ A}$ ).

A mass fraction of carbon was determined in droplets accumulated in cladding on massive copper plate using

a fast-moving electrode. Chemical analysis of deposited metal was made by sampling chips from metal deposited into a copper water-cooled mould [3].

To study the peculiarities of oxidation of carbon the macro- and microstructure of metal of ends of experimental electrodes with additions of 10 % cast iron, 1 % graphite to the coating and also without additions were analyzed.

The results of chemical analysis are given in the Table. The relative losses of carbon in oxidation at the stage of droplet were calculated by formula from [5]:

$$\psi_d = \frac{C_e - C_d}{C_e} [\%], \quad (2)$$

where  $C_e$ ,  $C_d$  are the carbon content in electrode and droplets, respectively.

Total carbon losses were determined by formula

$$\psi_{\text{tot}} = \frac{C_e - C_i}{C_e} [\%]. \quad (3)$$

Carbon losses for oxidation in pool were found as difference in carbon losses

$$\psi_p = \psi_{\text{tot}} - \psi_d [\%]. \quad (4)$$

Results of calculation of carbon losses in welding by formulae (2)–(4) are given in Figure 2. As is seen from the Figure, at a small mass fraction of carbon in electrode its losses for oxidation will be minimum [6]. With increase in carbon to critical content having different values for Fe-C alloy and graphite, losses at the stage of droplet and total losses are increased and at the stage of pool they are decreased. At further increase in mass fraction of carbon the losses for oxidation are decreased that is manifested in carburization of both metal of droplets and also deposited metal. This occurs due to the fact that the oxidizing potential of slag system of coating is exhausted. It should be noted that the reaction of carbon oxidizing in Fe-C alloy proceeds more completely than in graphite and its critical value in the coating can be higher. This is explained by that the molten cast iron in the form of carbon melt is better wetted with a slag than the hard carbon, as the CO bubbles forming in carbon oxidizing, are blocking the smaller part of its surface.

Oxides of iron, manganese, silicon and other elements contained in carbon melt are dissociated in metal with further oxygen diffusion inward the melt

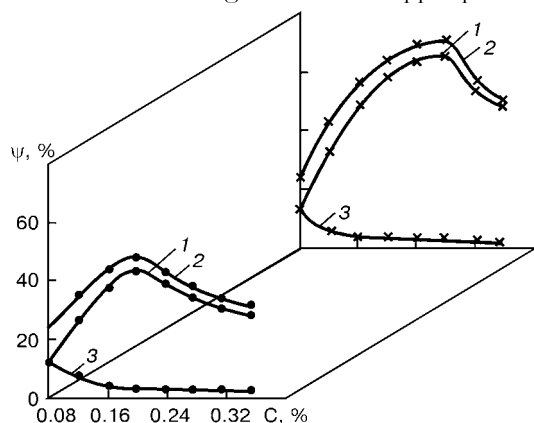
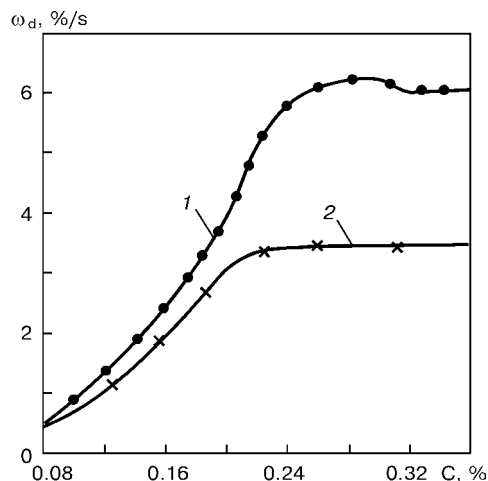
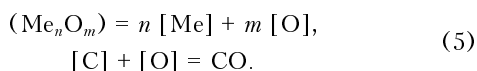


Figure 2. Dependence of carbon losses  $\psi$  for oxidation in welding on its content in electrodes: 1 — in droplet; 2 — total; 3 — in pool; ● — in graphite; X — in composition of Fe-C alloy



**Figure 3.** Dependence of rate of decarburization at the stage of droplet on carbon content in electrode: 1 — in composition of Fe-C alloy; 2 — in the form of graphite

and, after interacting with carbon, they become an additional source of oxidizer enter [9]:



As the mass transfer to the movable phase interface in contact of carbon melt with slag is proceeding more intensively than between carbon and slag, then the difference in rate of recovery with carbon in the diffusion condition can reach one order [9].

It is known [5] that the rate of carbon oxidation at the stage of droplet at a constant flow of oxygen is determined by equation

$$\omega_d = \frac{\Psi_d C_c}{t} [\%/s], \quad (6)$$

where  $t$  is the time of interaction in droplet during welding.

Assuming  $t = 0.03$  s [5], we shall obtain

$$\omega_d = \frac{\Psi_d C_c}{0.03} [\%/s]. \quad (7)$$

Figure 3 gives the curves of rates of decarburization at the stage of droplet, obtained for experimental compositions of electrodes by formula (7). It is seen from Figure, that maximum rate of carbon oxidation at the stage of droplet, added to composition of Fe-C alloy, reaches  $\approx 6.33$  %/s. With increase in carbon content above critical for the mentioned slag system the rate of oxidation is decreased negligibly and remains almost at the same level. Maximum rate of oxidation of carbon in the form of graphite is 2 times lower and amounts to about 3.33 %/s at reaching its critical content.

Decrease and stabilizing of rate of carbon oxidation in droplets with rise of its content in the electrodes is also explained by the fact that the oxidizing potential of the slag system is exhausted.

The melting of electrodes containing the cast iron powder in coating (Figure 4, *a*) is characterized by the formation of easily-melting slag layer of 0.1 mm

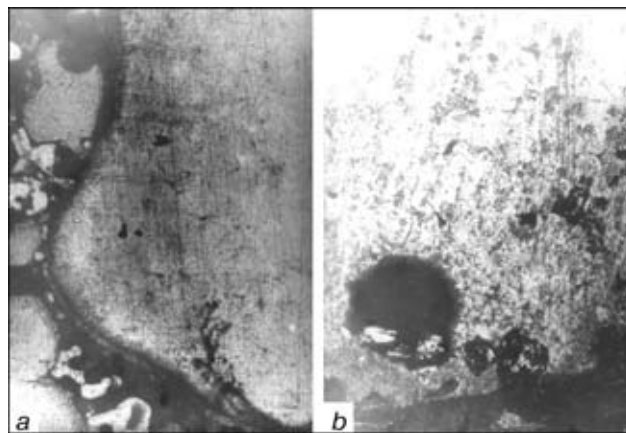


**Figure 4.** Microstructure of metal of electrode ends with coating containing cast iron powder: *a* —  $\times 120$ ; *b* —  $\times 500$

thickness projecting along electrode core for 1.3–1.5 mm height above the line of interface of liquid and solid phase of the core. At the electrode end the formation of layer of carbon melt and clustering of gas bubbles and slag inclusions are observed proving an intensive process of metal boiling in the lower part of the droplet. The decarburized melt transfers partially into the droplet metal in the form of small inclusions of about 0.05 mm size (Figure 4, *b*).

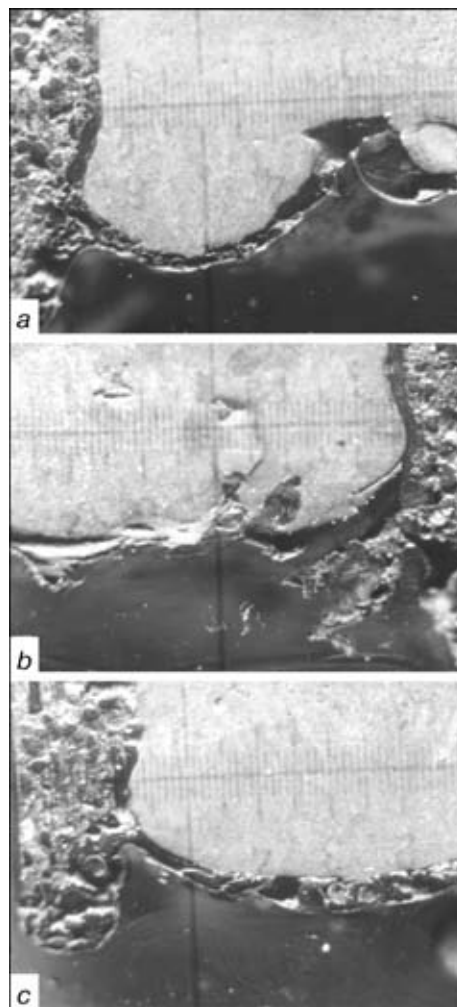


**Figure 5.** Macrostructure of metal of electrode ends with coating containing cast iron powder (*a*), graphite (*b*) and with a coating without deoxidizer (*c*) ( $\times 27$ )



Fine particles of carbon melt during lifting into the upper part of the droplet are decreased to 0.03–0.01 mm and at the height of  $\approx 0.5$ –0.6 mm the forming droplets are dissolved completely. Moreover, they are surrounded by CO gas bubbles. Gas CO is accumulated in the lower, more heated part of droplet and reaching critical pressure it is exploded into the arc zone. In addition, a typical depression is formed at the droplet surface (Figure 5, *a*).

In electrodes with graphite in the coating and intensive boiling of metal in the entire volume of droplet is occurred due to presence of hard inclusions of unsolved graphite in it (Figure 5, *b*). Reaction of oxidation of hard graphite at this stage is not finished completely. Remnants of a hard fraction of graphite are transferred into the pool and carburize the weld metal. Coating of electrodes of the initial variant (Figure 5, *c*) is melted without boiling of the droplet metal.

It can be concluded on the basis of investigations that graphite, having a high (3723 K) temperature of melting, comes into reaction of oxidation with gas, slag and metal phases of the arc in a solid state. Here, the rate of the graphite oxidation in the ilmenite-type coating is 2 times lower than that of carbon in Fe–C alloy that leads to the necessary decrease in its critical content in the electrode. Therefore, it is impossible to use graphite fully as a deoxidizer in welding electrodes of the given types.

The oxidation of carbon added to the composition of Fe–C alloy has a number of peculiar features. It is dissolved in melting powder in its metallic base and comes into reaction of decarburization with gas, slag and metal phases at the stage of droplet. After partial oxidation in the slag the molten Fe–C alloy is trans-

ferred into the droplet metal in the form of fine inclusions where it is decarburized.

Thus, when the cast iron powder is used in the amount exceeding the critical content of carbon for the given slag system there will be no hazard of the deposited metal carburization.

## CONCLUSIONS

1. Mechanism was studied and scheme of the process of carbon oxidation from Fe–C alloy included into the composition of electrode coating was suggested.

2. Losses of carbon from Fe–C alloy and graphite in electrode coating of ilmenite-type in welding were determined. It was established that carbon losses for oxidation of Fe–C alloy are higher than those of graphite by almost 1.5 times.

3. It was established that rate of decarburization at the droplet stage in Fe–C alloy is 2 times higher than that of graphite.

1. Slavyanov, N.G. (1988) *Transactions and inventions*. Perm.
2. Alov, A.A. (1947) *Electrodes for arc welding and surfacing*. Moscow: Mashgiz.
3. Erokhin, A.A. (1964) *Kinetics of metallurgical processes of arc welding*. Moscow: Mashinostroenie.
4. Mazel, A.G. (1969) *Technological properties of electric welding arc*. Moscow: Mashinostroenie.
5. Erokhin, A.A. (1973) *Fundamentals of fusion welding*. Moscow: Mashinostroenie.
6. Bykov, A.N. (1968) Oxidation of carbon in welding with high-alloy carbonate-fluorite coated electrodes. *Svarochn. Proizvodstvo*, **12**, 6–8.
7. Efimenko, N.G., Kalin, N.A. (2000) Thermodynamic analysis of redox carbon-involving processes occurred during fusion welding. *The Paton Welding J.*, **7**, 17–20.
8. Medzhibozhsky, M.Ya. (1986) *Fundamentals of thermodynamics and kinetics of steelmaking processes*. Kyiv-Donetsk: Vyshcha Shkola.
9. Popal, S.I., Sotnikov, A.I., Boronenkov, V.N. (1986) *Theory of metallurgical processes*. Moscow: Metallurgiya.



# EFFECT OF DEFORMATION ON ELECTROCHEMICAL HETEROGENEITY OF PIPELINE WELDED JOINTS

A.I. RADKEVICH

G.V. Karpenko Physico-Mechanical Institute, NASU, Lviv, Ukraine

Electrode potentials have been measured in various zones of a circumferential welded joint on low-carbon steel pipes at different levels of loading using internal pressure. It is shown that plastic deformation eliminates completely the difference of potentials between the parent metal and HAZ of the welded joint.

**Key words:** welded joints, pipelines, internal pressure, deformation, electrochemical heterogeneity

Electrochemical heterogeneity of welded joints (WJ) can cause significant corrosion and corrosion-mechanical damages [1]. It occurs due to difference in the chemical composition and structure of various regions of the welded joint, and also residual stresses in them which especially reduce their resistance to corrosion and stress-corrosion cracking [1–6]. To decrease it, the different methods, in particular such as heat treatment of WJ, selection of welding consumables, welding conditions, etc. are used. It is known that redistribution of residual stresses occurs during plastic deformation of WJ [6] and also in circumferential WJ of pipelines at their loading with internal pressure [7, 8]. Linear part of oil and gas pipelines is obligatory tested using an increased pressure before their putting into service to evaluate the leak-tightness and strength, revealing of possible latent defects which were not eliminated in construction [9, 10]. Therefore, it is evident that the use of hydraulic tests of WJ and decrease their electrochemical heterogeneity is actual problem for the favourable redistribution of residual stresses in WJ. The present work aim is to evaluate the effect of internal pressure in the pipeline and its deformation on electrochemical heterogeneity of circumferential WJ.

To evaluate the electrochemical heterogeneity of WJ, the local electrode potentials were measured by a voltmeter of potentiostat P-5827 which has a high input resistance and can be used for determination of DC voltage in low-powerful power sources. Electrode potentials in microzones of metal can be determined by a microelectrode with a capillary, whose inner diameter was commensurable with a region examined. Otherwise, the capillary will overlap the separate zones that will make it impossible to measure the difference of potentials between them [11, 12]. The capillary was manufactured from a glass tube of about 1 mm diameter, whose end was elongated to diameter 30–50  $\mu\text{m}$ . Then capillary 1 (Figure 1, *a*) was pressed-in into a fluoroplastic transition bushing 2 which, after its filling with a working solution, was placed tightly on a cylindrical end of a chlorosilver electrode 3 that provided the capillary filling with this solution.

In investigations of microelectrochemical heterogeneity of metal the essential role was played by an electrolyte which should have a low electrical conductivity [11, 12]. In case of the electrolyte with a high electroconductivity the mutual polarization of anodic and cathodic regions occurs, leading to establishment of an integral potential for both regions. If the resistance of the electrolyte is high then the system is not polarized and potentials of separate regions can be measured. Electrolyte was selected experimentally. The best working solution was a distilled water. The possible jump of the diffusion potential for interface «KCl–distilled water» from minimum concentrations of KCl to the saturation from data [13] was only 0.4–1.8 mV. To prevent the effect of a possible jump of the diffusion potential on the results of investigations, the measurements of electrode potentials started after preliminary soaking (> 2 h) of WJ in a working medium until stabilizing the electrode potential which began approximately after one hour.

Local electrode potentials were measured along the upper generatrix of pipe 1 (Figure 1, *b*) with a

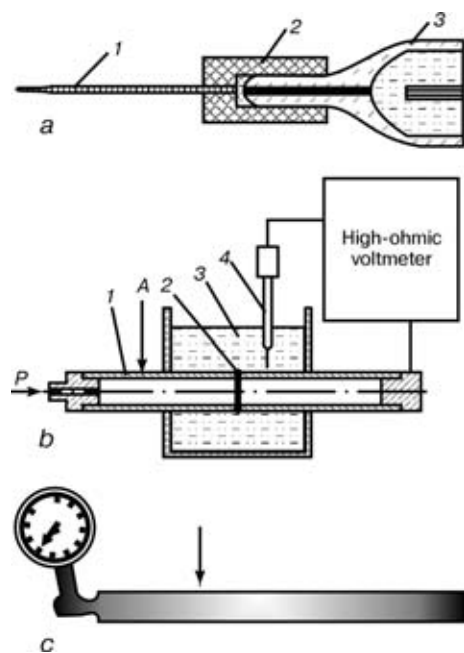


**Figure 1.** Microelectrode (*a*), scheme of measurement of local electrode potentials of WJ of pipe (*b*) and detection of longitudinal crack (shown by arrow) in St.20 pipe after fracture by internal pressure (*c*) (see designations in text)

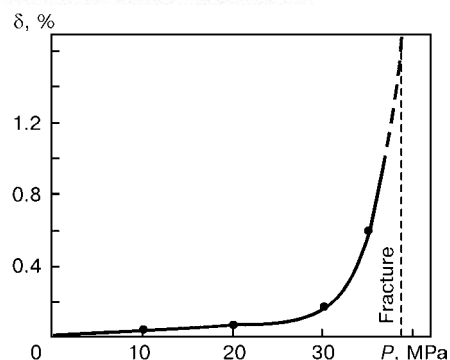


**Figure 2.** Dependence of St.20 pipe parent metal deformation on internal pressure (dash line — intensive yielding of pipe metal with formation of buckling and crack)

circumferential weld 2 in the middle. The pipe was fixed in a cell 3 with a working solution. Microelectrode 4 was mounted over different zones of pipe WJ. Experiments were performed at different stresses in pipe wall, which were attained by different pressure  $P$  in its inner cavity using press MP-600. During experiments the changes in outside diameter of pipe in point A (at about 200 mm distance from weld) beyond the cell 3 were recorded and the deformation  $\delta$  of pipe metal at the external surface depending on internal pressure was calculated on the basis of changes.

Seamless steel 20 (C — 0.2 wt.%) pipe of 60×6 mm diameter was selected for investigations. To reduce the collapsing pressure which can be reached by press MP-600 ( $\approx 58.8$  MPa), the pipe wall thickness was decreased to diameter 54 mm at the distance 275 mm (total length of each pipe is about 400 mm) using lathe machining. Then, two pipes were welded by a circumferential weld. Root weld was made by argon-arc welding with Sv-08GA (C — < 0.1; Mn — 0.8–1.0 wt.%; Fe — balance) wire and filling weld was made by electrodes Fox EV50. In thick (non-machined) ends of welded pipes the threaded plugs with a manometer (Figure 1, c) and pipeline for press MP-600 were installed. Oxide films and scale which were formed at the pipe surface after welding were subjected to etching.

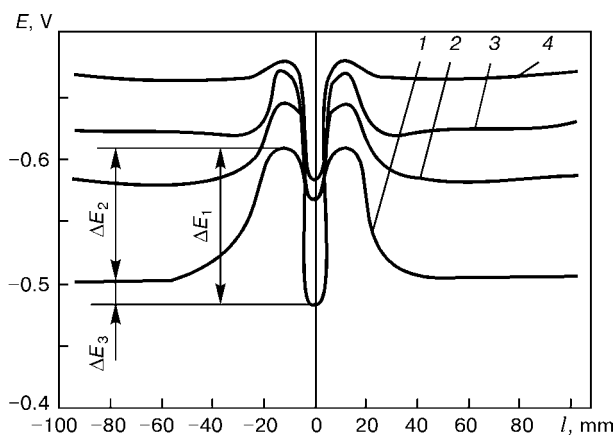


**Figure 3.** Curves of distribution of local electrode potentials in different zones of welded joint of St.20 pipe at different internal pressures: 1 —  $P = 0$ ; 2 —  $P = 20$ ; 3 —  $P = 30$ ; 4 —  $P = 35$  MPa

The tests were performed in the following sequence. Cell 3 with a welded pipe 1, installed into it (see Figure 1, b) was filled with a working medium, soaked for 2 h to stabilize the potential and then the local electrode potentials were measured in different regions of WJ of pipe by microelectrode moving along its generatrix. Further, the internal pressure was created inside the pipe, changes in pipe diameter were recorded and the measurements of local electrode potentials were repeated. Using this method the electrode potentials at different internal pressure, which was increased up to the collapsing value, were determined.

It was established that with increase in pressure to up to 24.5–26.5 MPa the pipe deformation was proportionally increased to  $\delta \leq 0.12$  % (Figure 2). At high its values ( $P = 30$ –35 MPa) the plastic deformation of the pipe occurred, and at  $P > 36.5$  MPa the abrupt increase in deformation (see dash line in Figure 2) and pipe fracture in parent metal with the formation of buckling and cracks of about 60 mm length along the generatrix are occurred (see Figure 1, c).

Local electrode potentials were measured at the following values of internal pressure: 0, 20, 30 and 35 MPa which correspond to the following deformations  $\delta$  of the pipe parent metal: 0, 0.11, 0.165 and 0.65 %. It was established that the electrode potential of initial ( $P = 0$ ) WJ becomes more negative in transition from weld to HAZ, then it is gradually improved in transition to the parent metal and stabilized at the distance of about 55–60 mm (Figure 3, curve 1). Difference of potentials  $\Delta E_1$  between the weld and HAZ metals is highest, being somewhat lower between the parent and HAZ metals ( $\Delta E_2$ ). The difference of potentials is also observed between weld and parent metal ( $\Delta E_3$ ). With increase in internal pressure the electrode potentials of all zones of WJ are shifted to the region of more negative potentials (Figure 3, curves 2–4), that is correlated completely with data [1, 4–6].

Nature of curves of changing electrode potentials is similar to relationships of distribution of residual stresses in circumferential WJ of steel pipes [7, 8]. Difference between them consists in the fact that the residual stresses in HAZ metal are abruptly changed from tensile to compressive. The electrode potentials of steel are shifted to the region of more negative potentials due to action of stresses, both compressive and tensile [4]. Therefore, curves  $\Delta E - l$  (Figure 3) reflect changes in value of residual stresses without allowance for their sign (compressive or tensile).

With increase in internal pressure to 20 MPa  $\Delta E_1$  is first decreased by 45–40 mV, and then increased by 16–22 mV (Figure 4, curve 1) that is, evidently, caused by different degree of deformation of weld and parent metal due to difference in their strength, and also effect of thickness. The weld reinforcement was 1.5–2.0 mm, it was not removed, as this could influence the residual stresses. The tensile and yield strengths of St.20 ( $\sigma_t \approx 350$  MPa,  $\sigma_{0.2} \approx 175$  MPa)



were significantly lower as compared with those of welds made by electrodes Fox EV50 ( $\sigma_t \approx 540$  MPa,  $\sigma_{0.2} \approx 445$  MPa). Thus, at pressures 30–35 MPa the plastic deformation of the pipe parent metal occurred (see Figure 2) that caused the shifting of electrode potentials to the region of more negative potentials (see Figure 3), while the weld metal was not yet subjected to plastic deformation and its electrode potential was changed negligibly. Therefore, at  $P = 30$ – $35$  MPa  $\Delta E_1$  increases (Figure 4, curve 1).

The electrode potentials of weld are less negative than those of parent metal (see Figure 3). In pipe deformation within elasticity range (up to 20 MPa) the difference of potentials between them  $\Delta E_3$  is decreased (Figure 4, curve 3). However, the further increase in the inner pressure increases  $\Delta E_3$  due to different stresses and nature (elastic or plastic) of deformation in weld and parent metal.

The positive effect of deformation of WJ of pipe on decrease in difference of potentials  $\Delta E_2$  between parent metal and HAZ is observed at all the values of internal pressure (Figure 4, curve 2). However,  $\Delta E_2$  is most intensively decreased under the action of plastic deformation of pipe metal approximately at  $P \geq 30$  MPa and amounts only to about 15 mV at  $P = 35$  MPa, whereas in initial WJ ( $P = 0$ )  $\Delta E_2$  is about 105 mV.

Thus, the testing pipelines using increased pressure decreases the electrochemical heterogeneity of circumferential WJ of pipes. The most effective improvement of corrosion resistance of WJ occurs at pressures which cause the plastic deformation of pipes. At pressure close to collapsing the almost complete leveling of values of electrode potentials of parent metal and HAZ metal occurs (see Figure 2) that is not attained even by postweld heat treatment according to [6]. Consequently, the testing using increased pressure is rational to use for increasing degree of defect detection in pipe WJ. However, to use it as a method of increasing performance of pipelines in aggressive, in particular hydrosulphuric media is dangerous as the significant decrease of electrochemical heterogeneity of WJ is possible at pressures causing plastic deformation of metal of pipelines due to which the growth of available defects in WJ is possible [10].

Thus, the electrochemical examinations showed that with increase in internal pressure in welded carbon steel pipe the electrochemical heterogeneity of WJ

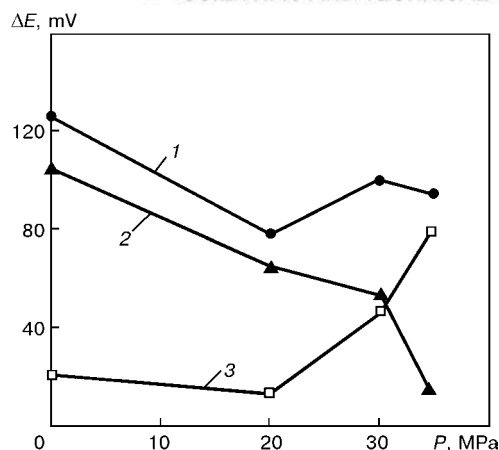


Figure 4. Effect of internal pressure on change in difference of potentials in St.20 pipe WJ: 1 — between welds and HAZ ( $\Delta E_1$ ); 2 — HAZ and parent metal ( $\Delta E_2$ ); 3 — parent metal and weld ( $\Delta E_3$ )

is decreased. However, the testing of pipelines with increased pressure in practice is limited.

1. Karpenko, G.V., Vasilenko, I.I. (1971) *Corrosion cracking of steels*. Kyiv: Tekhnika.
2. Vasilenko, I.I., Melekhov, R.K. (1977) *Corrosion cracking of steels*. Kyiv: Naukova Dumka.
3. Polyakov, S.G., Goncharov, A.B., Onoprienko, L.M. et al. (1992) Influence of electrochemical heterogeneity of titanium-zirconium welded joint on its corrosion resistance. *Zashchita Metallov*, **6**, 898–903.
4. Azhugin, F.F. (1974) *Stress-corrosion cracking and protection of high-strength steels*. Moscow: Metallurgiya.
5. Gutman, E.M. (1974) *Mechanochemistry of metals and corrosion protection*. Moscow: Metallurgiya.
6. Steklov, O.I. (1990) *Resistance of materials and structures to stress corrosion*. Moscow: Mashinostroenie.
7. Makhnenko, V.I. (1976) *Computational methods of study of kinetics of welding stresses and strains*. Kyiv: Naukova Dumka.
8. Makhnenko, V.I., Makhnenko, O.V. (2000) Development of calculation procedures for assessment of allowable defects in welded joints of critical structures. *The Paton Welding J.*, **9/10**, 79–87.
9. Ivantsov, O.M. (1985) *Reliability of main pipelines*. Moscow: Nedra.
10. Gessler, X. (1987) Hydrotest of pipeline layed by method of pressure loading above yield stress. In: *Proc. of 9th Soviet-German Symp. on Problems of Manufacturing of Large-Diameter Tubes*. Moscow.
11. Karpenko, G.V., Zamostyanik, I.E., Babey, Yu.I. et al. (1969) Determination of stresses in microvolumes of metal with aid of electrode potential. *Fiziko-Khim. Mekhanika Materialov*, **5**, 535–536.
12. Karpenko, G.V., Zamostyanik, I.E., Gutman, E.M. et al. (1970) Microelectrochemical heterogeneity of low-carbon steel with non-metallic inclusions. *Ibid.*, **1**, 3–6.
13. Rabinovich, V.A. (1985) *Thermodynamic activity of ions in electrolyte solutions*. Leningrad: Khimiya.



# ALLOWANCE FOR EFFECT OF CYCLE ASYMMETRY ON FATIGUE RESISTANCE OF WELDED JOINTS

V.S. KOVALCHUK

The E.O. Paton Electric Welding Institute, NASU, Kyiv, Ukraine

The paper deals with an engineering method of calculating estimation of the influence of cycle asymmetry on fatigue resistance of steel welded joints at different values of base in the high-cycle region of fatigue life. An informative diagram of limiting ranges of stresses based on asymmetry parameters and number of cycles, as well as analytical expressions for its description are suggested.

**Key words:** welded joints, fatigue resistance, cycle asymmetry, diagram, calculations

Many machine parts and metal structure elements are subjected during service to simultaneous action of cyclic and static loads. As a result of their summing the alternating stresses with a definite asymmetry of cycle  $r$  are occurred. In welded joints the cycle asymmetry in the zone of weld can change additionally by residual welding stresses. At a combined action of alternating and constant loads the deformation (vibrocreep) and, respectively, deformational strengthening of metal that causes complex non-linear mutual effect of strengthening and damaging effects are increased [1]. Undoubtedly, coefficient  $r$  should be taken into account in fatigue calculations in designing new and also in evaluation of residual life of metal structures being in service for a long time under alternating loading or those which exhausted their service term.

However, in some foreign standards of design and rules of designing [2, 3] the stress range is considered as a dominating factor in determination of fatigue resistance of road and building metal structures. In addition, the admissible value of range is the function of stresses which depends on the shape of welded joint and design fatigue life, while the cycle asymmetry is not almost taken into account. In national SNiP [4] the effect of cycle asymmetry is taken into account

in determination of maximum stresses using a correction coefficient, but without allowance for base of a cyclic life.

Usually the dependence of fatigue resistance on  $r$  is presented by diagrams of limiting stresses  $\sigma_{\min}$ ,  $\sigma_{\max} - \sigma_m$  or  $\sigma_{\max} - \sigma_{\min}$ , plotted by known values of fatigue limits at selected numbers of cycles [5, 6]. However, to obtain experimental data within the entire interval of cycle asymmetry it is necessary to fulfill a large number of fatigue tests. Therefore, these diagrams are plotted as a rule for one or several bases of fatigue life using a limited number of  $r$ . Assuming that fatigue limits depend linearly on cycle asymmetry [7] an additional grid of rays corresponding to different  $r$  is put on diagrams. This approach was valid for plotting diagrams relative to fatigue limits of welded joints of steel [5] where the effect of cycle asymmetry is negligible. The similar diagram plotting at other values of fatigue strength bases can lead to errors in determination of fatigue resistance. Similar results can be obtained from the assumption that fatigue resistance is changed proportionally at all the bases (similarity of fatigue curves at symmetrical and asymmetric loading) [18]. This is stipulated by possible change in inclination of fatigue curves at change in the cycle asymmetry. In addition, the inclination of fatigue curves depends on the parameter of stresses. Figure 1, *a* presents fatigue curves of steel M16S

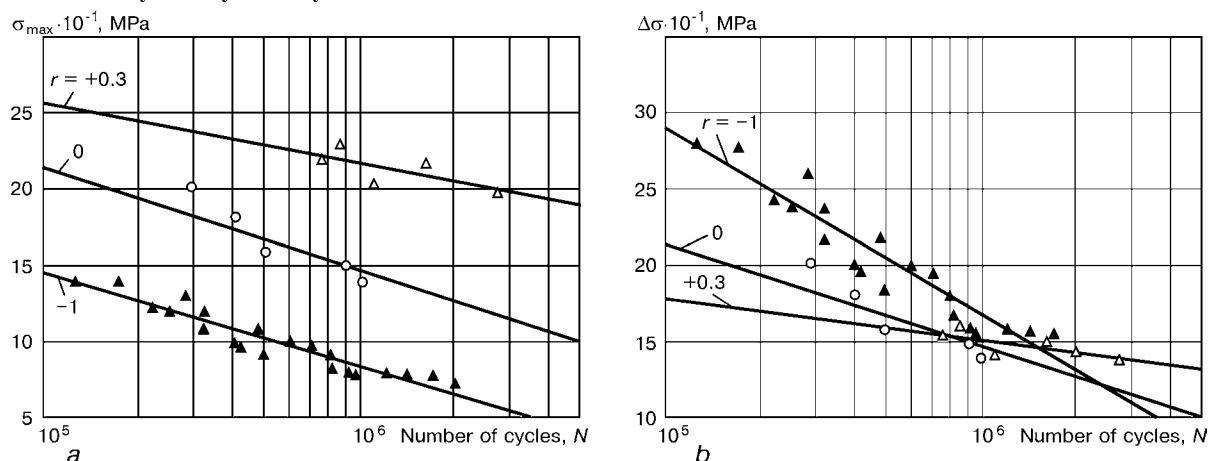


Figure 1. Fatigue curves of large-sized steel M16S specimens with butt joints plotted by maximum stresses (*a*) and ranges of stresses (*b*)

specimens with butt welded joints (coordinates  $\sigma_{\max} - \lg N$ ) [5] and replotted curves in coordinates of stress ranges  $\Delta\sigma - \lg N$  (Figure 1, *b*). In the first case the fatigue curves obtained at different asymmetry are almost parallel, in the second case they have a form of a fan with intersection approximately at the level of fatigue limit.

Analysis of results of numerous experimental data obtained at the E.O. Paton Electric Welding Institute on the large-scale specimens with various types of welded joints, manufactured from structural steels of different grades and classes of strength, showed that the dependencies  $\Delta\sigma - \lg N$  at different asymmetry are similar in most cases to those shown in Figure 1, *b*. In this connection it seems rational to plot the diagram of limiting ranges of stresses by parameters  $N$  and  $r$ . This type of diagram plotted from data of Figure 1 for some discrete values of fatigue strength bases is presented in Figure 2. Relationship  $\Delta\sigma - r$  at different bases of fatigue strength is described more precisely by more complex curve (equation of second order), however, it can be presented with a sufficient precision for practical purposes in the form of a straight line. Taking into account that scale  $\lg N$  is linear, grid of rays corresponding to selected bases of fatigue strength can be plotted with a desirable pitch.

As is seen from the diagram, the limiting range of stresses  $\Delta\sigma$  of welded joints depends greatly on asymmetry of cycle  $r$  and base of loading  $N$ . In the linear system of coordinates  $r - \Delta\sigma$  the link of these parameters at fixed bases of cyclic fatigue life  $N$  can be approximated by a beam of straight lines (rays) intersecting in a common point (pole)  $P_1$ .

Analytic expression of straight lines passing through point  $P_1(r_1, \Delta\sigma_1)$  in a given direction can be presented in the form

$$\Delta\sigma = k(r_1 - r) + \Delta\sigma_1. \quad (1)$$

At preset base of cyclic fatigue life  $N$ , fixed values of coefficient of cycle asymmetry  $r$  and appropriate values of limiting range of stresses  $\Delta\sigma$  the coefficient of proportionality

$$k = (\Delta\sigma - \Delta\sigma_1)/(r_1 - r) \quad (2)$$

has dimensionality of stresses and equals numerically to tangent of angle of inclination of straight line to abscissa axis ( $k = \operatorname{tg} \alpha$ ) in coordinates  $\Delta\sigma - r$ .

As the rays plotted in the diagram are isolines of a base number of cyclic fatigue life and left (inclined) branch of fatigue curves in the coordinate system with a logarithmic scale of number of loading cycles represents a straight line, then there is a direct relation between limiting range of stresses  $\Delta\sigma$  and  $\lg N$ :

$$k = f(N) = \gamma \lg N + d, \quad (3)$$

where  $\gamma = \operatorname{tg} \beta$  ( $\beta$  — angle of inclination of straight line to abscissa axis in coordinates  $k - \lg N$ );  $d$  is the constant.

Taking into account the relationship (3) the equation (1) takes the form

$$\Delta\sigma = (\gamma \lg N + d)(r_1 - r) + \Delta\sigma_1. \quad (4)$$

Solution of equation (4) relative to  $\lg N$  allows us to obtain expression for determination of logarithm of fatigue life in the form

$$\lg N = \left( \frac{\Delta\sigma - \Delta\sigma_1}{r_1 - r} - d \right) / \gamma \quad (5)$$

and cyclic fatigue life

$$N = 10^{\left( \frac{\Delta\sigma - \Delta\sigma_1}{r_1 - r} - d \right) / \gamma}. \quad (6)$$

To plot the full diagram or to determine the limiting range of stresses and cyclic fatigue life using expressions (4)–(6) within all the interval of cycle asymmetry and test base it is necessary to know the minimum of initial parameters determined experimentally. Let us illustrate this on example.

For butt welded joints made from steel M16S (see Figure 1) point  $P_1(r_1, \Delta\sigma_1)$  has coordinates (0.8, 136.6). Equation of rays in this case has a form

$$\Delta\sigma = k(0.8 - r) + 136.6. \quad (7)$$

As was noted the angle of inclination of rays and, respectively, the value of coefficient  $k$  depend on the selected base of cyclic fatigue life. For fixed values of these base the value  $k$  can be found from expression (2). From experimental data (Figure 2), for example, at bases of fatigue life  $N = 1 \cdot 10^5$  and  $1 \cdot 10^6$  cycles this coefficient is equal to 82.5 and 15.9, respectively.

Substituting values of coefficient  $k$  and  $\lg N$ , corresponding to it, in the equation (3) we shall obtain the system of equations:

$$82.5 = 5\gamma + d,$$

$$15.9 = 6\gamma + d.$$

Taking into consideration that  $\gamma = \operatorname{tg} \beta$  we shall obtain  $\gamma = -66.6$  (Figure 3). Substituting the obtained

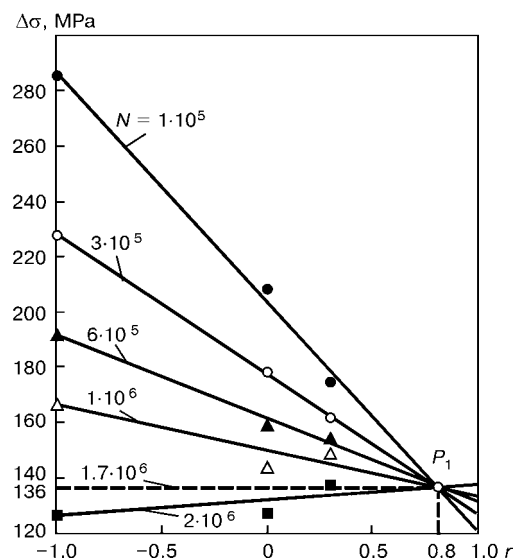


Figure 2. Diagram of limiting ranges of stresses  $\Delta\sigma$  of butt welded joints made from steel M16S

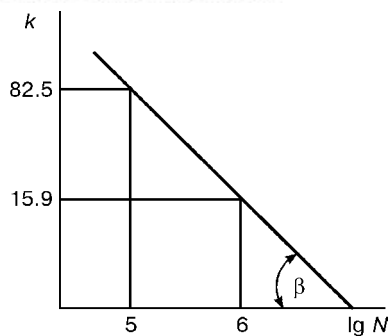


Figure 3. Dependence of coefficient  $k$  on  $\lg N$

value  $\gamma$  into one of equations of the system we shall find  $d = 415.5$ .

Taking into account (3) and (7) the equation of limiting range of stresses of butt joints of steel M16S will take the final form

$$\Delta\sigma = (415.5 - 66 \lg N)(0.8 - r) + 136.6.$$

Hence,

$$\lg N = \left( \frac{\Delta\sigma - 136.6}{0.8 - r} - 415.5 \right) / (-66.6),$$

$$N = 10^{\left( \frac{\Delta\sigma - 136.6}{0.8 - r} - 415.5 / (-66.6) \right)}.$$

For quantitative evaluation of the effect of cycle asymmetry on the change in limiting range of stresses it is necessary to compare values  $\Delta\sigma$  on a fixed base of cyclic fatigue life at different values of cycle asymmetry: at calculated  $r_c$  and standard  $r_s$ .

In accordance with (1) the equations for the calculated and standard values of limiting range of stresses can be written in the form

$$\Delta\sigma_c = k(r_1 - r_c) + \Delta\sigma_1, \quad (8)$$

$$\Delta\sigma_s = k(r_1 - r_s) + \Delta\sigma_1. \quad (9)$$

It is rational to compare not the limiting ranges of stresses themselves, but their increments above point  $\Delta\sigma_1$ , equal or close to the fatigue limit:

$$\Delta\sigma_c - \Delta\sigma_1 = k(r_1 - r_c),$$

$$\Delta\sigma_s - \Delta\sigma_1 = k(r_1 - r_s).$$

Their relation is

$$\Delta\sigma_c - \Delta\sigma_1 / \Delta\sigma_s - \Delta\sigma_1 = (r_1 - r_c) / (r_1 - r_s). \quad (10)$$

In practice  $r_s = 0$  is taken usually as a standard value. It is interesting to compare the increment of limiting range of stresses at frequently used values of cycle asymmetry  $r_c = -1$  and  $r_c = +0.5$  with  $r_s = 0$ .

For joints made from steel M16S at  $r_s = 0$  and  $r_c = -1$  we shall obtain

$$\Delta\sigma_c - 136.6 / \Delta\sigma_s - 136.6 = (0.8 + 1) / 0.8 = 2.25.$$

As is seen from this expression the increment of limiting ranges of stresses at a symmetrical loading

exceeds more than twice the standard value that is naturally put into fatigue life margin.

At  $r_s = 0$  and  $r_c = +0.5$

$$\Delta\sigma_c - 136.6 / \Delta\sigma_s - 136.6 = (0.8 - 0.5) / 0.8 = 0.375.$$

In this case the increment of limiting ranges of stresses is lower than at zero cycle of loading by 2.7 times. It is evident, that in the area of sign-constant variable tension the fatigue life is failed at such approach.

For quantitative evaluation of changing cyclic fatigue life it is necessary to compare values  $N$  at fixed (similar) value of range of stresses, but at various asymmetry of cycle, i.e.  $r_c$  and  $r_s$ .

According to (6), the number of cycles at calculated and standard asymmetry can be written in the form

$$N_c = 10^{\left( \frac{\Delta\sigma - \Delta\sigma_1}{r_1 - r_p} - d \right) / \gamma},$$

$$N_s = 10^{\left( \frac{\Delta\sigma - \Delta\sigma_1}{r_1 - r_s} - d \right) / \gamma}.$$

The relation of fatigue lives is

$$N_s / N_c = 10^{\left( \frac{\Delta\sigma - \Delta\sigma_1}{r_1 - r_s} - \frac{\Delta\sigma - \Delta\sigma_1}{r_1 - r_c} \right) / \gamma}$$

or

$$N_c / N_s = 10^{\frac{(\Delta\sigma - \Delta\sigma_1)(r_c - r_s)}{\gamma(r_1 - r_c)(r_1 - r_s)}}.$$

With respect to joints of steel M16S at  $r_s = 0$  and  $r_c = -1$  we shall obtain

$$N_{-1} / N_0 = 10^{\frac{(\Delta\sigma - 136.6)(-1)}{-66.6(0.8 + 1)0.8}} = 10^{\frac{(\Delta\sigma - 136.6)}{95.9}}.$$

The relation of fatigue lives depends on the level of loading and increases with its rise. At limiting range of stresses  $\Delta\sigma = 200$  MPa this relation is

$$N_{-1} / N_0 = 10^{\frac{(200 - 136.6)}{95.9}} = 4.58.$$

In this case the fatigue life margin is 4.58.

At  $r_s = 0$ ,  $r_c = +0.5$  and  $\Delta\sigma = 160$  MPa

$$N_{0.5} / N_0 = 10^{\frac{(\Delta\sigma - 136.6)(0.5)}{-66.6(0.8 - 0.5)0.8}},$$

$$N_{0.5} / N_0 = 10^{\frac{(160 - 136.6)(0.5)}{-66.6(0.8 - 0.5)0.8}} = 10^{-0.732} = 1/5.39.$$

It is evident that it is not necessary to neglect the reduction of cyclic fatigue life of welded joints in the region of sign-constant tension by more than 5 times.

## CONCLUSIONS

1. Determination of cyclic fatigue life by limiting ranges of stresses corresponding to zero cycles without allowance for the effect of cycle symmetry in the region of limiting fatigue life can lead to error up to



$\pm 5$  times. Error depends on the level of loading and increases with its rise. The effect of cycle asymmetry on fatigue limit is negligible and in some cases it can be neglected.

2. The offered type of diagram of limiting ranges of stresses  $\Delta\sigma$  using parameters of cycle asymmetry  $r$  and base number of cycles  $N$  makes it possible to determine the fatigue resistance of materials and welded joints with allowance for cycle asymmetry within the range of multicycle region of fatigue life.

1. Lazan, B.I. (1965) Creep and fatigue properties under cyclic loading at elevated temperatures. Current aeronaut fatigue problems. In: *Proc. of Symp.*, Rome, 1965. Pergamon Press.

2. (1979) *Ontario highway bridge design code*. Ontario: Ontario Ministry of transportation and communications.
3. (1977) *Standard specifications for highway bridges*. 12th ed. Washington: American association of state highway and transportation officials.
4. (1985) *SNiP 2.05.03-84*. Bridges and tubes. Moscow: Strojizdat.
5. Trufiyakov, V.I. (1973) *Fatigue of welded joints*. Kyiv: Naukova Dumka.
6. (1991) *MU. RD 50-694-90*. Reliability in technique. Probabilistic method of fatigue calculation of welded structures. Moscow, GK SSSR.
7. Gorbunov, B.N. (1941) *Solid welded beams and bridges*. Moscow-Leningrad: Gosstrojizdat.
8. Kuzmenko, V.A., Ishchenko, I.I., Troyan, I.A. et al. (1981) Influence of loading frequency, temperature and asymmetry of cycle on durability of 1Kh2M and Kh18N9 high-temperature steels. *Problemy Prochnosti*, 2, 30-36.

## METHOD OF CALCULATION OF VOLTAGE DROP IN ELECTRODE STICKOUT LENGTH WITH ALLOWANCE FOR NON-LINEARITY OF THERMOPHYSICAL PARAMETERS

I.V. PENTEGOV and O.I. PETRIENKO

The E.O. Paton Electric Welding Institute, NASU, Kyiv, Ukraine

The offered method is valid for the electrode stickout area, i.e. from the nozzle inlet to stickout adjacent to the droplet. Expressions for determination of current values of voltage drop in the electrode stickout length as functions of temperature and relations between the current length of electrode stickout and temperature at the end of the given area of stickout are presented.

**Key words:** arc welding,  $\text{CO}_2$ , electrode stickout, method of calculation, voltage drop, temperature, investigations, approximation

It is known that the electrode stickout length and voltage drop on it are the one of major parameters influencing the process of consumable electrode arc welding. Many works [1-11] were devoted to the study of voltage drop in the electrode stickout length in  $\text{CO}_2$  welding. To determine values of this parameter, there are different experimental methods [9, 10], for example, of tungsten or copper probe, contactless methods. However, there are no now analytical methods making it possible to determine the voltage drop at any electrode stickout, unchangeable wire feed speeds and welding current.

The aim of the present work is to develop the new method of calculation of voltage drop in the electrode stickout length and to compare the results obtained with experimental data. It should be noted that the offered method of calculation is valid for different methods of consumable electrode welding at constant speed of wire feeding, for example, for the submerged-

arc and shielded-arc and other methods of welding without short-circuiting.

Figure 1 shows the calculated scheme of distribution of voltage drop in the electrode stickout length. The elementary region (element) of wire  $dl$  is moved in the direction to the droplet at the electrode end. Let us assume for  $dl$  element a system of coordinates, being fixed relative to wire and moved together with it at a constant feed speed  $v_f$ . Here, the temperature of element  $dl$  is increased and a process of heating has a dynamic nature.

In accordance with Ohm's law, the voltage drop  $dU$  at element  $dl$  of the electrode stickout can be written in the following form:

$$dU = I\rho(T) \frac{dl}{S_e} = j\rho(T)dl, \quad (1)$$

where  $I$  is the current, A;  $\rho$  is the specific electrical resistance of metal,  $\text{Ohm}\cdot\text{m}$ ;  $T$  is the current value of temperature of element  $dl$ , K;  $S_e = \pi d_e^2/4$  is the cross-section area of electrode of diameter  $d_e$ ,  $\text{m}^2$ ;  $j$  is the current density,  $\text{A}/\text{m}^2$ .



Consequently, the current value of voltage of the electrode stickout is determined by the expression

$$U_s(l) = j \int_0^l \rho(T) dl, \quad (2)$$

where  $l$  is the current value of electrode stickout length, mm.

Temperature  $T$  of element  $dl$  is the function of a current length of electrode stickout  $l$ , therefore, after substitution of integration variables, the expression (2) can be written in the form

$$U_s(T, T_0) = j \int_{T_0}^T \rho(T) \frac{dl}{dT} dT, \quad (3)$$

where  $T_0$  is the temperature of wire at the outlet from the nozzle, K.

To determine the derivative  $dT/dl$ , we shall use the differential equation of Fourier's heat conductivity [12]. We assume that radiation and convection losses are small at the electrode stickout area  $0 < l < l_1$  (see Figure 1), where the effect of heat conductivity can be neglected. Then, taking into account the one-dimensionality of the problem we shall write the Fourier's equation in the form

$$\gamma C_p(T) \frac{dT}{dt} = \rho(T) j^2, \quad (4)$$

where  $\gamma$  is the density of metal (steel),  $\text{kg}/\text{m}^3$ ;  $C_p(T)$  is the isobaric heat capacity of the mass unity,  $\text{J}/(\text{kg}\cdot\text{K})$ ;  $dT$  is the increment of temperature of the electrode stickout element  $dl$  during time  $dt$ .

For the system of coordinates considered the current length of electrode  $l$  is associated with a current time  $t$  by a linear relation  $l = v_f t$ . Using the latter, we shall substitute variable  $dt = dl/v_f$  in the equation (4)

$$\frac{dT}{dl} = \frac{\rho(T) j^2}{\gamma C_p(T) v_f}, \quad (5)$$

where  $v_f$  is the wire feed speed,  $\text{m}/\text{s}$ .

Substituting (5) and (3) we shall obtain

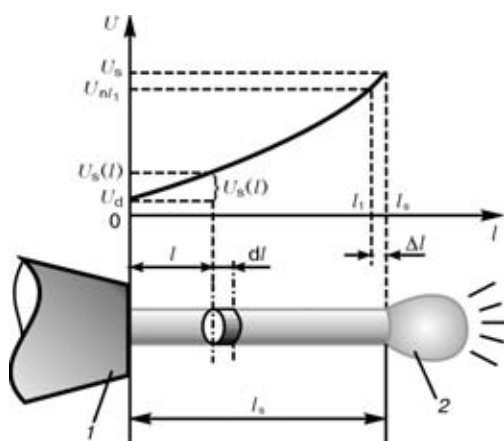


**Figure 1.** Scheme of distribution of voltage drop in electrode stickout length: 1 — nozzle; 2 — droplet (the rest designations are in the text)

$$U_s(T, T_0) = \frac{\gamma v_f}{j} \int_{T_0}^T C_p(T) dT. \quad (6)$$

This expression enables us to determine the current value of voltage drop at the electrode stickout as a function from  $T$ .

To determine the relationships between the temperature  $T$  and current length of electrode stickout  $l$ , we shall separate variables in formula (5) and integrate the expression obtained in the following ranges: temperature — from  $T_0$  up to current value  $T$ , and stickout length — from 0 up to current value  $l$ :

$$\int_{T_0}^T \frac{\gamma C_p(T)}{\rho(T)} dT = \int_0^l \frac{j^2 dl}{v_f}. \quad (7)$$

This results in the expression allowing determination of relation between the current value of the electrode stickout length and temperature at the end of the given region of the electrode stickout:

$$l(T, T_0) = \frac{v_f}{j^2} \int_{T_0}^T \frac{\gamma C_p(T)}{\rho(T)} dT. \quad (8)$$

Formula (8) is valid for the region of the electrode stickout from 0 to  $l_1$ , where the heat is realized only by the passing current and all the heat generated is used for increasing heat capacity of the metal when the heat flow from the droplet is not yet manifested, i.e.  $l_1 \approx 0.98 l_s$  (here  $l_s$  — full length of the electrode stickout).

Thus, the equations (6) and (8) preset the parametric form of writing dependence  $U_s(l)$ . These formulae confirm that the voltage drop depends on the metal density, its specific heat capacity, wire feed speed and current density.

It is known that power  $P(T)$  is generated during current passing in the electrode stickout at the area from the nozzle to the point of temperature  $T$ . This power can be written using the expression (6) as follows:

$$\begin{aligned} P(T, T_0) &= U(T, T_0) I = \frac{\gamma v_f \pi d_c^2}{4} \int_{T_0}^T C_p dT = \\ &= m_s (T - T_0) \frac{1}{T - T_0} \int_{T_0}^T C_p dT, \end{aligned} \quad (9)$$

where  $I = \pi d_c^2 j / 4$  is the welding current, A;  $m_s$  is the electrode wire mass consumption per second,  $\text{kg}/\text{s}$ .

At presence of a contact resistance in the point of contact of welding wire and nozzle of welding torch the power  $P_c(T_0)$  is generated, which leads to the electrode wire heating:

$$P_c(T_0) = U_c(T_0) I = m_s (T_0 - T_{\text{env}}) C_{p_{\text{st}}}(T_0), \quad (10)$$

where  $U_c(T_0)$  is the contact drop of voltage between the nozzle and wire, V;  $T_{\text{env}}$  is the temperature of welding environment, K;



$$C_{p_{av}}(T_0) = \frac{1}{T_0 - T_{env}} \int_{T_{env}}^{T_0} C_p(T) dT$$

is the mean value of specific heat capacity of wire metal for the temperature interval investigated.

As a result of this the wire at the nozzle outlet is occurred to be already heated to  $T_0$ . The contact voltage drop at the nozzle is determined by the expression

$$U_s(T_0, T_{env}) = \frac{\gamma v_f}{j} \int_{T_{env}}^{T_0} C_p(T) dT. \quad (11)$$

The actual voltage drop at the electrode stickout area between the nozzle and point  $l_1$  (see Figure 1) at  $T = T_1$  in the electrode stickout length, is equal to the sum of expressions (6) and (11) is found from the expression

$$U_{nl_1}(T_1) = \frac{\gamma v_f}{j} \int_{T_{env}}^{T_1} C_p(T) dT, \quad (12)$$

where  $T_1$  is the temperature at the electrode stickout length equal to  $l_1$  which lies in all the cases within the narrow interval of temperatures. Its value can be taken, for example, from publications [1, 13], where  $T_1 = 723$  K. The preliminary calculations showed that the temperature  $T_1$  is from 713 to 1044 K depending on the length of the electrode stickout.

Calculations of voltage drop were made for the region which is beginning at the wire inlet to the nozzle and completing by the length of the electrode stickout  $l_1$ , differing from the full length of stickout  $l_s$  for a value  $\Delta l$ , its value not exceeding 1–2 mm. At the region  $\Delta l$  such laws are valid, which are differed from the laws describing the heating of the electrode wire with a passing current. Moreover, the heating from a droplet has a great effect, and the voltage drop  $\Delta U$  in this region is 1–2 V. Special investigations will be devoted to this case.

The offered method made it possible to take into account the voltage drop in wire–nozzle contact, not knowing its resistance value. In addition, to determine the full voltage drop  $U_{nl_1}$  at electrode stickout length  $l = l_1$  it is not necessary to know the temperature  $T_0$  at the wire outlet from the nozzle.

The final variant of calculations has a parametric form of record of relationship  $U_s(l)$  (to point  $l_1$  with temperature  $T_1$ ):

$$\begin{cases} U_{nl}(T, T_0) = \frac{\gamma v_f}{j} \left[ \int_{T_{env}}^{T_0} C_p(T) dT + \int_{T_0}^T C_p(T) dT \right]; \\ l(T, T_0) = \frac{v_f}{j^2} \int_{T_0}^T \frac{\gamma C_p(T)}{\rho(T)} dT. \end{cases} \quad (13)$$

From the formulae obtained the calculations for electrode wires Sv-08G2S (C — 0.11; Si — 0.5; Mn — 1.4; Cr — ≤ 0.1 wt.%) of 1.2 and 2.0 mm

diameter in the electrode stickout length from welding torch nozzle to the area adjacent to the droplet were made (see Figure 1). Figure 2 gives the comparison of obtained data with experimental data [1] of voltage drop in the electrode stickout length.

Based on the calculated data at  $v_f = \text{const}$  and  $I = \text{const}$  the curves 1–8 were plotted, experimental data [1] are given by circles. In work [1] there are no data about the voltage drop in the electrode stickout length in certain points of stickout at  $v_f = \text{const}$  (the values of  $v_f$  were changed to change  $l_s$ ). Therefore, to obtain the intersection of curves with appropriate experimental points at a preset length  $l_s$  the authors used different values  $T_0$  for each experimental point. Figure 2 shows a good coincidence of calculated and experimental data.

It can be concluded on the basis of calculations: the higher electrode feed speed the lower contact drop of voltage that is coincided with experimental data, and the lower the wire temperature  $T_0$  at its inlet from the nozzle the lower voltage drop in the electrode stickout length.

From formula (13) the voltage drop in contact with wire–nozzle using welding wire of 1.2 mm diameter and  $T_0 = 485$ –625 K was 0.660–0.796 V; when welding wire of 2.0 mm diameter was used and  $T_0 = 515$ –690 K the voltage drop was 0.529–0.736 V. These data correspond to those of [1] where  $U_c = 0.6$ –0.9 V. However, it should be taken into account that in work [1] a non-optimized nozzle was, probably, used as this small value  $U_c$  cannot be obtained at the optimized nozzle [13], it is usually 4–6 V.

Curves in Figure 2 are plotted by formulae of the parametric form of record (13) using approximations of temperature relations of specific heat capacity and specific electrical resistance given in Figures 3 and 4.

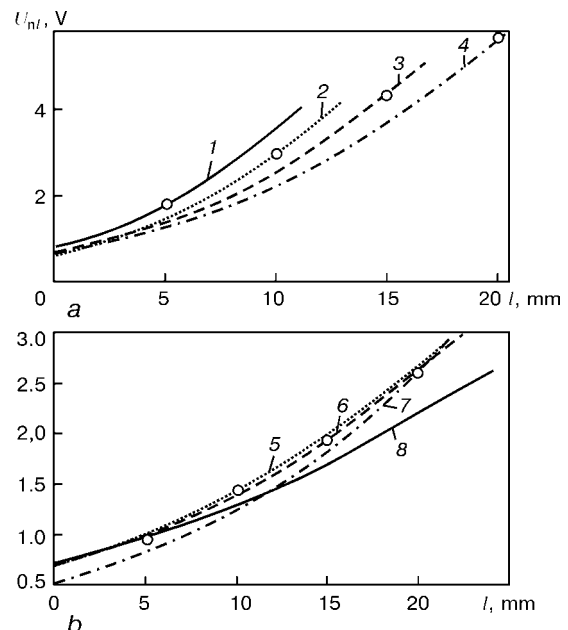


**Figure 2.** Curves of voltage drop in stickout length of electrode of 1.2 (a) and 2.0 (b) mm diameter at  $v_f = 0.180$  (1), 0.200 (2), 0.230 (3), 0.270 (4), 0.050 (5), 0.056 (6), 0.057 (7) and 0.068 (8) m/s (○ — experimental data)

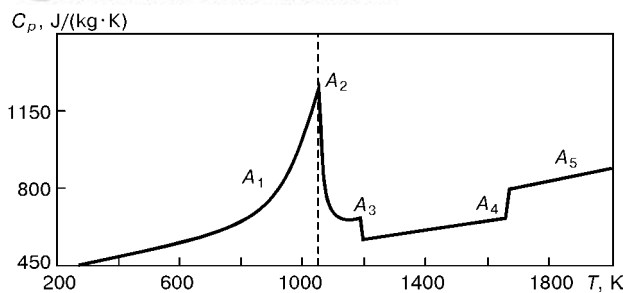


**Figure 3.** Approximation of relationship between specific heat capacity  $C_p$  of wire metal and temperature ( $A_1$ – $A_5$  — points of phase transitions)

Approximations have the following form:  
for specific heat capacity

$$C_p(T) = \begin{cases} 375 + 0.3T + 561.80 e^{-0.0105(T_C - T)} & \text{at } T \leq T_C, \\ 345 + 0.276T + 616.856 e^{-0.005(T_C - T)} & \text{at } T_C < T \leq 1190, \\ 290 + 0.232T & \text{at } 1190 < T \leq 1660, \\ 345 + 0.276T & \text{at } T > 1660, \end{cases} \quad (14)$$

for specific electrical resistance

$$\rho(T, C, Si, Mn, Cr, Ni, P) = \begin{cases} 0.031 \cdot 10^{-6} (1 + 0.006(T - T_0)) + 0.9 \cdot 10^{-6} e^{-0.0026(T_C - T)} + X_1 & \text{at } T \leq T_C, \\ 0.031 \cdot 10^{-6} (1 + 0.0035(T - T_0)) + 0.96 \cdot 10^{-6} + \\ + 0.095 \cdot 10^{-6} (1 - e^{0.02545(T_C - T)}) + X_1 & \text{at } T > T_C, \end{cases} \quad (15)$$

where  $T_C$  is the Curie temperature (1044 K);  $X_1$  is the coefficient of chemical composition of wire Sv-08G2S:

$$X_1 = 0.34 \cdot 10^{-6} C + 0.135 \cdot 10^{-6} Si + 0.05 \cdot 10^{-6} Mn + 0.054 \cdot 10^{-6} Cr + 0.015 \cdot 10^{-6} Ni + 0.11 \cdot 10^{-6} P.$$

The approximations of temperature relationships (to 1700 K) of specific heat capacity at constant pressure and specific electrical resistance  $\rho$  for pure iron from the data of work [14] and for welding wires Sv-08A, Sv-08G2S, Sv-18KhMA (GOST 2246-70) are given. In Figure 3 the temperature relationships of specific heat capacity at constant pressure of the purest iron from data of Goletsko [14, 15] were taken as a basis.

## CONCLUSIONS

1. The obtained equations are presented in the form of a parametric relationship of distribution of voltage drop in the electrode stickout length as a function of temperature with a allowance for a non-linearity of thermophysical parameters, i.e. specific electrical resistance and specific heat capacity.

2. Such parameters as current, wire feed speed, initial temperature of wire at its inlet from the nozzle, which depends in turn on a contact resistance in the nozzle, greatly influence the voltage drop in the electrode stickout length.

3. The full drop of voltage at the nozzle-droplet area can be calculated not knowing the values of a contact resistance in the nozzle and initial temperature of wire at its outlet from the nozzle.

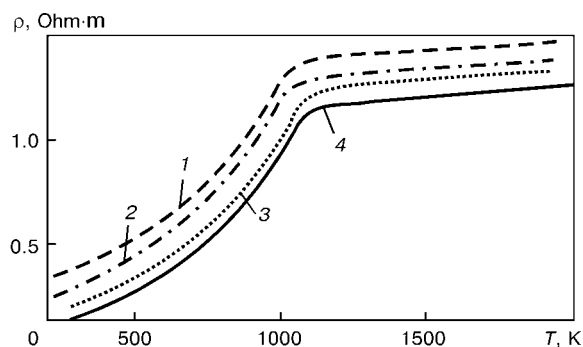


**Figure 4.** Approximation of relationship between specific electrical resistance  $\rho$  of pure iron and welding wires of different grades and temperature: 1 — Sv-08G2S; 2 — Sv-18KhMA; 3 — Sv-08A; 4 — pure iron

4. With increase in electrode wire feed speed the contact resistance in the nozzle is decreased.

5. The calculations of specific heat capacity and specific electrical resistance and also electrode heating by passing current and the family of curves, plotted by the data obtained, are coincided with already known experimental results in this field of investigations (in present work — for pure iron and wires Sv-08G2S, Sv-08A, Sv-18KhMA). The offered model of calculation of the voltage drop in the electrode stickout length is more precise and valid, as compared with existing models, as it reflects the processes proceeding in the power source–welding arc system. Using this model it is possible to calculate all the main parameters at different conditions of consumable electrode welding and to design new power sources with improved properties.

1. Koshkaryov, B.T., Mikhajlov, A.N., Budnik, N.M. (1971) Influence of stickout on electrode melting in  $CO_2$  welding. *Svaroch. Proizvodstvo*, **11**, 30–32.
2. Rykalin, N.N. (1951) *Calculations of thermal processes in welding*. Moscow: Mashgiz.
3. Paton, B.E. (1953) *Automatic electric arc welding*. Kyiv: Mashgiz.
4. Shejnkina, M.Z. (1978) Determination of admissible stickout of thin electrode wire in  $CO_2$  welding. *Svaroch. Proizvodstvo*, **9**, 24–28.
5. Zaruba, I.I., Kasatkin B.S., Kakhovsky, N.I. et al. (1966)  *$CO_2$  welding*. Kyiv: Tekhnika.
6. Potapievsky, A.G. (1974) *Gas metal arc welding*. Moscow: Mashinostroenie.
7. Akulov, A.I. (1966) About quantity of heat introduced in arc by electrode heated in stickout. *Avtom. Svarka*, **5**, 35–38.
8. Poklady, V.R. (1973) *Study and development of semi-automatic welding technology with increased electrode stickout in  $CO_2$ -O mixture*. Synopsis of Thesis for Cand. of Techn. Sci. Degree. Kyiv: PWI.
9. Doronin, V.P., Popkov, A.M. *Method of measuring of voltage drop on electrode stickout*. USSR author's cert. 466969, Int. Cl. B 23 K 9/00. Publ. 07.01.76.
10. Doronin, V.P., Elantsev, A.I. (1975) Measuring of voltage drop on electrode stickout and arc in short-circuit transfer welding. In: *Problems of welding manufacturing*. Transact. of Chelyabinsk Polytechnical Institute.
11. Bezakh, D.K. (1962) Use of electrode preheating to improve the welding productivity. *Avtom. Svarka*, **4**, 33–36.
12. Belyaev, N.M. (1989) *Fundamentals of heat transfer*. Manual. Kyiv: Vyscha Shkola.
13. Chubukov, A.A. (1980) Resistance of tip-electrode wire contact in  $CO_2$ -welding. *Svaroch. Proizvodstvo*, **12**, 31–32.
14. Goudremont, E. (1966) *Special steels*. Moscow: Metallurgiya.
15. Chirkin, V.S. (1959) *Thermophysical properties of materials*. Moscow: Fizmatgiz.



# PROPERTIES OF MAGNETRON COATINGS ON THE Fe–Cr–Ni BASE WITH AMORPHOUS STRUCTURE

G.N. LUKINA, M.V. BOLSHAKOV and S.Ya. PIDGAJCHUK

National University «Lvivska Polytekhnika», Lviv, Ukraine

Structure and properties of coatings produced by magnetron sputtering of targets of stainless steel of the 18-10 type with molybdenum additions have been investigated. As shown by X-ray diffraction analysis, the Fe–Ni–Cr–Mo coatings are characterised by an amorphous structure, stable in the 293–823 K range. The coatings are proved to have high values of microhardness (8.5–9.0 GPa) and corrosion resistance in aqueous salt solutions.

**Key words:** *coatings with amorphous structure, magnetron sputtering, corrosion resistance, protective-decorative coatings*

High values of anti-corrosive properties and a combination of physical-chemical characteristics of alloys with an amorphous structure offer wide prospects for their commercial application in the form of coatings.

Magnetron sputtering provides a substantial decrease in heating of the surface due to its decreased bombardment by secondary electrons [1], thus making it possible to achieve high cooling rates in formation of coatings, which are required for their amorphisation. This circumstance makes the magnetron sputtering method most promising for production of coatings with an amorphous structure, compared with the known methods of vacuum condensation deposition. In addition, the above coatings, unlike thermal spray ones, require no subsequent machining and have an attractive appearance, which determines their wide application for protective and decorative purposes.

Objectives of the present study were as follows:

- evaluation of the possibility of producing coatings with an amorphous structure on metal parts by the method of magnetron sputtering of targets based on Cr–Ni stainless steels alloyed with molybdenum;
- investigation of structure of the resulting coatings by X-ray diffraction analysis, depending upon their chemistry and conditions of subsequent heat treatment, as well as comparison of their corrosion resistance.

The choice of molybdenum for alloying the coatings is based on the fact that it promotes stabilisation of the amorphous structure, increases corrosion resistance, improves mechanical characteristics and raises thermal stability of the alloy [2].

Coatings 4–9  $\mu\text{m}$  thick were deposited on samples of steel 40Kh (C — 0.4; Cr — 1.0 wt.%). Targets for sputtering were made from sheet steel 08Kh18N9T (C — 0.08; Cr — 18.0; Ni — 9.0; Ti — 0.6 wt.%). Composite targets with molybdenum inserts, which were mechanically fixed in rectangular grooves made in the stainless steel targets, were used to produce coatings of the Fe–Ni–Cr–Mo system with a differing molybdenum content of the coatings. Mass fraction of molybdenum within a range of 5–15 % (calculation)

was regulated by varying the area of the inserts in the active zone of erosion of the targets. The upper limit of the content of molybdenum was chosen on the basis of ecological factors and its relative shortage as an alloying element. Sputtering was performed under the following conditions: working pressure of argon in the chamber was  $3 \cdot 10^{-1}$  Pa, working voltage was 600 V, discharge current was 4 A, deposition rate was  $16\text{--}20 \text{ nm} \cdot \text{s}^{-1}$  and temperature of heating of the samples during the coating process was not in excess of 373 K. The time of sputtering was varied from 1 to 3 h to produce coatings of differing thickness. Prior to deposition of the coatings, to activate the surface and increase their adhesion strength the samples were subjected to preliminary treatment in argon plasma with an energy of ions equal to 200 eV for 1–1.5 h.

Structure of the coatings (packing character, degree of dispersion of atom groups and their mean sizes) was investigated by X-ray diffraction analysis with the DRON-3 instrument in a filtered iron radiation (Fe- $K_{\alpha}$ ) using different attachments. Sizes of the coherent scattering blocks were determined from widening of interference fringes by the approximation method, as it provides a high accuracy for crystalline grains with a size ranging from 10 to 150 nm. Because of small thickness of the coatings, the investigations were conducted at small incidence angles to decrease the effective depth of penetration of X-rays. The method of reverse filming was employed to estimate integral intensity and position of diffraction lines at specified angles. The high-temperature investigations were carried out in a special chamber in the high-purity helium atmosphere. Corrosion resistance of the coatings was studied using the P-5827G potentiometer by recording anode polarisation curves in 3 % NaCl aqueous solution under potentiodynamic conditions. Estimation of microhardness, according to GOST 9450–76, was conducted on transverse sections of the coatings with the PMT-3 microhardness meter using a quadrangular pyramid with a rhombic base (Knoop pyramid).

The atomic density radial distribution function (ADPDF) is an important characteristic of the amorphous structure of alloys. This function is obtained by reducing the curve of angular dependence of the

**Table 1.** Characteristics and properties of experimental coatings

Target material	Coating thickness, $\mu\text{m}$	Microhardness, GPa	Coherent scattering block sizes, nm	Coating structure
Steel 08Kh18N9T	Without coating	2.0	30	Crystalline
Steel 08Kh18N9T	6	5.0	11	Microcrystalline
Steel 08Kh18N9T + 5 % Mo	9	8.5	–	Amorphous
Steel 08Kh18N9T + 15 % Mo	9	9.0	–	Same

intensity of scattering of X-rays to electron units. Given that the coatings investigated are multicomponent ones, the structural factor was calculated by averaging the atomic factor [3].

As follows from the results of structural investigations (Table 1), in the case of using the steel 08Kh18N9T targets the deposited coatings have a microcrystalline structure, and the coherent scattering blocks are much decreased in size (approximately by a factor of 3, i.e. to 11 nm), compared with a material before sputtering (target), which is accompanied by an increase in microhardness. Similar coatings alloyed with molybdenum are characterised by a higher microhardness and have an amorphous structure. Diffraction patterns (Figure 1) show a wide diffusion halo in a range of reflection angles  $\theta = 35\text{--}65^\circ$  at the absence of diffraction peaks of crystalline phases of the alloy. Some bifurcation of the main interference maximum, which decreases with an increase in the amount of molybdenum in the coating, is indicative of an insignificant structural heterogeneity of the coatings. Therefore, an addition of molybdenum to the coatings based on the Fe–Ni–Cr system favours formation of their amorphous structure and leads to their substantial hardening.

In view of the established amorphous structure of the Fe–Ni–Cr–Mo system coatings, it is important to study the problem of similarity of the amorphous and polycrystalline structures in the short range ordering region. This problem was solved by using the method of integrated analysis of the intensity curves, which consists in plotting ADRDF and structural factor from experimental data of angular distribution of the intensity of a scattered radiation of the Fe–Ni–Cr–Mo system coatings (Figure 2). The general view of structural factors (Figure 2, *a*) is similar to typical structural factors for unordered systems, the only difference lying in the fact that there is a clearly defined

intensity peak on the side of small angles. Experimental studies of alloys with the amorphous structure showed that the far range structural ordering and periodicity of arrangement of atoms are absent in this case. There is some short range ordering which can be well determined at a distance between the two neighbouring atoms, although the correlation between the atoms in their relative arrangement rapidly attenuates with an increase in distance from a selected atom [2].

Positions of maxima were compared with positions of the corresponding maxima for polycrystalline components of the alloy.  $\gamma$ -Fe was found to be characterised by the best correspondence of the main maxima. Positions of maxima depending upon the wave factor  $S = 4\pi/\lambda \sin \theta$  (where  $2\theta$  is the angle of scattering of X-ray radiation and  $\lambda$  is the wave length) for them is as follows (Table 2).

The first peak cannot be compared with lines for polycrystalline components of the alloy or compounds, which is indicative of their different nature. As this maximum is located on the side of smaller scattering angles, it may correspond to certain structural groups of larger sizes, i.e. of the type of clusters. A coating with a higher molybdenum content is characterised by a less defined structural factor (the first and second maxima are smaller in height and width), which is indicative of an increased degree of heterogeneity of the coating structure.

The ADRDF values computed using PC by means of the integral Fourier transformation were employed for a more comprehensive analysis of structure of the coatings (Figure 2, *b*). The main structural parameters (probable atomic distance and mean coordination number) were determined from the above values.

The first maxima of ADRDF are smeared, and areas beneath them, equal to about 3, are insignificant. These maxima correspond to interatomic distances which are approximately equal to 0.2 nm, this being indicative of existence of regions with a loose atomic packing in the coatings. The main coordination maxima are more clearly defined and correspond to

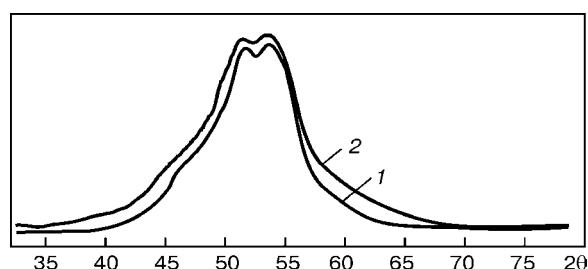


**Figure 1.** Diffraction patterns of magnetron coatings of the Fe–Ni–Cr–Mo system produced by sputtering targets of different chemistry: 1 – steel 08Kh18N9T + 5 % Mo; 2 – steel 08Kh18N9T + 15 % Mo

**Table 2.** Position of maxima on the structural factor curves

Investigation object	$S, \text{nm}^{-1}$		
	Peak 1	Peak 2	Peak 3
Fe–Ni–Cr–Mo system coating	10	30.0	37.0
$\gamma$ -Fe	–	30.3	34.9

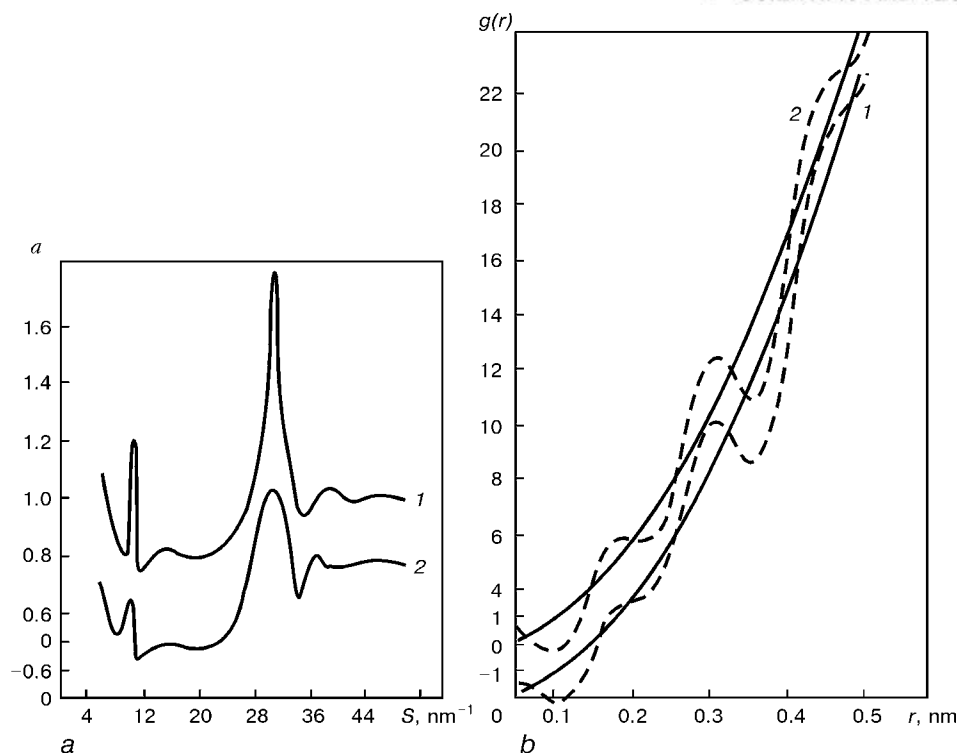


**Figure 2.** Structural factor (*a*) and radial distribution function (*b*) at 293 K for the Fe-Ni-Cr-Mo system coatings with amorphous structure produced by sputtering targets of different chemistry:  $g(r)$  – ADRDF;  $r$  – distance from a fixed atom;  $a$  – structural factor;  $S$  – wave factor (see designations in Figure 1)

an interatomic distance of 0.305 nm. The area under the main coordination peak was computed from the resulting distribution functions, as this area directly characterises the packing density and is one of the basic short range ordering parameters. Coordination number for the Fe-Ni-Cr-Mo system coatings was found to be 12.3 and 12.4, depending upon the molybdenum content. Such values of the areas are indicative of the fact that the atomic distribution is the densest. Also, this points to the fact that the similarity with  $\alpha$ -Fe is a larger than with  $\gamma$ -Fe, as the coordination number for the former is 12 and that for the latter is 8. Some exceeding of the coordination number of the coatings over that of  $\gamma$ -Fe is indicative of a substantial imperfection of the atomic ordering, which is caused by a complex alloying of the coating.

It can be concluded on the basis of the above data that the short range ordering of the coatings with an amorphous structure is characterised by a dense packing of atoms with the mostly metallic character of binding, and is similar to the crystalline structure of iron with the face-centred cubic lattice. A drawback of the majority of alloys with the amorphous structure is a very low thermal stability of the amorphous state, i.e. a low value of the devitrification temperature (transition from the amorphous to crystalline state), which is normally accompanied by a dramatic deterioration in mechanical and physical-chemical properties [2]. Radiography was conducted in the high-temperature chamber with the high-purity helium atmosphere to prevent oxidation at temperatures of 293–823 K and at a holding time of 1–2 h. Direct radiography at different temperatures proved that the amor-

phous structure of the coatings investigated was very stable within a wide temperature range.

The intensity of the main interference maximum, the profile of which at different temperature is shown in Figure 3, was fixed. As can be seen, no substantial or cardinal changes were revealed in a temperature range of 373–523 K. In heating to 823 K the coating structure remained amorphous, and its basic characteristics did not change. The absence of insignificant bifurcation of maximum at heating temperatures of 373–473 K evidences disappearance of microregions with an insignificant structural heterogeneity. Therefore, the addition of molybdenum to the coatings was

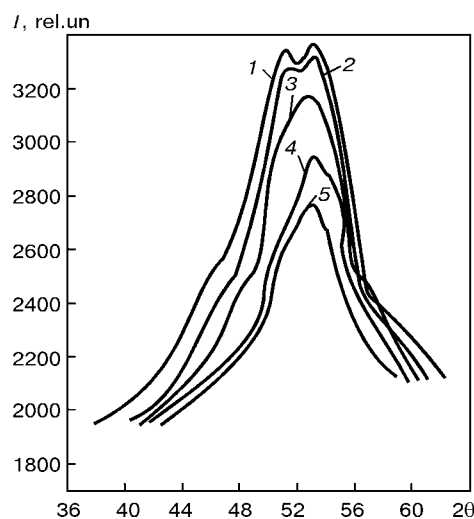


**Figure 3.** Curves of intensity  $I$  of the main interference maximum of the Fe-Ni-Cr-Mo system coating at different temperature values, K: 1 – 293; 2 – 373; 3 – 573; 4 – 673; 5 – 823

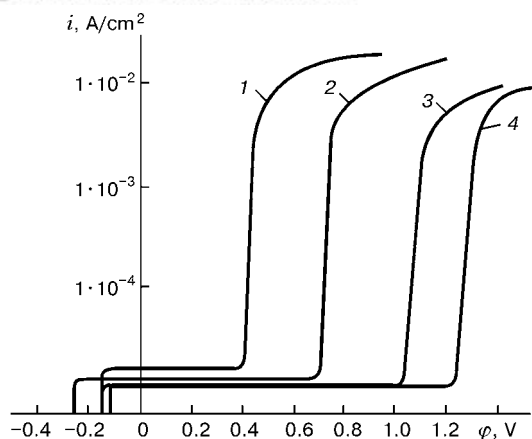


**Figure 4.** Anode polarisation curves: 1 — steel 08Kh18N9T; 2 — coating produced by sputtering the steel 08Kh18N9T target; 3 — same, steel 08Kh18N9T + 5 % Mo; 4 — same, steel 08Kh18N9T + 15 % Mo;  $\phi$  — stationary electrode potential

proved to provide thermal stability of the amorphous structure up to a temperature of 823 K.

The anode polarisation curves were plotted under potentiodynamic conditions at a rate of superposition of potentials equal to 2 mV/s at a temperature of 293 K in order to generate comparative data on corrosion resistance of the Fe–Ni–Cr and Fe–Ni–Cr–Mo system coatings with the amorphous and microcrystalline structures. Analysis of the polarisation curves (Figure 4) shows that the stationary electrode potential of the majority of these coatings is within a range of  $-0.12$  –  $-0.21$  V with respect to a saturated chlorine–silver electrode. All the coatings are characterised by a rapid formation of passive protective films at a low current density  $i$  ( $\approx 1 \cdot 10^{-5}$  A/cm<sup>2</sup>). The Fe–Ni–Cr system coating has a more extended passivation region, compared with steel 08Kh18N9T in the initial state. Widening of the passivation region of the microcrystalline coatings based on stainless steel is attributable to more homogeneous and stable chromium oxide based films formed on the coating surface. It can be assumed that a high stability of these films is associated with a ready enrichment of the passivating films with chromium, owing to the microcrystalline structure of the coating.

Addition of molybdenum to the coating leads to formation of large passivation regions (from  $-0.12$  to  $+1.1$  V) with a decreased passivation current density, compared with coatings having a crystalline structure. Factors that favour an increase in corrosion resistance of the Fe–Ni–Cr–Mo system coatings include the posi-

tive effect of molybdenum, which is evidenced by widening of the passivation region with an increase in its content of the coatings (Figure 4) and by their amorphous structure. Apparently, molybdenum becomes part of composition of the passivating films, thus increasing their stability. But first of all, high corrosion resistance of the Fe–Ni–Cr–Mo system coatings is attributable to the fact that the passivating films have high density, as they are formed on a defect-free base of the coating with the amorphous structure (absence of dislocations, grain boundaries), which prevents pitting. In addition, the amorphous state is metastable in nature, which leads to a fast self-recovery of the passivating films after damage.

Therefore, the Fe–Ni–Cr–Mo system coatings have the highest corrosion resistance among other materials investigated, and provide an efficient protection of metal parts in aggressive environments containing chlorine ions.

## CONCLUSIONS

1. Addition of 5–15 % molybdenum to coatings produced by magnetron sputtering of composite targets based on stainless steel 08Kh18N9T is favourable for their amorphisation. In this case the short range ordering of the amorphous phase is of a type similar to the crystalline structure of  $\gamma$ -Fe with the fcc lattice.

2. As shown by direct radiography, the amorphous structure of the Fe–Ni–Cr–Mo system coatings is stable within a temperature range of 293–823 K.

3. The Fe–Ni–Cr–Mo system coatings with the amorphous structure have high values of microhardness (8.5–9.0 GPa) and corrosion resistance in aggressive aqueous environments containing chlorine ions, and are insensitive to pitting formation. An increase in the molybdenum content of the coatings has a positive effect on the above characteristics.

4. The combination of properties of the Fe–Ni–Cr–Mo system coatings with the amorphous structure makes it possible to recommend them for deposition on various metal parts for protective and decorative purposes, for operation under atmospheric and sea corrosion conditions.

1. Danilin, B.S., Syrchin, V.K. (1982) *Magnetron sputtering systems*. Moscow: Radio i Svyaz.
2. Suzuki, K., Fuzimori, H., Hashimoto, K. (1987) *Amorphous metals*. Moscow: Metallurgiya.
3. Skryshevsky, A.F. (1980) *Structural analysis of liquids and amorphous bodies*. Moscow: Vysshaya Shkola.



# FLOATING WELDED MEGASTRUCTURES (REVIEW)

V.N. BERNADSKY, S.Yu. MAKSIMOV and M.A. NETREBSKY

The E.O. Paton Electric Welding Institute, NASU, Kyiv, Ukraine

The paper presents a review of Japanese publications, devoted to world's first experience of designing, construction and studying the performance of floating welded megastructures

**Key words:** *design, fabrication, mounting, underwater welding, quality control, welded structure, off-shore floating construction, corrosion, service, repair*

The idea of creating floating off-shore structures of super-large dimensions, so-called floating megastructures (FMS) originated and found its practical application in Japan. This is exactly where the greatest experience of construction of large floating structures has been accumulated, namely ocean ships, off-shore platforms, piers, etc. Some of the largest floating structures are «Sea Giant» tanker 440 m long, 58.8 m wide with 28.8 m draft and sea oil storage facility «Hiroshima» 397 m long, 82 m wide with 25.5 m draft. Such huge facilities were mainly manufactured in ship-building yards in the docks or berths. Their dimensions were limited just by the capabilities of a specific fabrication. The idea of FMS was based on developing a structure of a much larger scale — of up to several kilometer length. Such a task had no precedent in the world practice. In order to implement it (build the FMS and conduct full-scale testing of the proposed engineering and design solutions) 17 steel-making and ship-building companies of Japan formed in April, 1995 a Technological Research Association MEGA-FLOAT (TRAMF) that carries out the entire package of scientific, design, engineering and production developments [1, 2].

Over the period of three years an experimental sample of FMS of 2×60×300 m size was designed and built, which was followed by making in 1998 a three-year program, including investigations of various aspects of the problem of FMS development, in particular the possibility of their practical use. Investigations led to construction of a full-scale model of a floating airport 1 km long, 120 m wide and 3 m high (Figure 1). The full-scale model was fitted with systems of instrument landing, landing beacons, glide-path systems and other modern equipment.

Development of the above structure required solving a number of problems, one of the principal of which was the maximum allowance for the features of sea wave impact on a floating platform of such dimensions. Unlike vessels, the FMS does not rock on a wave, but sways or vibrates. Vertical vibrations induced by a wave propagate along the structure, imparting it a very slight motion in the vertical plane,

which is not typical of regular ships, but is inherent in elastic «thin-walled» bodies of the type of huge flat structures afloat. The interaction of an elastic body and a liquid medium is of a complex nature, being, however, easily modelled in such a way as to be able to provide a quantitative estimate of various characteristics. Individual elements of a floating body are taken to be material points. Analysis of these points motion yields a system of equations to determine the parameters of FMS motion as a whole.

Research performed allowed determination of the characteristics required for FMS design. The design process included a number of independent stages the following of which can be singled out [3]: simulation of the floating body as a flat rectangular plate; calculation of the schematic of structure vibration (calculation of the level of inherent vibrations); calculation of maximum magnitudes of mass and bending moment, vertical acceleration and surface stresses of a flat body; modeling the inner part of the structure; stress analysis in the structure inner part; determination of stresses induced by the inherent mass and working load by the results of statistical calculation; analysis and assessment of the ultimate static strength; fatigue resistance and ultimate service life.

A designed and manufactured full-scale model of 9500 t weight and area of  $8.4 \cdot 10^4 \text{ m}^2$  in the form of a box-shaped pontoon consisted of six modules, the largest of which was 383 m long and 60 m wide [1]. The modules were primarily made of blocks, having



Figure 1. Development of FMS — a model of a floating airport

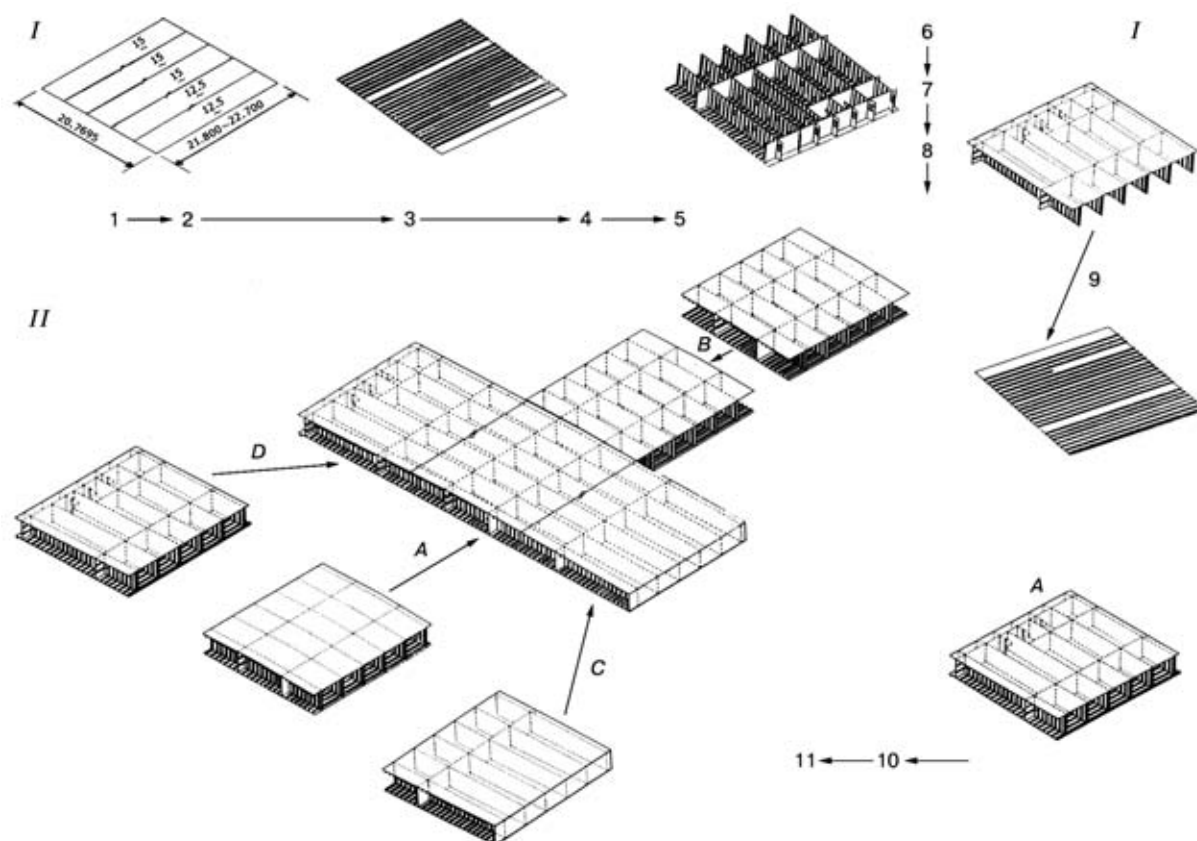


**Figure 2.** Fabrication of FMS blocks and modules: *I* — technological sequence of an individual block fabrication (1 — base platform, upper flooring; 2 — welding of blocks; 3 — preliminary welding of longitudinal stays; 4 — mounting; 5 — welding; 6 — control; 7, 11 — painting; 8 — tilting; 9 — arrangement, mounting on the bottom and welding on; 10 — control); *II* — schematic of assembly of part of FMS module of individual blocks (*A–D* — assembly algorithm)

longitudinal and transverse partitions, as well as a set of stiffeners, covered with steel plates on all the sides [4].

Modules were made by a regular module-by-module sequence, used in ship-building [4] in construction of oil tankers that in the general terms consists in successive assembly and joining of the longitudinal and transverse partitions on a platform (i.e. lower part plating), while meeting the stringent requirements for provision of the joint quality and tightness, as well as guaranteeing a long-term service under sea conditions.

The largest module consisted of 51 blocks (3 by width and 17 along the length). The size of each block of 180–190 t weight was 3.0×20.0×22.7 m. Transverse partitions were mounted every 4 m, extreme blocks had one longitudinal partition and the middle block — two (with the total width of the module of 60 m). Spacing of the stiffeners (longitudinal stays of the deck and the bottom) was 811 mm (Figure 2).

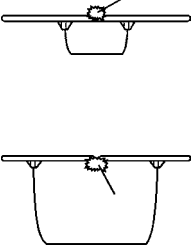
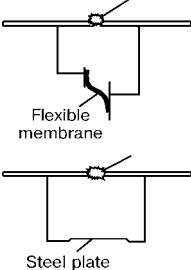
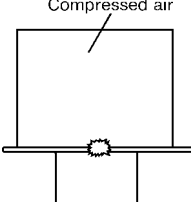

After fabrication the blocks were assembled into modules in the berth. The inner part of the module had compartments of the type of ballast tanks and air cavities for adjustment of draft. Since shop conditions allowed modules of greater dimensions to be made, their number in FMS was minimum. This enabled shortening the scope of operations on modules joining in open sea, improving the efficiency of operations and FMS quality, as a whole.

When modules were joined on the water surface, specific problems arose not characteristic of the technology of fabrication of such structures under regular conditions on the ground [5]: ability to apply welding is limited by the level of modules swaying relative to each other; structures afloat develop higher deformation than on the ground (deformations, because of the difference of temperature on the deck heated by the solar rays and in the underbody shell; and asymmetrical joints, because of module joining predominantly from one side, where the mooring devices are located); need to perform underwater welding; inability to provide siting in open sea that would be a position reference. Therefore, very important is monitoring of the dimensions of a structure continuously exposed to swaying and deformations.

It is obvious that the most serious problems in joining the modules were related to the accuracy and rigidity of their fastening [1]. During abutment the modules rock freely on the waves. Various devices of the type of guides, jacks, swivels, couplings, etc. were used to gradually reduce their swaying relative to each other. To avoid or minimise the variation of gaps at final assembly, the modules were further loaded with ballast to reduce their buoyancy.

Proceeding from the established practice, floating structural elements can be joined either by welding or using mechanical connections, i.e. intermediate elements, that are mechanically fastened to each other.

## Welding of floating structure elements below the water-line

«Dry» welding		«Wet» welding	
Outer chamber	Connected air chamber	De-watering with compressed air	Welding with local de-watering
			
Point of contact of chamber with the module bottom is sealed and water is pumped out. Depending on chamber dimensions, work is performed only from inside the module or on both sides	After fastening the joined modules a small chamber is formed on the outside, from which water is pumped out. When a flexible membrane is used, the cavity forms right after mounting and drying	Chamber walls are welded to the module bottom from both sides. Water is ousted at the expense of feeding compressed air from outside	Welding is performed at direct contact with the ambient water. Automatic welding with local de-watering

This provides a sufficient strength and time saving. There is a real danger, however, that lack of continuity of the formed joints on a microlevel may lead to stress concentration in these points. Considering the anticipated FMS service life (100 years), requirements for the joints and cost factors, welding was selected as the most suitable method of assembly of the modules into one FMS.

Welding of the upperworks did not run into any difficulties, unlike welding below the water-line. Two methods, applied in practice («dry» and «wet» welding) have their disadvantages and advantages. «Dry» welding is performed, using regular electrode materials and provides the welded joint quality similar to that produced in air. In order to implement it, however, it is necessary to dry up the space adjacent to the edges to be welded. «Wet» welding differs by simplicity and versatility, does not require any additional cost for the protection of the arc and the weld pool from ambient water. However, in this case special electrode materials are required. In addition, only highly qualified divers-welders can perform it. Considering the quite extensive volume of welding operations and increased requirements to the joint quality, the developers decided that application of «wet» welding is not rational in terms of cost and engineering aspect.

Several approaches were used to remove water from the welding zone, depending on the features of a specific assembly (Table), each of which has its features consisting in the use of plates-inserts and/or metal backing. When hydraulic packing was used, the elements of both the modules to be joined below the water level, were isolated using rubber seals right after fit up and fastening. Water was pumped out of the formed space. In some cases the bottom of the external chamber was left open to have unrestrained access to the welding site from the outside, and in

order to remove water on the inside, a second chamber was mounted where compressed air was fed. Depending on the dimensions of chambers, determining the possibility of man's access to the site of work performance, welding was performed from one or two sides. In the first case, ceramic backing, copper shoes or permanent metal backing were used.

Despite application of diverse methods of fastening the modules to be joined, it was not possible to completely avoid their microvibration. Therefore, comparative testing of welded joints was conducted with various methods of de-watering the welding zone. As a result, water removal by feeding compressed air was recommended as the main process.

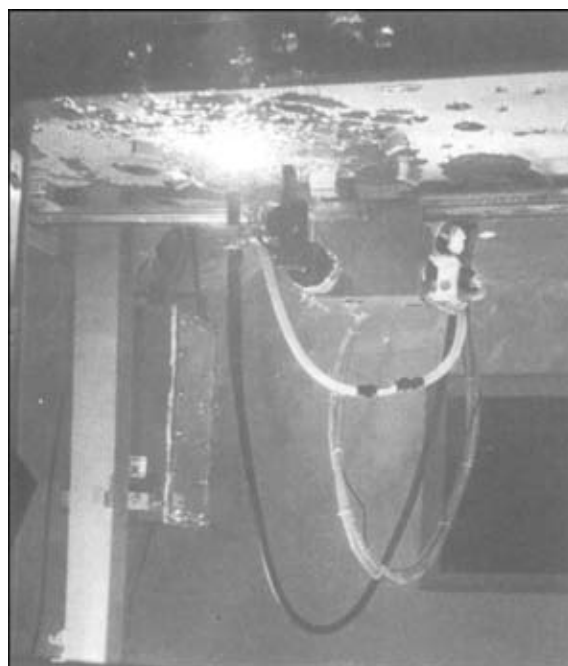
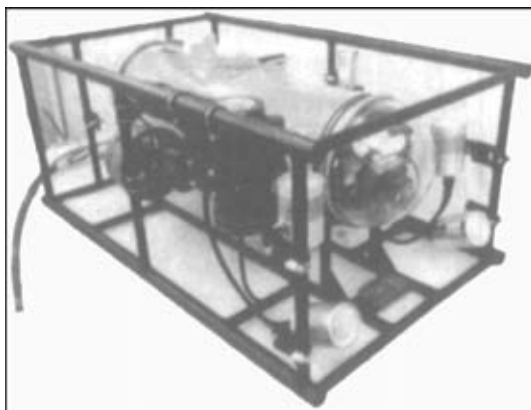


Figure 3. Underwater mechanised welding in the overhead position



**Figure 4.** Experimental set-up with permanent storage and video camera for monitoring FMS underbody

Computer application allowed determination of the optimal welding modes, providing minimal linear error when extended welds are made, namely 30 mm per 1000 m of weld. In addition, welding was performed at night to lower the level of deformations induced by temperature difference between the module underbody and upperworks heated by the sun. Depending on depth portable semi-automatic machines («dry» welding near the water-line) or automatic machines (welding with local drying up of the bottom in the overhead position) of a special design were used (Figure 3). The main work on underwater welding was performed by Sumitomo Heavy Industries that has experience of construction afloat of large-capacity vessels with up to 21 m draft and of repair operations at the depth down to 53 m.

As the anticipated service life of FMS should not be less than 100 years, it was necessary to envisage all the measures to provide its reliability in service. Therefore, the following problems were addressed under the project [6]: development of a system of optimal protection from corrosion; studying the ability to apply advanced materials; development of the technology of long-term monitoring; development of the technology for underbody repair.

During project implementation a system of corrosion protection was developed that includes the use of Ti-plated steel sheets in the variable wetting zone, a combination of paint coat and anode protection of the bottom, a method of moisture removal from the inner sections. The method of corrosion protection of sea structures with titanium application was developed by Nippon Steel and implemented in fabrication of tubular steel piles with facing with a thin titanium sheet for construction of bridges and mooring [2].

Control of FMS condition was performed using the following specialised equipment: units for external flaw detection, used for recording deformations

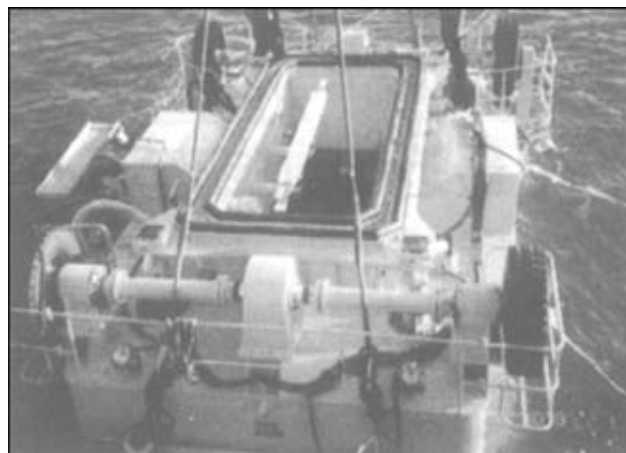


**Figure 5.** A unit for repair-restoration work under the water

and degree of corrosion damage; an NDT robot, fitted with special equipment for ultrasonic and magnetic defectoscopy, designed for measurement of wall thickness and crack detection in welds; multi-purpose unit with permanent storage for monitoring the FMS underbody, fitted with a device to produce acoustic images, video camera and a device for corrosion potential measurement (Figure 4).

In order to perform repair-restoration work under water, a special unit was developed (Figure 5), which was fitted with a positioner, working chamber with the equipment for «dry» welding, grips and NDT means.

Fabrication, mounting and monitoring the performance of FMS (a floating aerodrome in full-scale testing) confirmed the actual possibility of creation of such constructions, and the developed fundamentally new design and engineering solutions provided the high reliability of novel ingenious sea structures. MEGA-FLOAT Association plans further improvement of the procedures of calculation and technologies of fabrication of FMS to expand the capabilities of designing such huge welded structures for new floating facilities.

1. Okamura, H. (2000) Development and practical of mega-float. *J. JWS*, 4, 44–47.
2. Torii, T., Hayashi, N., Kanai, H. et al. (2000) Development of a very large floating structure. *Nippon Steel Technical Report*, 82, 23–34.
3. Sato, C. (2000) Principal characteristic of mega-float and its structure planning flow. *J. JWS*, 4, 48–52.
4. Kawai, M., Toyota, M., Kida, A. et al. (2000) Structure and construction of the unit-A, which is a component of the floating airport model for the MEGA-FLOAT R&D Program Phase II. *Ibid.*, 53–58.
5. Yamashita, Y. (2000) Joining technologies for very large floating structures. *Ibid.*, 59–62.
6. Yamada, M. (2000) Corrosion protection and maintenance of mega-float. *Ibid.*, 63–67.



# DEVELOPMENT OF LASER TECHNOLOGIES FOR MATERIALS TREATMENT AT THE INSTITUTE FOR PROBLEMS OF LASER AND INFORMATION TECHNOLOGIES

V. Ya. PANCHENKO and V. S. GOLUBEV

Institute for Problems of Laser and Information Technologies of the Russian Academy of Sciences, Shatura, Russia

New trends in upgrading equipment and technology for laser treatment of materials, developed at the Institute for Problems of Laser and Information Technologies of the Russian Academy of Sciences, to be applied for welding, cutting, surface treatment, stereolithography and laser diagnostics are briefly described.

**Key words:** *technological lasers, laser treatment of materials, laser cutting, laser welding, laser surface modification, laser stereolithography*

The Institute for Problems of Laser and Information Technologies of the Russian Academy of Sciences is working on fundamental and applied problems for development of laser and information technologies [1, 2]. It is one of the leading institutions of Russia in the field of development of high-power technological lasers, equipment on their base and laser technologies for materials treatment (welding, cutting, surface modification, stereolithography). The Institute is located in Shatura and has a division in Troitsk of the Moscow District. It has a staff of 350 people. The Institute has close scientific contacts and performs collaborative research with leading universities, research centres and companies of Russia, Ukraine, Belarus, USA, Japan, Germany, Great Britain, Poland, Bulgaria, Greece, Italy, India and China.

The Institute arranges and regularly holds an international conference «Industrial Lasers and Laser Applications» (ILLA), which gathers about 200–300 participants who make up to 150 presentations. The focus of the conference is on the latest developments in the field of technological lasers and laser treatment of materials. The conference proceedings are published in the form of special books «Proceedings SPIE» (issue 2257 is dedicated to ILLA'93, issue 2713 — to ILLA'95, 3688 — to ILLA'98 and 4644 (7th in series) — to ILLA'2001). Special issue 4165 «Progress in R&D of High-Power Industrial CO<sub>2</sub>-Lasers: Selected Papers», published in 2000, describes the latest developments made by the Institute, as well as other Russian and foreign research centres in the field of technological lasers and laser treatment of materials.

**Main fields of activity of the Institute. I. Technological lasers, laser-computer systems and technologies for materials treatment:**

- development and manufacture of technological 0.5–15 kW CO<sub>2</sub>-lasers with a high optical quality of radiation;

- technologies for laser treatment of materials and computerised technological laser systems for cutting, welding and surface modification.

## *II. Laser information technologies:*

- fundamental research in the field of development of basic elements and materials for multiwave optical information networks;

- methods and smart laser systems for synthesis of 3D objects of a complex topology from computer models and tomography data, including laser stereolithography systems;

- methods and systems of adaptive optics for solving problems associated with control of technological materials treatment processes.

## *III. Application of lasers in biomedicine:*

- laser systems for myocardial revascularisation, biocompatible coatings for stomatology and orthopaedy, controlled modification of the shape of cartilaginous tissue;

- optical-information methods of investigation of biological objects;

- fibre-optic waveguides and instruments for laser therapy and biomedical optics.

This article gives information about new developments and results obtained by the Institute in field *I* and partially in field *II* (stereolithography).

**Technological lasers and systems for precision cutting of sheet materials.** The Institute for Problems of Laser and Information Technologies is active in development [1–4] and manufacture of industrial technological CO<sub>2</sub>-lasers with a power of 0.5–10 kW, as well as laser systems for cutting, welding and surface treatment of metallic and non-metallic materials. The available production facilities of the Institute, which include modern optical production, allowed it, as well as a number of small enterprises established on its base, to produce more than 150 technological lasers and technological laser systems, which are now in operation in Russia and in a number of foreign countries, such as India, Czechia, China, Korea, Cuba and Yugoslavia.

**Table 1.** Main technical characteristics of the produced lasers

Model	Maximum power, kW	Aperture, mm	Divergence, mrad	Power consumption, kW	Weight, kg
10215 (TL-1.5)	1.5	19	1.4	24	1000
10430 (TL-2.5)	2.5	Up to 28	1.5	26	1000
10260 (TL-6)	6	30	1.5	70	2000

Main technical characteristics of the produced technological lasers used in laser cutting systems are given in Table 1.

These lasers are characterised by the presence of a modern control system, complete unification of assemblies and components and the possibility of operating in a crucibleless mode. Some models of high-power technological CO<sub>2</sub>-lasers are shown in Figures 1 and 2.

Specifications of laying-out tables used in the laser cutting systems are given below:

Maximum working zone, mm	
along axis X	up to 2000
along axis Y	up to 3000
Maximum travel speed, m/min	
along axes X and Y	20
Rated travel speed, m/min	
along axes X and Y	0.1–15.0
Accuracy of positioning, mm	
along axes X and Y	0.1
Voltage, V	380/220
Power consumption, kW,	
not more than	2

The above laser equipment provides cutting of metallic (up to 15 mm thick) and non-metallic (up to 60 mm thick) materials. Figure 3 shows appearance of a technological laser cutting system which uses the 1.5 kW laser of model 10215.

The work is now underway on building of high-efficiency modern laser systems for commercial cutting of sheet metal materials. The Institute, in collaboration with the Open Joint Stock Companies «NIAT» and «SAVMA» (V.A. Karasyov,

G.F. Smotrisky, V.V. Blinkov, A.V. Shcheglov, I.V. Volkov), is completing development and manufacture of a high-speed laser system intended for precision cutting of metal sheets measuring up to 1500x3000 mm and up to 10 mm thick. The system comprises a machine tool with units for three-axis displacement of the laser head, device for automated displacement of the table with a billet, technological laser with systems for transportation of radiation, gas feeding and cooling of optical-mechanical units, machine tool guard rail cabin, devices for removal of waste and cooling unit. The modern control system based on a high-capacity automatic high-technology CNC device of the «Power Automation PA 8000 NT CNC-Series» Company and a drive of the «Indramat» Company are used to increase productivity and improve quality of cutting. The system can be used to manufacture parts for automotive, aerospace, shipbuilding and electric engineering industries, as well as at enterprises of the defence and mining industries for cutting flat billets of structural, tool, stainless, silicon, spring steels and their alloys.

**Laser cutting of structural materials.** The Institute carries out experimental and numerical investigations into fundamental mechanisms of gas-laser cutting [5–7], as well as development of specific technologies for cutting various structural materials. The purpose of these efforts is to provide high-efficiency and optimal cutting processes with a high technological quality for different materials and cut profiles of high practical importance. Figure 4 shows an example of experimental measurements of temperature of a sample after cutting (associated gas — O<sub>2</sub>, O<sub>2</sub>/N<sub>2</sub>,


**Figure 1.** Industrial technological CO<sub>2</sub>-laser TL-1.5

**Figure 2.** Industrial technological CO<sub>2</sub>-laser TL-6

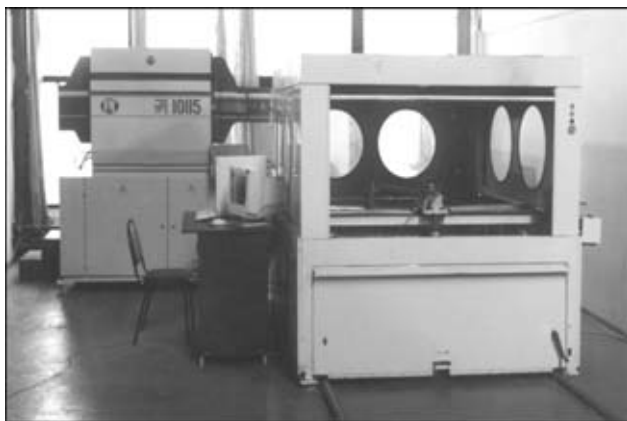


**Figure 3.** System for precision laser cutting developed and manufactured by the Institute for Problems of Laser and Information Technologies

$N_2$ ) with the fixed length of a cut profile, which allows the balance of energies of the process to be refined and cutting conditions to be optimised [6]. Table 2 gives experimental data obtained by V.A. Karasyov on cutting parameters for low-carbon and stainless steels using laser systems available at the Institute. Results of the investigations conducted are applied to fulfil orders on cutting sheet structural materials for manufacture of specific pieces, such as armour shields, safes, doors, cabins, disk saws, medical instruments, car body parts and research equipment (e.g. steel plates for collider CERN).

**Laser cutting of advanced materials.** Many projects of the XXI century associated with power generation, exploration of space and making of new tools require processing of advanced materials. The Institute for Problems of Laser and Information Technologies, in cooperation with the Institute of Metallurgy and Materials Science of the Russian Academy of Sciences (Prof. L.I. Ivanov), is active in investigation of capabilities and parameters of laser cutting of the above materials, using the up to 1.5 kW  $CO_2$ -lasers generating radiation in continuous and pulse-periodic (up to 3 kHz) modes with a high optical quality of the laser beam [7]. The results of the efforts include investigation of cutting parameters for the following

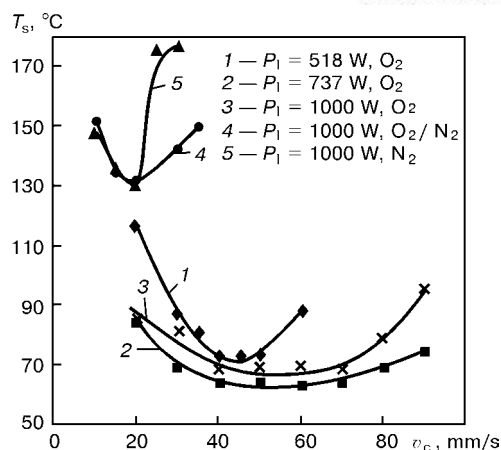


**Figure 4.** Dependence of temperature of samples,  $T_s$ , after cutting upon speed  $v_c$  (cutting gas pressure — 50 kPa)

materials: metals (e.g. Cr–Mn-alloyed steels), graphite, ceramic (boron nitride and heat-insulating high-temperature special ceramics) and a number of minerals. The cut depth is up to 20 mm, and the cutting speed is up to 6 m/min. Optimal values of the following main process parameters were established: laser power, pulse repetition frequency, feed speed, lens focal distance, focus deepening, type and pressure of an auxiliary gas, and geometrical parameters of the gas-dynamic system for gas feeding. The investigations proved the feasibility and showed real capabilities of laser cutting of a number of hard-to-treat advanced materials with a high quality and productivity of the process.

#### Promising areas of application of laser welding.

The high concentration of energy of radiation of the high-power (from 2 to 10 kW)  $CO_2$ -lasers enables welding of metals from 0.1 to 10 mm thick at a speed of 2 to 30 m/min. The basic advantage of laser welding is not just a high speed of the process, but also elimination of residual strains and ensuring high values of mechanical properties and operational strength. The Institute mastered the technology for laser welding of transmission gears (Figure 5), stainless pipes, hydraulic tappets of fuel equipment, cardan shafts, spray cans and fuel filter casings. The work is in

**Table 2.** Experimental data on cutting parameters for low-carbon and stainless steels

Material	Thickness, mm	Cutting speed, mm/s	Laser power, W	Cutting gas pressure, kPa
Zn-plated steel	0.3	50	450	300–400
	0.7	50	700	300–400
Cold-rolled steel	1.0	50–100	450–500	300–400
	2.0	60	680	300–400
Steel 3	3.0	30–40	700–720	200–300
	10.0	10	1300	50
Steel 10	5.0	20	900	150–250
	6.5	15	1100	200
Armour steel 40KhNMS	1.0	30	650	300–400
	3.0	25	810	200–300
Stainless steel 304SS	5.0	15	900	1.5



**Figure 5.** Appearance of the VAZ car gear ( $D = 80$  mm) welded using the TK-2.5 laser (welding speed — 2 m/min, focal distance — 150 mm, material — steel 18KhGT and 12Kh2N4A)

progress on the technology for laser welding of gas and oil pipelines [8], parts of aluminium alloys for aircraft engineering, and casing parts of titanium and high-strength steels for defence industry [9]. As an example, consider parameters of some of the welding processes:

- high-speed laser welding of thick-walled stainless steel pipes. This process was developed for welding of pipes with a diameter of 40 mm and wall thickness of 5 mm at a speed of 15 m/min using the TL-5M laser. It found application at Moscow and Dnepropetrovsk pipe manufacturing plants;
- laser welding of diamond abrasive bearing saw teeth for sawing of stones. The process is performed on saws 3–10 mm thick using the TL-5M laser (5 kW);
- high-speed laser welding of cans with a wall thickness of 0.15–0.25 mm at a speed of 30 m/min using the TL-5M laser (5 kW);
- laser welding of main gas and oil pipelines with a wall thickness of 10–15 mm at a speed of 3 m/min using the TL-10 laser (10 kW).

In development of the technologies for laser welding of pipes, the Institute cooperates with the PWI [8] in an area of investigation of performance of welded joints.

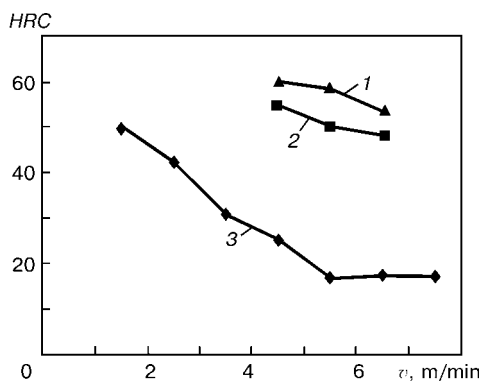


**Figure 6.** Hardness of steel WLC as a function of speed of heat treatment: 1 — hardening from 1040 °C; 2 — hardening from 1040 °C + tempering at 560 °C; 3 — without heat treatment (laser power — 3 kW)

The Institute is involved also in theoretical research [10, 11] to study mechanisms of hydrodynamic instabilities of the melt in deep penetration of the intensive laser beam into metal during the laser welding process.

#### **Application of laser technology for improvement of quality of working surfaces of die tools.**

The Institute is working under the European Program «EUREKA» to perform Project «GEFEST» intended for development and application of the technologies for laser and plasma cladding of working surfaces of die tools. Participating in the Project are the Institute for Metals Treatment and Technical University (Poland), Institute for Problems of Laser and Information Technologies of the Russian Academy of Sciences, N.E. Bauman Moscow State Technical University (Russia) and the PWI (Ukraine) and Metallurgical Works (Poland). The initial results obtained so far include development of the technology for laser modification of surfaces (hardening, alloying) of die tools for the manufacture of parts for automotive industry [12].

The methods were selected and developed for laser treatment of surfaces using the high-power technological CO<sub>2</sub>-laser MTL-2.5 with a mean radiation power of 3 kW and a specialised five-axis manipulator of the VISIP 125-A type.

Samples of dies after laser hardening and laser alloying were examined by metallography.

As proved by the investigations conducted, laser surfacing of worn-out parts can be replaced by laser alloying with refractory and super-hard elements of the type of finely dispersed boron.

Laser hardening of samples of die tools exhibited high adaptability for industrial application. Hardness of the treated layer (not less than 0.5 mm thick) amounts to HRC 60 (Figure 6), which is required for operation of the dies. Such hardness was produced both by laser hardening alone and by laser hardening performed after preliminary heat treatment of parts.

Based on temperature parameters and character of impact loads under conditions of operation of die tools, it is recommended to use preliminary hardening of parts at  $T_{\text{hard}} = 1040$  °C, followed by tempering at  $T_{\text{temp}} = 650$  °C, in combination with laser treatment at a radiation power of about 2 kW and treatment speed of 1.6 m/min.

Rig tests of the treated samples at the Institute for Metals Treatment (Poland) yielded positive results.

The data obtained laid the basis for working out principles of development of specific technologies for laser hardening and alloying of die tools for automotive industry.

#### **Laser stereolithography — new high-efficiency technology for acceleration of the production cycle.**

Achievement of a high qualitative level of new developments and a fast response to the current demand require rapid changes in the range of products and,

hence, maximum possible acceleration of the process of design of new products and corresponding fixtures, as well as manufacture of experimental samples and prototypes. These problems can be solved by one of the technologies of rapid prototyping, i.e. stereolithography. This type of the technology is being intensively developed at the Institute for Problems of Laser and Information Technologies, which has become the Russian leader in the field [13]. The technology allows production of plastic copies of 3D computer models of almost any degree of complexity with dimensions of several tens of metres within 24 hours, the accuracy of manufacture being not worse than 0.1 mm.

In other words, laser stereolithography is the laser-information technology for rapid manufacture of 3D objects of a complex topology, based on the data generated with the computer technology ACAD, for application in automotive industry, aerospace engineering, power generation, medicine, criminalistics and archaeology.

Laser stereolithography allows the route from a structural or art designer's idea to a finished model to be passed within a few days (Figure 7). The source data can be in the form of sketches and drawings, files, 3D objects, files of computer tomographs or coordinate-measurement machines, etc.

The Institute has developed and is producing the laser stereolithograph LS-250 (Figure 8). It is intended for layer-by-layer making of models, parts, assemblies and structures of any shape and complexity from liquid compositions which are polymerised under the effect of laser radiation. A 3D object designed on a computer is grown from a liquid photopolymerisable composition in successive thin layers formed under the effect of laser radiation on a mobile platform immersed into the bath with the liquid composition.

#### Specifications of the laser stereolithograph

Maximum dimensions of a part to be made, mm .....	250×250×250
Accuracy of manufacture, mm .....	±0.1
Power consumption, kW .....	2
Dimensions, mm .....	1700×1600×800
Weight, kg .....	300

The source data can be transmitted via Internet. Objects made with the LS-250 device can be used:

- as structural and art design prototypes;
- as consumable patterns or fixtures for various types of casting;
- as master-models for manufacture of electrodes utilised for electroerosion treatment;
- for manufacture of objects by the data of computer tomographs and coordinate-measurement machines, and other types of probing of 3D objects.

The Institute is also active in development of the technology for laser micro-stereolithography, which has already enabled production of objects a few micrometres in size (A.V. Evseev). The technology for

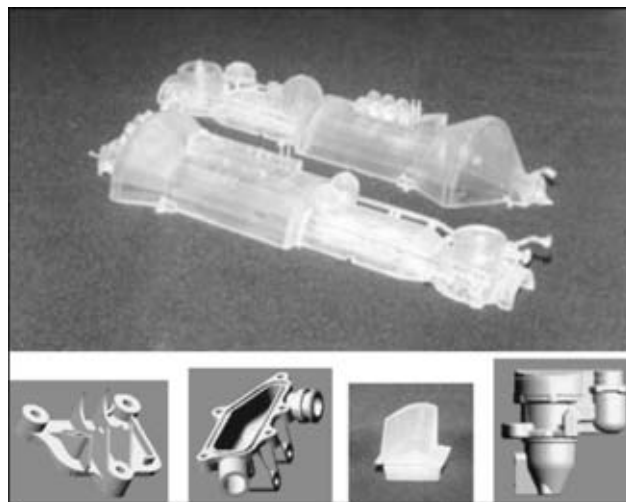


Figure 7. Photopolymeric models grown by the method of laser stereolithography

rapid manufacture of functional parts and fixtures is being developed using laser stereolithography and videogrammetry (V.P. Yakunin). This technology is based on the equipment developed and built by the Institute for the rapid manufacture of parts, fixtures or their copies from photopolymerisable compositions. The possibility exists of making functional parts and fixtures by casting using consumable or lost patterns.

**Laser diagnostics of subsurface defects.** Contactless non-destructive testing methods show promise for solving problems in both machine building and «smart» laser technologies. Thermal-wave microscopy is topical and one of the most important methods of non-destructive testing.

The principle of «thermal-wave microscopy based on a running beam» is in synchronised surface scan-



Figure 8. Laser stereolithograph LS-250

ning of the heat beam spot (in the form of a strip) and the range of sensitivity of a linear IR receiver. The speed of scanning should be comparable with the velocity of a heat wave for the thermal field to be efficiently registered. At present this method shows the highest promise in photothermal microscopy. It provides a high-contrast imaging of heterogeneities with a high efficiency of monitoring [14].

Another contactless method of non-destructive testing, i.e. laser opto-thermoacoustic diagnostics, is based on a stimulated laser excitation of surface acoustic waves and fixation of the thermal response which accompanies dilatation of the acoustic wave [15, 16]. The method provides the possibility of investigating anisotropy of elastic characteristics of a material by analysing angular dependence of the velocity of propagation of the surface acoustic wave, which allows defects of the type of vertical cracks to be detected. The method is particularly convenient for testing samples under increased temperature conditions.

1. Web-site: <http://iplit.laser.ru>
2. Panchenko, V.Ya., Golubev, V.S. (2000) Applications of lasers in machine building and metallurgy. In: *Proc. SPIE*, Vol. 4165.
3. Golubev, V.S. (1996) Research of some new ways to improve the efficiency and optical quality of industrial CO<sub>2</sub>-lasers. In: *Gas lasers — recent developments and future prospects*. Ed. by W.J. Witteman, V.N. Ochkin. Dordrecht: Kluwer A.P.
4. Vasiltssov, V.V., Zabelin, A.M. (2000) High power CO<sub>2</sub>-lasers for material processing. In: *Proc. SPIE*, Vol. 4165.
5. Ledenev, V.I., Karasyov, V.A., Yakunin, V.P. (1999) On capillary phenomenon during melt removal under gas assisted laser cutting. *Ibid.*, Vol. 3688.
6. Bazyleva, I.O., Galushkin, M.G., Golubev, V.S. et al. (2001) Thermal losses in process of gas assisted laser cutting metals. *Ibid.*, Vol. 4644.
7. Dubrov, V.D., Panchenko, V.Ya., Golubev, V.S. (2001) Laser cutting and welding of unspecified materials. In: *Proc. of Int. Conf. on Program on Advanced Laser Technologies*, Constanta, Romania, Sept. 11–24, 2001.
8. Rybakov, A.A., Yakubovsky, V.V., Kirian, V.I. et al. (1995) Investigation of operational integrity of 10G2BT pipe steel welded joints performed by two-pass laser welding. *Avtomatich. Svarka*, **7**, 12–17.
9. Kajtanov, A.Yu., Ozersky, A.D., Zabelin, S.M. et al. (2001) Static and fatigue strenghts of laser welded overlap joints with controlled penetration. In: *Proc. SPIE*, Vol. 4644.
10. Golubev, V.S. (2000) Possible hydrodynamic phenomena in deep penetration laser channels. *Ibid.*, Vol. 4165.
11. Golubev, V.S., Mirzoev, F.Kh., Shiganov, I.N. (2001) Hydrodynamical model of melt components stratification during scanning laser beams interaction with heterogeneous materials. *Ibid.*, Vol. 4644.
12. Panchenko, V.Ya., Vasiltssov, V.V., Golubev, V.S. et al. (2001) Application of laser technology in quality improvement of stamping tool working surfaces. *Ibid.*
13. Antonov, A.N., Evseev, A.V., Kamaev, S.V. et al. (1998) Laser stereolithography — the technology of layer-by-layer manufacturing of 3D objects from liquid photopolymerizable compositions. *Opticheskaya Tekhnika*, **1**, 5–14.
14. Karabutov, A.A., Kubyshkin, A.P. (1994) Laser thermal-wave microscopy for remote nondestructive testing. In: *Proc. SPIE*, Vol. 2257.
15. Karabutov, A.A., Kubyshkin, A.P., Savateeva, E.V. (1995) Novel noncontact method of surface acoustic wave registration for nondestructive testing. *Ibid.*, Vol. 2713.
16. Kubyshkin, A.P., Paul, M., Arnold, W. (1999) Detection of laser generated Rayleigh waves by recording their IR radiation. *Ibid.*, Vol. 3688.



# WEAR RESISTANCE OF DEPOSITED METAL OF Fe-C-Cr-Ti-Mo ALLOYING SYSTEM

I.A. RYABTSEV, I.A. KONDRATIEV, V.G. VASILIEV and L.K. DOROSHENKO

The E.O. Paton Electric Welding Institute, NASU, Kyiv, Ukraine

Resistance of deposited metal of type of high-carbon Cr-Ti-Mo steel under the conditions of abrasive wear was studied. High wear resistance of deposited metal of this type is explained by the ability of austenitic-martensitic matrix of alloy to prevent the chipping of titanium carbides at the expense of formation of coherent bonds at the austenite-carbide interface. Optimum composition of deposited metal was selected and self-shielding flux-cored wire was developed on the basis of results of investigations.

**Key words:** *deposited metal, wear resistance, dilatometric analysis, self-shielding flux-cored wire*

Abrasive wear resistance of deposited metal of type of high-alloyed steels and alloys is determined mainly by a structural state and degree of alloying of a base as well as by a number and composition of a carbide phase. In addition, with increase in hardness of a carbide constituent a total wear resistance is usually increased.

Titanium belongs to strong carbide-forming elements, and its carbide of TiC type is one of most hard and refractory materials. Besides, the cost of ferro-titanium used in charge of surfacing flux-cored wire and strips is much lower than the cost of ferroalloys of other strong carbide-forming elements (vanadium, niobium, tungsten). Therefore, the use of titanium as one of main alloying elements in highly wear-resistant surfacing materials is rather challenging.

The aim of the present work is to determine the optimum composition of the deposited metal, being resistant under the abrasive wear conditions; investigation of structure of deposited metal depending on thermal cycles of a multilayer surfacing; development of composition of flux-cored wire and technology of electric arc surfacing, providing the maximum assimilation of titanium characterized by a strong affinity to oxygen and ability to burn out significantly in electric arc surfacing.

For investigations the deposited metal of Fe-C-Cr-Ti-Mo system of alloying was selected, in which the role of main carbide-forming element was played by titanium, while chromium and molybdenum were added mainly for the matrix strengthening. Coming from the existing experience and capabilities of manufacture of the flux-cored wire [1] the mass fraction of chromium in the deposited metal was limited to 6 % and molybdenum to 1 %. Carbon content varied in the range of 1.5–2.5 and titanium — 2–8 wt.%. Investigation of wear resistance and selection of optimum composition of the deposited metal were performed on model alloys (Table) melted in a vacuum induction furnace.

Taking into account that surfacing, as a rule, is performed in many layers and the metal of the previous bead undergoes thermal effect from the subsequent layer due to repeated heating to different temperatures, the wear resistance and hardness of selected alloys were evaluated after the heat treatment. Heat treatment consisted of heating samples up to 850–1100 °C and cooling by their air blowing. Cooling rate of the samples corresponded approximately to the cooling rate of components after surfacing.

Wear resistance of selected alloys was evaluated in friction of samples along the abrasive paper in test machine IZA-3 [2]. Two samples were tested simultaneously, i.e. experimental and reference sample

Chemical composition of investigated alloys

Alloy	Elements, wt. % <sup>*</sup>					
	C	Mn	Si	Cr	Ti	Mo
150Kh6T4M	1.6	1.0	0.5	6.0	4.5	1.2
200Kh6T4M	2.1	0.4	0.3	5.9	3.9	0.9
250Kh6T2M	2.8	0.5	0.4	5.8	2.5	1.0
250Kh6T4M	2.5	0.5	0.4	6.0	4.2	1.0
250Kh6T8M	2.4	0.4	0.5	5.8	8.5	0.8

<sup>\*</sup>The rest — iron.

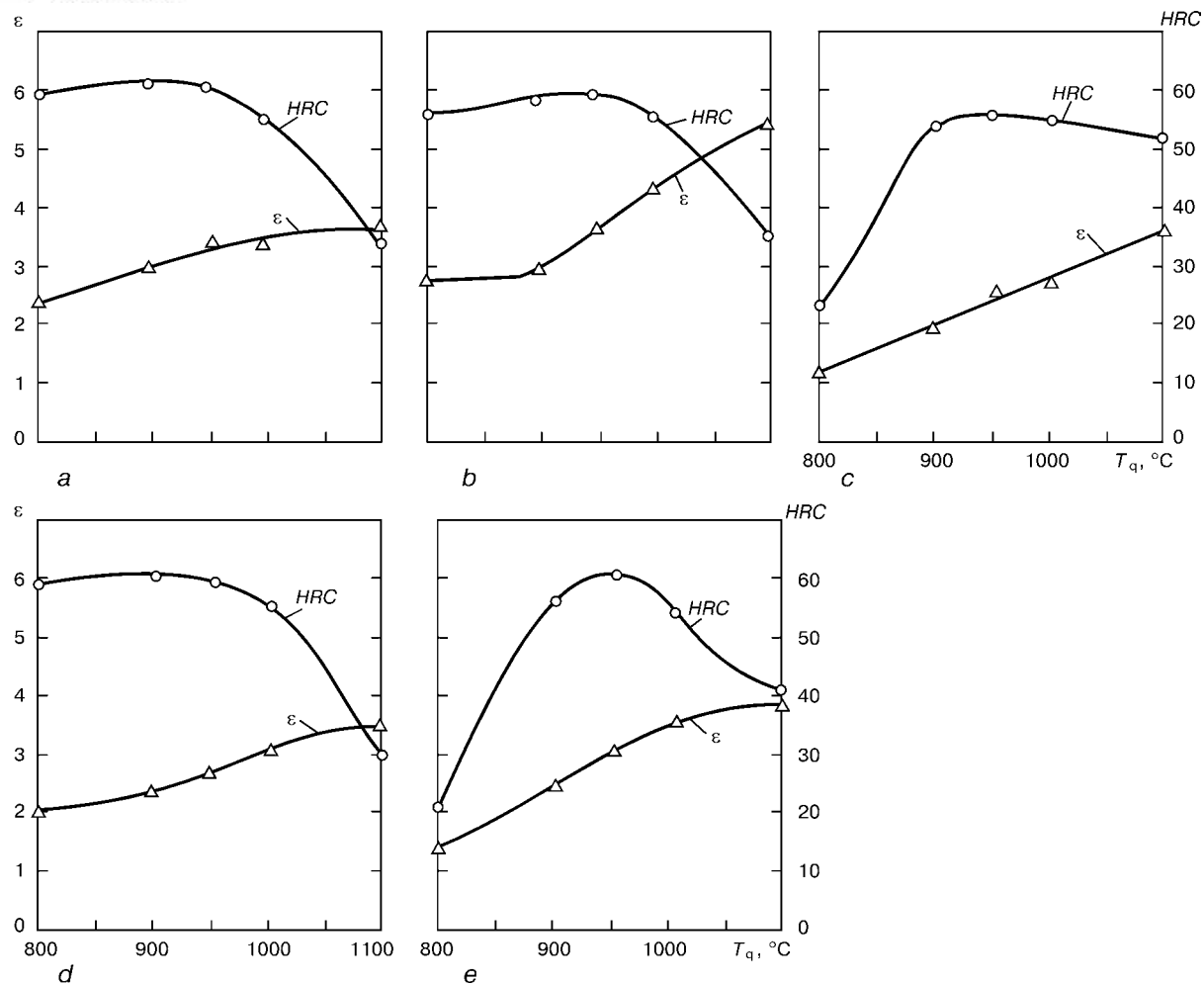


**Figure 1.** Relative wear resistance  $\epsilon$  and hardness HRC of Cr-Ti-Mo alloys 250Kh6T2M (a), 250Kh6T4M (b), 250Kh6T8M (c), 200Kh6T4M (d) and 150Kh6T4M (e) depending on temperature of quenching  $T_q$

from annealed steel 45. Test results were expressed in the form of a relative wear resistance equal to ratio of loss of reference sample mass to the loss of test sample mass.

Relationships between the relative wear resistance and hardness and temperature of heat treatment are given in Figure 1. It follows from Figure that metal should contain, wt.%: C — 1.5–2.5; Ti — 3.5–5.0; Cr — 5.0–7.0; Mo — 0.8–1.2, to explain the high resistance under the conditions of abrasive wear. After heating within the wide range of temperatures the high wear resistance of this metal is preserved that is very important in multilayer surfacing.

A self-shielding flux-cored wire was developed to produce the deposited metal of the above-mentioned composition. Taking into account the high degree of alloying of deposited metal it was necessary to select the composition of gas-slag-forming part (minimum mass) of charge of the flux-cored wire. System of rutile-fluorite type was taken as a basis and nepheline concentrate was used to stabilize the arc burning and to decrease spattering. Experiments resulted in the development of the new composition of a gas-slag-forming part of charge of the self-shielding flux-cored wire whose total mass did not exceed 4 %. This made it possible to manufacture the self-shielding flux-

cored wire PP-Np-150Kh6T4M of diameter from 2.0 to 2.8 mm. The wire is characterized by good welding-technological properties, assimilation of titanium in surfacing is amounted to 70–75 %.

To study the structural transformations in the deposited metal of 150Kh6T4M in the process of single- and multilayer arc surfacing the dilatometric examinations were performed. Samples for this examination were cut from the fourth layer of the multilayer deposited metal.

Firstly, the transformations in the deposited metal were studied by simulating a single bead. Samples were heated to 1200 °C at 150 °C/s rate, cooling — at 20 °C/s rate, close to a real surfacing. Samples were soaked at 1200 °C for 1 min to increase the degree of dissolution of carbides. Estimated temperature of cooling samples was 200 °C, while real temperature was (180±10) °C.

The increase in length on heating curve in the range of 350–650 °C temperature was observed, this area corresponded to the transformation of residual austenite (Figure 2). Above the 650 °C temperature the length of sample is decreased that corresponds to completion of transformation of residual austenite and beginning of carbide transformation. Temperature of end of the carbide transformation is 780–820 °C.

Transformation  $\alpha \rightarrow \gamma$  occurs at temperatures 855–870 ( $A_{c1}$  — beginning of transformation) and 970–975 °C ( $A_{c3}$  — end of transformation). At further rise of temperature and increase in time of soaking the carbides are dissolved in the formed austenite.

During cooling the austenite decay was not observed. It is not also occurred after soaking of samples for 6 h at 180 °C, simulating preheating and auxiliary heating (autopreheating) in the process of long multilayer surfacing. The subsequent delayed cooling for 30 min leads to the formation of martensite ( $M_b = 170$  °C). Transformation is not finished completely in cooling to room temperature and it is continued in isothermal conditions. After soaking for 12 h the martensite content in the deposited metal increases proportionally to length  $K_1 K_2$  (Figure 2). This proves that a large amount of residual austenite is preserved in the structure of the deposited metal.

Dilatometric investigations of samples were also made by heating samples at temperatures 800–1050 °C and, thus, simulating structural transformations in the deposited metal 150Kh6T4M in the process of multilayer surfacing (Figure 3). Then, without soaking they were cooled at the 20 °C/s rate. Figure 3 shows only the curves of cooling, as the curves of heating in all the cases were similar to that of Figure 2.

In cooling from temperatures 1050, 990, 920 °C (Figure 3, curves 1–3) to the point of beginning of martensitic transformation no bends in curves of cooling were observed. Inclination of curves is similar to that of curve of cooling samples corresponding to surfacing of a single bead (Figures 2 and 3, curve 4). Reaching the martensite point (for each temperature of heating it is different) the part of austenite is transformed into martensite. However, the same as in case of surfacing of a single beat this austenite is rather stable after cooling to room temperature its amount in the structure of the deposited metal remains high.

At heating to 800 °C, i.e. to the temperature below the critical point  $A_{c1}$ , the nature of cooling curve is differed by a smaller inclination and more high temperature of beginning the martensite transformation (Figure 3, curve 5) than in three previous cases. Thus, the content of martensite (tempered) should increase in HAZ heated to the temperature below  $A_{c1}$ .

The examination of microstructure of deposited metal of 150Kh6T4M type confirmed the data of dilatometry (Figure 4). The sections show areas of residual austenite inside of which martensitic needles are located, a large amount of carbonitrides of titanium of different geometric shape are observed over the entire area of the section.

#### Hardness of samples, HRC

Deposited metal (center of first bead) .....	52
Simulation of first bead (heating to 1200 °C) .....	57
Simulation of HAZ (heating to 1050 °C) .....	61
The same (heating to 990 °C) .....	59
» (heating to 920 °C) .....	61
» (heating to 800 °C) .....	51

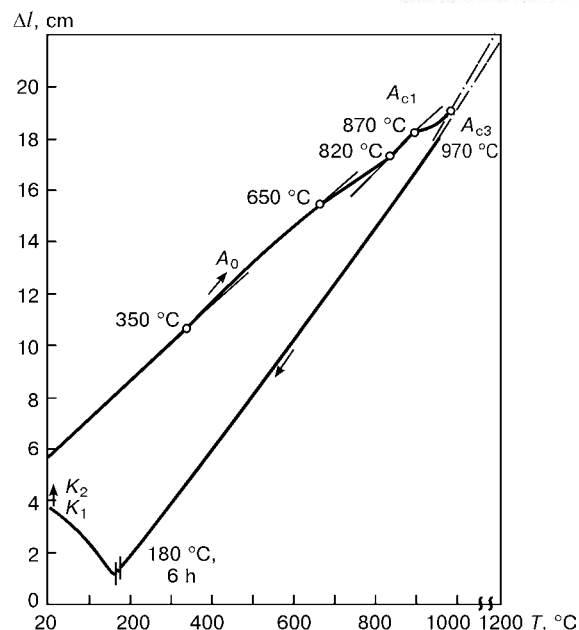


Figure 2. Dilatometric curve in heating and cooling of deposited metal 150Kh6T4M ( $\Delta l$  — indications in dilatometer scale)

The mentioned temperatures cover the range of temperatures of heating areas of lower (neighboring) bead which undergo thermal effect in surfacing of a subsequent bead. Negligible change in hardness makes it possible to state that the wear of components deposited by a self-shielding wire PP-Np-150Kh6T4M will have a uniform nature.

Assumption was made that the high wear resistance of austenitic-carbide structure of the deposited metal of 150Kh6T4M type is explained by establishment of strong bonds at the carbide–austenite interface in the process of alloy crystallization. Titanium carbide and austenite have a similar type of a crystalline lattice (fcc). Data of X-ray structural analysis show that in some crystallographic directions

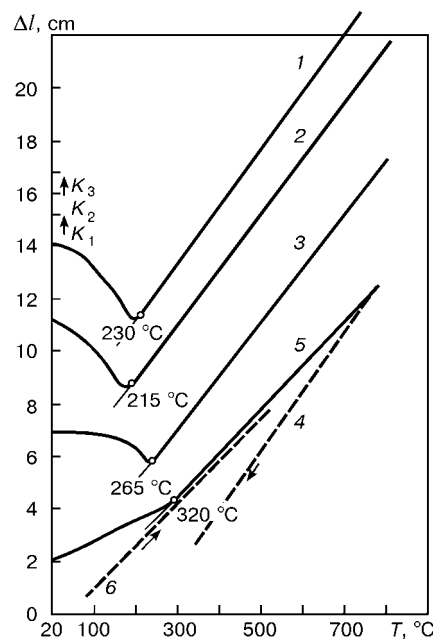
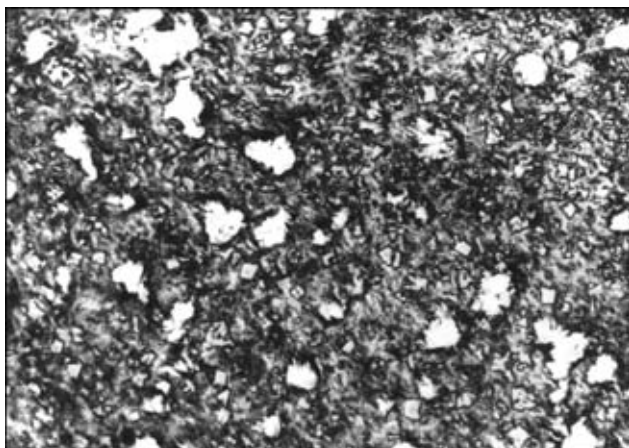


Figure 3. Dilatometric curves in cooling deposited metal 150Kh6T4M at different temperatures (for designations see the text)



**Figure 4.** Microstructure of deposited metal 150Kh6T4M (x800) (reduced by 3/4)

the oriented conformity between crystalline lattices of titanium carbide and austenite was observed:

$$(001)\text{TiC} \parallel (110) \gamma\text{-Fe}, <001>\text{TiC} \parallel <110> \gamma\text{-Fe}.$$

In this case the formation of a strong mating of crystalline lattices, i.e. establishment of a coherent bond is possible at the austenite–carbide interface [3]. Real particles of titanium carbides are not monocrystalline, therefore, the strong mating occurs only at separate regions of their surfaces where orientation of carbide grains of titanium and austenite is favourable.

Formation of strong bonds at the titanium carbide–austenite interface is already possible at the stage of the weld pool crystallization. Titanium carbides which have higher melting temperature than that of iron are the primary centers of crystallization in solidification. Solidification of matrix melt will proceed near these centres with the formation of coherent bonds in places of a favourable crystallographic orientation of grains.

Indirect confirmation of this assumption is the results of thermal analysis of deposited metal 150Kh6T4M in unit VDTA-8M at 80 °C/min rate of heating and cooling. Two bends at temperatures 750 and 880 °C were observed on a thermal curve at the branch of heating in a solid state (Figure 5, curve 1). First of them corresponds to Curie point, while the second — to transition  $\alpha \rightarrow \gamma$ , probably. Temperature of beginning of melting is 1370 °C and 1470 °C at the end of melting.

Two peaks are seen in curve of cooling (Figure 5, curve 2) that proves about the complex nature of

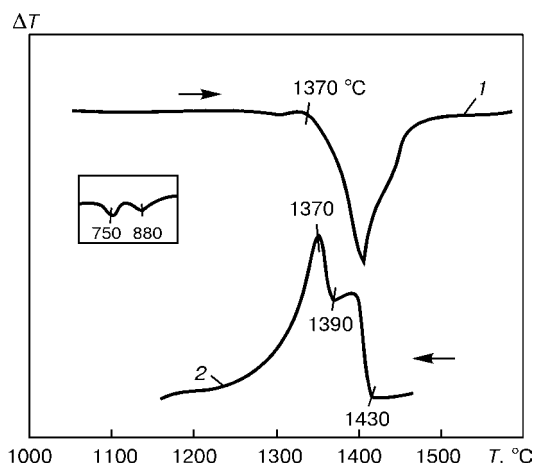


**Figure 5.** Differential thermal curves in heating (1) and cooling (2) of deposited metal 150Kh6T4M

crystallization. High-temperature constituent ( $T \geq 1430$  °C) can be probably associated with the formation of centers of crystallization in the form of carbides. The second peak of crystallization at temperature  $T \leq 1390$  °C is associated with the formation of  $\gamma$ -phase. In accordance with the generally accepted procedure the solidus point is selected on curve of heating ( $T_S = 1370$  °C), and the liquidus point — on curve of cooling ( $T_L = 1430$  °C). Thus, the fact of dividing crystallization peak, established as a result of investigations, corresponds to the crystallization of two different phases: first — carbide constituent, second — austenite matrix.

## CONCLUSIONS

1. Surfacing self-shielding flux-cored wire PP-Np-150Kh6T4M has been developed, which provides the metal characterized by high resistance under the conditions of abrasive wear.

2. Investigations showed that high wear resistance of the deposited metal of 150Kh6T4M type is explained by the ability of austenitic-martensitic matrix of alloy to prevent the chipping of titanium carbides at the expense of formation of coherent bonds at the austenite–carbide interface.

1. Ryabtsev, I.A., Kondratiev, I.A. (1999) *Mechanized electric arc surfacing of metallurgical equipment components*. Kyiv: Ekotekhnologiya.
2. Yuzvenko, Yu.A., Gavrish, V.A., Marienko, V.Yu. (1979) Laboratory units for evaluation of wear resistance of deposited metal. In: *Theoretical and technological bases of surfacing. Properties and tests of deposited metal*. Kyiv: PWI.
3. Palatnik, L.S., Papirov, I.I. (1964) *Oriented crystallization*. Moscow: Metallurgiya.



# REPAIRING DEFECTS IN THICK METAL USING THE TECHNOLOGY OF NARROW-GAP ARC WELDING

I.A. TARARYCHKIN<sup>1</sup> and A.N. TKACHENKO<sup>2</sup>

<sup>1</sup>East-Ukrainian National University, Lugansk, Ukraine

<sup>2</sup>Holding Company «Luganskteplovoyz», Lugansk, Ukraine

The paper gives the results of welding technologies application to repair a crack in the body of a large-sized structure. It is shown that the maximal effectiveness of the repair operations can be achieved when using the technology of narrow-gap arc welding.

**Key words:** arc welding, large thicknesses, narrow gap, defects, quality control

The attractiveness of repair operations for modern enterprises is primarily related to the ability of quickly achieving a real result at a minimal cost level. The highest repair effectiveness is achieved in the case of repairing defects of large-sized structures, having a considerable weight and thickness of metal. Welding technologies are widely applied in restoration of the performance of structures for various purposes [1–3].

This paper gives data on the use of narrow-gap arc welding technology in welding up a crack in the bottom of a cylinder of a forging hammer in «Luganskteplovoyz» enterprise.

By the results of external examination of the structure it was established that crack propagation into the part of the body was  $\approx 90$ –95 mm, its length being 490 mm (Figure 1). Part thickness in the plane of crack propagation was from 110 to 280 mm. A special feature of repair was a one-sided access to the site of work performance, because of the availability of the flange part. Under such conditions, making a one-sided V-shaped groove with groove angle  $\alpha = 60^\circ$  requires subsequent deposition of metal of more than

22 kg weight, and at  $\alpha = 30^\circ$  the deposited metal weight is about 11 kg.

One-sided deposition of a considerable volume of metal leads to development of angular deformation, the magnitude of which may be higher than  $10^\circ$ . Deformation of such a level on  $\approx 500$  mm arm (distance from the crack to the connector holes) may lead to distortions of up to 90 mm, which is unacceptable. The arising problems are also related to the need to provide the required quality of repair work, as the structure failure in service may lead to a grave accident.

The above problems can be effectively solved, using the technology of gas-shielded narrow-gap arc welding, that has the following advantages: minimum volume of the deposited metal, when filling the groove; low level of residual deformations of the structure; ability of automation of welding operations. This results in a high quality of the deposited metal making it potentially attractive, when repairing defects in thick metal. However, the capabilities of this method when applied for repair operations have not practically been studied.

In this case the technology of repair work included the following operations:

- milling out the crack along the entire length to a depth of 100 mm. The thus formed groove 12 mm wide was examined for surface cracks (dye penetrant method was used);

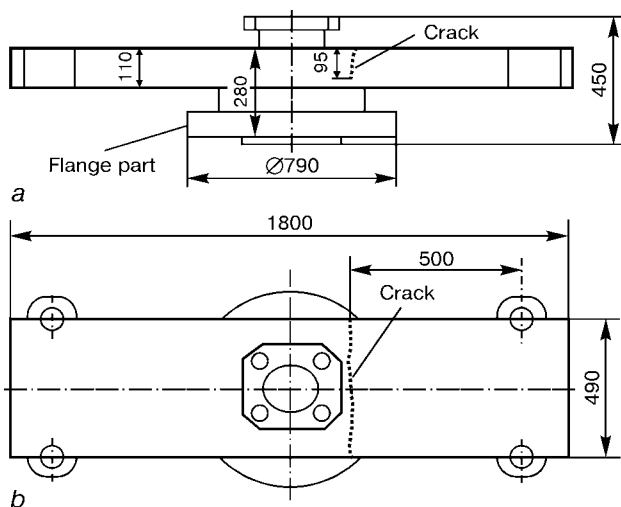


Figure 1. Sketch of cylinder bottom and crack location

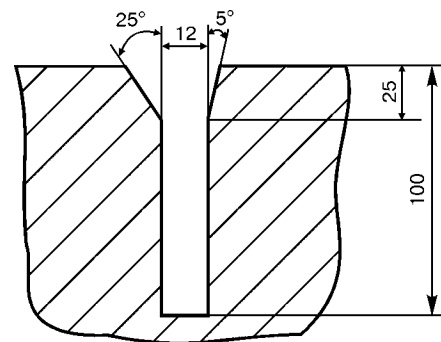
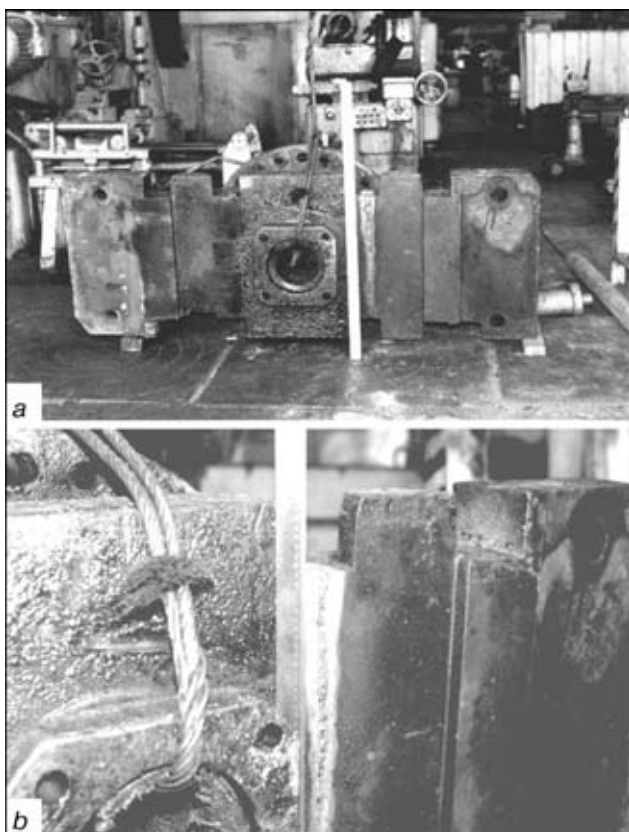


Figure 2. Schematic of groove propagation for welding



**Figure 3.** Appearance of repaired structure (a) and fragment of the restored section (b)

- widening of the groove at the surface (Figure 2) in view of a complex configuration of the plane of crack propagation;
- filling the lower rectangular part of the groove with the metal, using gas-shielded narrow-gap auto-

matic welding, and the upper part, using coated-electrode manual arc welding.

As welding of thick metal should be performed with preheating, when filling the main part of the groove, the welding zone was preheated with gas flame approximately up to the temperature of 150 °C. The groove upper part was filled in a cascade, when preheating methods are not required.

When filling the rectangular part of the groove, the welding operations quality was guaranteed, by using the method of plotting the charts of controlling the process condition [4]. Process monitoring and statistical regulation of the process were carried out by the position of the torch relative to the gap centre; change of the gap width because of development of angular and transverse deformations and by arc voltage.

Final control of the quality of welding operations was performed, using the ultrasonic testing methods. Figure 3 shows the appearance of the item and a fragment of the repaired section.

The obtained results turned out to be satisfactory on the whole, as the quality of the performed work corresponded to the requirements made, magnitude of distortions in the region of the connecting holes was 2–3 mm, this not requiring performance of the operations of subsequent straightening, while the deposited metal weight was  $\approx 5.5$  kg.

1. Semyonov, V.M., Gulida, V.P., Bratsun, I.T. et al. (1981) Examination of possibility of repair of large frames with cracks. *Avtomatich. Svarka*, **12**, 56–57.
2. Gutman, L.M., Balakanov, V.A., Tkachenko, O.P. (1993) Welding of cracks in automatic coupling body. *Ibid.*, **10**, 41–42.
3. Lozebnov, P.P. (1999) Repair by welding of cellulose sulfite digestion boiler. *Ibid.*, **1**, 54–56.
4. Tararychkin, I.A. (2001) Statistic regulation of welding technological processes using the method of construction of charts of condition control. *The Paton Welding J.*, **10**, 28–31.



# TECHNOLOGY FOR EXPLOSION HARDENING OF SUPPORT SURFACES OF AXLE BOXES

V.V. DRAGOBETSKY

Kremenchug State Polytechnic University, Kremenchug, Ukraine

Technology for hardening support surfaces of bodies of railway car axle boxes made from aluminium alloy Al-6.2Mg and high-strength cast iron is described. Technology parameters of explosion welding of steel to aluminium plates, as well as Hadfield steel plates to cast iron parts are given.

**Key words:** *axle box body, explosion welding, cladding, shock wave, support surface, parameters, process*

Progress in production of special profiles made by extrusion offered the possibility of manufacturing bodies of railway car axle boxes from aluminium alloys. An increased corrosion resistance of the latter allowed the costs of anti-corrosion treatment to be eliminated, the costs of repair due to corrosion to be reduced and weight of the running gear of cars to be decreased by 20–30 %. However, aluminium alloys lack anti-friction properties. Therefore, it is recommended to make surfaces of aluminium bodies of axle boxes in contact with steel surfaces of mating parts also from steel. The coating method based on explosion cladding has a number of advantages over other known methods for deposition of steel coatings on working surfaces of aluminium parts. For example, it provides a strong welded joint of metals over the entire surface of a part; the joint, being absolutely thermally unaffected, retains structural characteristics of clad metal; resulting coatings have an increased wear resistance, which is attributable to the processes of hardening of materials joined that occur in the contact zone (wear resistance increasing with distance from the contact zone deep into the coating).

The process of cladding of axle box bodies with wear-resistant steel plates, which is in commercial production now, is as follows. Bodies of railway car axle boxes are made from aluminium Al-6.2Mg alloy. Wear of the axle box lug during operation amounts to 30–40 mm (steel–aluminium alloy friction pair). To prevent wear, associates of the Research Institute for Railway Transport recommended to clad lugs of the axle box bodies with a 4–6 mm thick layer of carbon steel of grades 20, 25 and 30. Shear strength of the cladding layer should be within a range of 12–15 MPa. As the processes of spraying, surfacing and roll knurling fail to provide the desirable parameters of the cladding layer, investigations were conducted to study the process of explosion welding.

It is a known fact that aluminium and iron form a chemical compound in interaction. Metals of this group are hard to weld by any welding method, including explosion welding. This method can be realised within a very narrow range of collision parameters. Neverthe-

less, it has been already mastered and is widely applied in industry of our country and abroad [1].

In the case under consideration the application of explosion welding is hampered by a number of reasons. One of them is a small area of the mating surfaces. If the length of a lug is within the range of stable welding conditions, its width of 40 mm is insufficient. The axle box body comprises two lugs, the distance between which is 150 mm. An air shock wave passes this distance for  $\approx 4.5 \cdot 10^{-4}$  s. Therefore, in the case of cladding two lugs the detonation of two charges should be timed within  $(1.5-2.0) \cdot 10^{-4}$  s. In addition, shock wave loading is accompanied by deformation of the axle box body and propagation of wave disturbances through metal.

Allowing for all these factors, the problem of cladding lugs of axle box bodies with steel plates was solved by preliminarily cladding them with commercial aluminium of grades AD1, AD1-0 or D1. Thickness of the aluminium alloy layer was selected so that it provided minimum forcing out of metal at the edges and then minimum welding parameter  $r$ , i.e. ratio of mass of an explosive to mass of the plate welded. This practically excluded any lack of penetration at the edges. To eliminate lacks of penetration at the initial stage of the process, related to the absence of oblique collision and cleaning of the surfaces welded, the explosion welding process used involved flanging of the plate [1]. Bimetal steel-aluminium (2000×40×4 mm) was welded to the lugs of the axle box bodies. Welding conditions were selected on the basis of ensuring the required accuracy of a welded joint and minimum deformation of the lugs and the axle box body as a whole, i.e. values of the welding parameters were set at minimum —  $r = 0.6$  and collision velocity equal to 500–600 m·s<sup>-1</sup>.

No deformation was observed under dynamic loading of billets of the bodies produced by extrusion. However, this resulted in an elliptic form of inside openings of the treated billets. Therefore, it was necessary to use expanding mandrels for explosion cladding of finished items to prevent deformation of the body [2] and extinguishing of refracted and reflected shock waves, leading to decrease in strength of a welded joint or even to separation of the cladding layer. The following explosion welding parameters



Axle box body with steel plate welded to it

were established:  $r = 0.6$ ;  $h = 3d$  (here  $h$  is the welding gap and  $d$  is the plate thickness),  $D = 2200 \text{ m}\cdot\text{s}^{-1}$ ,  $H = 35 \text{ mm}$  (here  $D$  is the detonation velocity and  $H$  is the charge height).

The resulting welded joints were subjected to standard tensile and shear tests. Rupture of specimens cut from the entire surface of the weld occurred in a less strong material, this being indicative of a high quality of the welded joint. An experimental batch of bodies of axle boxes with lugs clad with steel plates was made and subjected to service tests. A sample with a plate welded to one of the lugs (for visualisation) is shown in the Figure.

In our opinion, direct explosion hardening of lugs of aluminium bodies either by explosion wave or by impact by a solid body accelerated by explosion is not less efficient. The process of hardening using a captive explosion charge (shock wave) is technically simpler and easy to realise. This provides a several times decrease in labour consumption of the process by eliminating the need of making bimetal steel-aluminium plates and their flanging, and avoiding operations associated with installation of distant elements and cladding plates. After the hardening operation, hardness of a lug through its entire thickness increases by 40–45 %, yield strength increases by 50 % and tensile strength — by 10–15 %, i.e. it is approximately equal to that of carbon steel 20.

Higher values of strength and hardness are achieved by hardening the lugs by impact by a solid body accelerated by explosion under the collision parameters which provide melting of the surface layer of the axle box body lug without formation of a welded joint. In particular, values of the collision parameters exceed the limits of explosion welding parameters (detonation velocity of an explosive is more than 1.3 times higher than velocity of sound which propagates in aluminium alloy), but are lower than values of the explosion hardening parameters. If the surfaces of the axle box body lugs are given a certain roughness which provides formation of opposing cumulative molten alloy Al-6.2Mg jets formed in collision with a flyer

plate, this will result in formation of a microlayer. Its microhardness corresponds to hardness of titanium alloys. Under such conditions the rate of cooling of the opposing cumulative jets amounts to one million degrees per second [1], which results in conditions for rapid solidification. However, labour consumption of this process is comparable with that of explosion welding processes. This is a reason why it failed to find application.

Although the processes under consideration provide approximately similar values of wear resistance, production people, probably mechanically or because of the established traditions, prefer to use the explosion cladding process. At the suggestion of German train car constructors, support surfaces of the axle box bodies made from high-strength cast iron were clad with Hadfield steel plates. As follows from [2, 3], this steel is considered unweldable and is not produced in the rolled form both in our and other CIS countries.

It is likely that in this case explosion welding is the only possibility to produce a permanent joint between high-manganese steel and cast iron. To prevent formation of cracks and separations in cast iron bodies of axle boxes, the explosion welding process was performed through a copper interlayer  $2\cdot 10^{-3} \text{ m}$  thick. This is associated with the fact that strength of copper meets service requirements under loading and it can be explosion welded to iron-carbon alloys within a very wide range of explosion loading parameters. Large experience has been accumulated in explosion welding of copper to cast iron. Copper was found to be characterised by high damping properties in collision of a cladding billet with a clad surface.

Preliminary explosion welding was carried out to join Hadfield steel plates  $240\times 40\times 4 \text{ mm}$  to copper. The resulting welded joints had adhesion strength of the layers in excess of tensile strength of copper, the welding parameters being as follows:  $r = 1$ ,  $D = 4000 \text{ m}\cdot\text{s}^{-1}$  and  $h = 3\cdot 10^{-3} \text{ m}$ .

Prior to direct cladding of the support surfaces of an axle box body, it was necessary to determine parameters of collision of the plates welded, at which no fracture of the support surfaces would occur and no cracks would be formed in the surface layer and in the bulk of the axle box body. In this case the additional difficulties were associated with the fact that the axle box body was made from a low-ductility material with low crack resistance and had four support surfaces, i.e. two vertical and two horizontal ones, located in pairs and mutually perpendicularly. Simultaneous explosion cladding of four support surfaces by a combination of the vertical and horizontal explosion welding methods led to fracture of the axle box body. In the case of simultaneous cladding of two support surfaces, we faced the problem that there occurred a loss of the non-detonated explosive and cladding plate at the initial stage of detonation. This is associated with the fact that the explosive is placed near the support surface which is normal to the surface



treated at the first stage. Interaction of shock waves propagating in the treated and non-treated support surfaces, as well as in the axle box body, prevented formation of a welded joint. To eliminate the effect of subsequent shock-wave disturbances, directed normal to the cladding layer, the use was made of an expanding mandrel that comprised laminated elements which extinguished the effect of the shock waves. The system of charges, the detonation of which localises loading in a direction normal to that of the flyer cladding plate, was used to eliminate the effect of shock-wave disturbances and the converging shock waves that are formed in plane of the cladding layer [4]. Thickness of the copper sublayer was estimated from a condition that stress formed in it in explosion cladding is not in excess of the dynamic tensile strength of the axle box body material and does not cause formation of cracks. That corresponded to a collision velocity of up to  $600 \text{ m}\cdot\text{s}^{-1}$ . Explosion welding of the stack of plates, i.e. high-manganese steel + copper, to the cast iron axle box body at collision velocities not in excess of the maximum permissible values takes place under the following parameters:  $r = 0.6$ ,  $h = 5 \cdot 10^{-3} \text{ m}$  and  $D = 4000 \text{ m}\cdot\text{s}^{-1}$ . The process of explosion cladding with plates of high-manganese steel through a copper interlayer was performed under such conditions. Ultimate shear forces corresponded to strength of copper, which was 2.5 times in excess of service requirements.

Optimisation of the technology of hardening of lugs of such complex pieces as axle box bodies by explosion cladding allowed a number of peculiarities

to be revealed and recommendations to be worked out for practical application of the processes. Unlike the process of explosion welding of flat or cylindrical surfaces, the cladding zones (there are two or four of them in the case under consideration) are under the effect of reflected, refracted and converging shock waves, which prevent formation of a welded joint. Therefore, this leads to the need to install process devices in open cavities to extinguish reflected shock waves, as well as synchronise the process of initiation of several explosive charges and use an interlayer of laminated materials to perform the damping function and prevent cracking. In explosion cladding of the surface located near the rigid wall, it is necessary to provide at the stage of design for a process gap between the plate welded and the wall. Its size is determined from a condition that the total time of propagation of an air shock wave in the wall should be in excess of the time of detonation of the explosive charge. Otherwise, this will result in a complicated arrangement of the detonation process. In determination of parameters of the dynamic turn angle, as well as welding parameters, it is necessary to take into account a maximum permissible collision velocity that causes no deformation of a structure.

1. Konon, Yu.A., Pervukhin, L.B., Chudnovsky, A.D. (1987) *Explosion welding*. Moscow: Mashinostroenie.
2. Kobelev, A.G., Potapov, I.N., Kuznetsov, E.B. (1991) *Technology for laminated metals*. Moscow: Metallurgiya.
3. Deribas, A.A. (1980) *Physics of explosion hardening and welding*. Novosibirsk: Nauka.
4. Dragobetsky, V.V., Tsygan, B.G., Pruzhilkin, I.I. *Method for cladding metal parts*. USSR author's cert. 1569145, Int. Cl. B 23 K 20/80. Publ. 11.04.88.

## WELDING IN SURGERY — A NEW DIRECTION IN WELDING TECHNOLOGY

A new development in the field of bioelectric technology, namely welding of live tissues, was discussed in a meeting of the Scientific Council in the Ministry of Health of Ukraine in Kiev on December 20, 2001.

Mr. V.F. Moskalenko (Minister of Health of Ukraine), Prof. B.E. Paton (President of the NAS of Ukraine), Prof. A.F. Vozianov (President of the Academy of Medical Science of Ukraine), Prof. Yu.A. Zozulya (Vice-President of the AMS of Ukraine) took part in the Scientific Council meeting, chaired by Prof. E.G. Pedachenko (Corresp.-Member of AMS of Ukraine).

Prof. M.P. Zakharash, Head of Defense-Medical Administration (DMA) of the Security Service of Ukraine (SSU), made a presentation on behalf of the team of Ukrainian scientists and specialists-developers of the technology. He presented the work of a team of engineering and medical staff of the participating organisations, namely: The E.O. Paton Electric Welding Institute of the NAS of Ukraine in co-operation with the International Association «Welding», Institute of Surgery and Transplantation (IST) of the AMS of Ukraine and Central Clinical Hospital of SSU DMA, which has been fulfilled in co-operation with CSMG, USA. The presentation included demonstration of documentaries, and fragments of planned surgery conducted under clinical conditions. Samples of advanced medical equipment and tools, applied during such surgery, were displayed. The developers

of this technology — Prof. V.K. Lebedev and Prof. Yu.A. Furmanov, also addressed the meeting.

This work has proved for the first time the possibility of joining cuts in various organs without applying sutures or metal cramps. The new joining technology is a further development of electrosurgical technologies.

Numerous preliminary experiments on animals were reported, which allowed establishing the conditions of producing the joints that ensured restoration of the physiological functions of the organs after surgery. A series of experiments on a control group of pigs of 40 animals confirmed the reliability of joining the incisions of the intestine and other organs, allowed conducting histological studies with the observation time from 14 up to 180 days, which confirmed the favourable process of restoration of tissue morphology. This was followed by the world's first clinical mastering of the welding technology in the field of general surgery and gynaecology, both in open surgery and in laparoscopy. More than 400 patients have been operated on with 100 % positive post-surgery results under the clinical conditions of SSU DMA and IST of the AMS of Ukraine.

It was noted that application of welding technology and new medical equipment greatly simplified the technique of surgery performance, eliminated the availability of foreign material in an organ or tissue after surgery with all the possible negative consequences, provided complete tightness of the joint, shortened the duration of surgical operations, of the patient staying under narcosis, essentially lowered the loss of blood, reduced the number of surgical tools required, in particular eliminated the need for special coagulation equipment, enabled development of specific procedures not applied in traditional surgery. This points both to rehabilitation conditions more favourable for the living organism, and to more cost-effective conditions for surgery.

Presentation led to a lively discussion, involving Prof. B.E. Paton; Prof. A.F. Vozianov; Prof. V.V. Smirnov, academician of the NAS of Ukraine, Institute of Microbiology and Virusology; Prof. S.A. Shalimov, Director of the Institute of Oncology of the AMS of Ukraine; Prof. G.M. Butenko, academician of the AMS of Ukraine, Corresp.-Member of the NAS of Ukraine, Institute of Gerontology; Prof. G.V. Gajko, Prof. D.Yu. Krivchenya and Prof. G.I. Zhaboedov, National Medical University; Prof. G.E. Timen, Institute of Otolaryngology; G.V. Dzyak, academician of the AMS of Ukraine,



Prof. M.P. Zakharash during his presentation



During an operation in the clinic



Welding system for joining live tissues

Rector of Dnepropetrovsk Medical Academy; Prof. A.V. Tokar, Kiev Medical Academy of Post-Graduate Education; Prof. Yu.A. Zozulya, Vice-President of the AMS of Ukraine. The speakers noted the importance of the scientific aspects of the new development and the good prospects for its application for surgical practice. Prof. B.E. Paton specifically described the prospects for further improvement and mastering the production of medical automated welding systems. Prof. A.F. Vozianov showed interest in application of the new technology in urology. Prof. Yu.A. Zozulya noted the evident rationality of

widening the areas of the new technology application, in particular, in neurosurgery.

The Scientific Council of the Ministry of Health of Ukraine approved the performed comprehensive team work and noted its high importance for development of surgical systems. The rationality of continuing research in this area was noted, as well as the need to set up production of the equipment for the leading clinics in Ukraine and a centre to train practising surgeons to master the technique of welding tissues, operation of the new equipment and to gain new experience of welding application in surgery.

## ***U.S. Congressman Visits the E.O. Paton Electric Welding Institute of the National Academy of Sciences of Ukraine***

On the 22<sup>nd</sup> of February, 2002, the U.S. Congressman Mr. B. Schaffer, accompanied by the First Secretary of the U.S. Embassy in Ukraine Mr. D. Moganko, visited the E.O. Paton Electric Welding Institute of the NAS of Ukraine. The American guests were welcomed by the Director of the Institute Prof. B.E. Paton. Participating in the discussions were Deputy Directors of the Institute Prof. S.I. Kuchuk-Yatsenko, Prof. K.A. Yushchenko and a number of leading scientists of the Institute.

Prof. B.E. Paton introduced Mr. Schaffer to results of cooperation of the PWI with the U.S. research centres, laboratories and known companies in the field of welding and related technologies, as well as to the really ingenious developments of the Institute in the field of high technologies.

The Institute has business and creative contacts with the American Welding Society (AWS), which last for almost quarter of a century. The Parties regularly exchange welding periodicals and specialists, participating in international conferences and exhibitions held in Ukraine and the U.S.A. The PWI is a collective member of AWS.

The collaborative activity of the Joint Venture Company «Pratt&Whitney-Paton», having its business place in workshops of the the PWI Pilot Plant for New Technologies, is a good example of the successful cooperation. Based on ingenious developments of the PWI associates, the JV Company manufactures specialised equipment and materials, and performs electron beam deposition of thermal barrier coatings on various-application gas turbine blades.

The unique technology for continuous flash butt welding developed by the PWI has found a wide application in the U.S.A. Some time ago the U.S. Company «McDermott» bought from the Institute the license for the equipment and technology for flash butt welding of off-shore pipelines. The collaborative work on the licensed technology for flash butt welding of rails is in progress with a number of major U.S. railway companies. About 60 mobile rail-welding units are now in operation in the U.S.A. They are employed for construction of railways and metro lines.

In the middle of the 1990s, in collaboration with «McDonnell Douglas» and the NASA Marshal Space Flight Center the Institute completed comprehensive tests of its versatile hand tool intended for performing various technological operations (welding, cutting, brazing, etc.) in space. The American and Ukrainian

specialists prepared an experiment on testing the «Universal» hardware in space on board the «Columbia» space shuttle. Unfortunately, the experiment was not conducted because of changes in the Shuttle flight program.

The Institute is involved in accomplishment of interesting projects and technological developments with companies «General Electric», «McDonnell Douglas», Lawrence Livermore and Sandia National Laboratories on investigation into weldability of advanced Al-Li and Al-Sc alloys and dispersion-strengthened materials, as well as on welding and brazing of similar and dissimilar materials.

Of special interest to the American guests was an information on research conducted by the PWI on joining biological tissues by high-frequency resistance welding. Welding in surgery has come out of the stage of experiment and is applied now by two Ukrainian clinics, which have already performed more than 400 surgery operations using this method. Almost from the very beginning, these works were carried out with participation by the U.S. Company «Consortium Service Management Group, Inc.». Nevertheless, this technology has not yet been applied in the U.S.A.

Prof. B.E. Paton in detail told Mr. Schaffer, at his request, about the activity of the PWI in the field of joining dissimilar materials: steel to aluminium alloys, aluminium to copper alloys, steel to titanium alloys and ceramics.

At the demonstration hall of the Institute the guests were introduced to the most interesting samples of equipment and technologies intended for space application, aerospace engineering, construction of main pipelines, etc.

During the visit, the U.S. Congressman Mr. B. Schaffer noted the high authority of the E.O. Paton Electric Welding Institute in scientific and industrial community of the U.S.A. The scientific-and-technical cooperation of the Institute with the American research centres and companies in the field of high technologies is mutually beneficial and should go on in the future. In conclusion, Mr. Schaffer expressed gratitude to Prof. B.E. Paton for interesting discussions and promised to render assistance in further development of the American-Ukrainian cooperation.

*I.A. Ryabtsev  
PWI Press-Group*